University of Nottingham

UK | CHINA | MALAYSIA

# Synchronization transition in the double dimer model

Neil Wilkins

Thesis submitted to

the University of Nottingham

for the degree of

*Doctor of Philosophy*

April 2021

# Abstract

Over the past few decades, interest has grown in classical and quantum phase transitions that cannot be understood in terms of a Landau–Ginzburg–Wilson (LGW) theory. These unconventional transitions, which are often accompanied by other exotic phenomena, such as topological order and confinement of fractionalized excitations, are known to exist in strongly correlated systems such as the dimer model.

This thesis investigates a novel 'non-LGW' phase transition in the classical double dimer model, consisting of two coupled replicas of the standard dimer model, which has no symmetry-breaking order parameter. It can be understood as a 'pure' topological or confinement transition, and we utilize these properties to distinguish the phases.

In two dimensions, we find a Berezinskii–Kosterlitz–Thouless transition at zero critical coupling, using a symmetry-based analysis of an effective height theory. Meanwhile, on the cubic lattice, we use Monte Carlo simulations to measure the (nonzero) critical coupling and critical exponents, the latter being compatible with the 3D inverted-XY universality class.

Furthermore, we map out the full phase plane when aligning interactions are added for dimers within each replica. In the square-lattice case, we are able to calculate the shape of the phase boundary in the vicinity of the noninteracting point exactly, starting from Lieb's transfer-matrix.

In arriving at this result, we also derive several results of general significance for the square-lattice dimer model. First, we rederive a host of known exact results from Lieb's transfer matrix, many of which were previously derived in the 1960's using Pfaffian methods. Second, we rigorously derive the continuum height description from the microscopic model using the technique of bosonization.

# Acknowledgements

I would like to thank my supervisor Stephen Powell for his invaluable guidance throughout this work. I also thank Juan P. Garrahan for useful comments. I am grateful for the help and encouragement of other PhD students in the Condensed Matter Theory group including, among others, Matt Jessop, Jemma Needham, Loredana Vasiloiu, Maike Ostmann, Tom Oakes and Gary McCormack. Finally, I would like to thank my parents, my sister and Adam for their support.

# Published work

Each chapter in this thesis is the subject of a publication or manuscript, as listed below.

Chapter 2:

**Neil Wilkins** and Stephen Powell. Interacting double dimer model on the square lattice. *Phys. Rev. B*, 102:174431, 2020.

Chapter 3:

**Neil Wilkins** and Stephen Powell. Topological sectors, dimer correlations and monomers from the transfer-matrix solution of the dimer model. *arXiv:2103.03260*, 2021 (under review by Phys. Rev. E).

Chapter 4:

**Neil Wilkins** and Stephen Powell. Derivation of field theory for the classical dimer model using bosonization. *In preparation.*

Chapter 5:

**Neil Wilkins** and Stephen Powell. Synchronization transition in the double dimer model on the cubic lattice. *Phys. Rev. B*, 99:144403, 2019.

# Contents

# Chapter 1

# Introduction

The classical dimer model is a paradigmatic example of a strongly-correlated system, in which dimers cover the edges of a lattice subject to a close-packing constraint, i.e., each vertex touches exactly one dimer (see Fig. 3.1 for an example configuration). First introduced in the 1930's to describe the adsorption of diatomic oxygen molecules onto a surface [1, 2], in modern physics the dimer model offers a simple setting for the study of novel phenomena in geometrically frustrated systems [3].

In particular, its extensive entropy reflects macroscopic ground-state degeneracy [4], while the configuration space splits into topological sectors labeled by horizontal and vertical 'flux' components, with a global rearrangement of dimers required to change sector, reflecting *topological order* [5]. Moreover, a dimer can be replaced by a pair of monomers, which can be separated by subsequent dimer updates and thus play the role of *fractionalized excitations* [3, 6].

In the absence of interactions, the dimer model exists in an unusual disordered phase known as the 'Coulomb phase' [6], which has liquid-like properties, i.e., both strong fluctuations and power-law dimer–dimer correlations. Fluctuations among the topological flux sectors in this phase are not suppressed, i.e., the flux variance is nonzero [7, 8], while, due to the background dimer configuration, a pair of inserted monomers interact via an effective Coulomb potential [4, 6]. The monomer pair is therefore deconfined, and can be separated to infinity with finite free-energy cost.

As the temperature is lowered, interacting dimer models can enter ordered

phases. A well-studied example of an equilibrium phase transition in the dimer model is the columnar-ordering transition on the square [9,10] and cubic [11] lattices, where interactions favor parallel alignment of dimers, $J$, and hence the ordered phase spontaneously breaks translation and rotation symmetries. A related class of transitions, where the symmetry is broken externally, e.g., by applying a 'magnetic field', are the Kasteleyn transition in the honeycomb-lattice dimer model [12] and its generalizations to three dimensions (3D) [13,14], as well as the '1GS' variant of the cubic dimer model studied by Chen et al. [15].

These phase transitions are interesting for several reasons. First, an application of the standard Landau–Ginzburg–Wilson (LGW) paradigm [16], in which one writes down a continuum theory in terms of a local order parameter, is not sufficient to describe the critical behavior. In these particular cases, this is understood to be a consequence of the hard constraints, since an LGW treatment fails to capture the unusual correlations of the Coulomb phase [17]. They therefore define a class of 'non-LGW' or 'unconventional' phase transitions [18,19].

Second, in addition to an order parameter, the two phases can be distinguished using the concepts of topological order and fractionalization. In the low-temperature phases, fluctuations among topological flux sectors and the separation of monomers necessarily disrupt the order and are hence penalized energetically. The flux variance is therefore suppressed exponentially with system size in the ordered phases, while a pair of inserted monomers has a free-energy cost proportional to separation, and is thus confined. The qualitative difference in these behaviors compared with the Coulomb phase provides a criterion to distinguish the phases. Such transitions can therefore be understood as 'topological' or 'confinement' phase transitions.

In this thesis, we study the *double dimer model* [20–22], comprising two replicas of the close-packed dimer model, with interactions between dimers that coincide (or 'overlap') in the two replicas, $K$. In the case of attractive coupling, $K \leq 0$, our results demonstrate the existence of a phase transition, in both two and three dimensions, between a standard Coulomb phase and a 'synchronized' phase, where both replicas remain disordered but their relative fluctuations are suppressed. We will refer to this as a 'synchronization transition'.

Owing to the nature of the ordered phase, this is an unusual example of a transition with no local order parameter, which clearly cannot be described within the LGW framework. Instead, it can be understood as an example of a 'pure' topological or confinement transition, with the relative flux variance and the effective interaction between a pair of monomers placed in a single replica providing suitable topological and confinement measures, respectively.

## Outline

For the most part, this thesis will examine the synchronization transition in the double dimer model on the square lattice. In Chapter 2, we do so using a combination of theoretical arguments and Monte Carlo (MC) simulations. Surprisingly, we establish that the critical coupling is zero using a symmetry-based analysis of an effective height theory, indicating that infinitesimal coupling is sufficient to synchronize the square-lattice case. By adding aligning interactions for dimers within each replica, we map out the full phase diagram in the $(J, K)$ plane. In this chapter we will also briefly address the case of the honeycomb lattice.

Motivated by our finding that the critical coupling is zero in Chapter 2, the combined aim of Chapters 3 and 4 is to analytically derive the shape of the phase boundary in the vicinity of the non-interacting point, using perturbation theory in the couplings $J$ and $K$. Along the way, we will also derive some results of general significance to the standard dimer model, namely a new derivation of known exact results in Chapter 3, as well as new field theory results in Chapter 4. Specifically, Chapter 3 solves the standard square-lattice dimer model with periodic boundaries and in the presence of a field $\boldsymbol{t}$ that couples to the (vector) flux. We do this by diagonalizing a modified version of Lieb's transfer matrix [23], which we map to a (quantum) free-fermion Hamiltonian in 1+1 dimensions. After deriving the torus partition function in the thermodynamic limit, we show how the configuration space divides into 'topological sectors' corresponding to distinct values of the flux. Additionally, we obtain explicit expressions for dimer occupation numbers, dimer–dimer correlation functions and the monomer distribution function. Most of these results were derived in the 1960's using a combinatoric

(Pfaffian) method [12, 24–29].

Since the effective height theory used to analyze the square-lattice synchronization transition in Chapter 2 is written down based on symmetry, it necessarily contains unknown phenomenological parameters that depend nontrivially on the couplings $J$ and $K$. In Chapter 4, we use the technique of bosonization [30] to map the free-fermion Hamiltonian of Chapter 3 to a free-boson quantum field theory, and show that the resulting action in the path integral formulation is precisely the effective height theory conjectured in Chapter 2, but now with known values for the parameters. Height theories of this kind have been written down based on symmetry for decades [31, 32]; our work in this chapter demonstrates how they can be derived rigorously from the microscopic model. Including interactions in this formalism perturbatively allows us to determine the shape of the phase boundary at linear order in the couplings $J$ and $K$.

In Chapter 5, we turn to the three-dimensional case and study the synchronization transition in the double dimer model on the cubic lattice. The structure of this chapter closely follows that of Chapter 2, and we similarly utilize a mixture of theoretical arguments and MC simulations to map out the full phase diagram in the $(J, K)$ plane. However, in the cubic-lattice case we place a stronger emphasis on the numerical aspect, focusing in particular on a finite-size scaling analysis to extract the (nonzero) critical coupling and critical exponents. We also solve the coupled double dimer model exactly on the Bethe lattice and show that it correctly reproduces the qualitative phase structure, but with mean-field critical behavior.

Finally, Chapter 6 concludes by drawing together the results of Chapters 2–5. Here, we summarize the main results of this thesis and discuss some possible experimental realizations and future work.

# Chapter 2

# Interacting double dimer model on the square lattice

## 2.1 Introduction

A prominent example of a non-LGW phase transition is the BKT transition in the two-dimensional (2D) XY model. Across the BKT transition, no symmetry is broken, as required for a 2D system at nonzero temperature by the Mermin–Wagner–Hohenberg theorem [33,34], and there is hence no local order parameter.

One can instead understand the BKT transition as an example of a 'topological' phase transition [35], where the phases are distinguished by their topological properties. An appropriate criterion is the response to a twist applied across the boundaries of the system: the associated energy cost, referred to as the helicity modulus (or phase stiffness), decreases exponentially with system size above the transition, but is nonzero in the thermodynamic limit below it [36,37].

In this chapter, our main focus is the synchronization transition in the double dimer model on the square lattice, which provides a superficially distinct example of a non-LGW transition in two dimensions. Surprisingly, we find that this transition occurs for infinitesimal coupling $K = 0^-$ between replicas, reflecting the critical nature of the noninteracting double dimer model [22].

We also find a novel 'antisynchronized' phase, where the overlap between replicas is minimized, which meets the Coulomb and synchronized phases at the zero-interaction point. Both of these features, along with the other transitions in

the phase diagram, can be understood in terms of effective field theories based on 'height models' [31, 32], which we derive based on symmetry.

For sufficiently strong repulsive (i.e., $J > 0$) interactions within each replica, we confirm the presence in the single dimer model of a transition into a staggered phase, as noted in previous works [9, 38, 39], and determine the critical coupling at which it occurs. We also demonstrate the existence of phases in the double dimer model that are simultaneously staggered and (anti)synchronized.

Previous work on the double dimer model on the square lattice has addressed the noninteracting case [22], as well as models that correspond to the limit $K \to +\infty$ [20] (see Sec. 2.2.2) and that include nonlocal interactions [21], motivated by a mapping from the quantum dimer model. Other related work has demonstrated the possibility of phase locking transitions in 2D superfluids [40] and the XY model [41].

An outline of this chapter is as follows. In Sec. 2.2 we define the interacting double dimer model and present its phase diagram, which is calculated using the methods detailed in the subsequent sections. In Sec. 2.3, we use symmetries to write down height field theories that describe the various phases and transitions. We then describe, in Sec. 2.4, the MC method that we use, which extends the standard worm algorithm, before presenting the numerical results that underlie our phase diagram and establish the critical properties in Sec. 2.5. We conclude in Sec. 2.6.

## 2.2 Model

We consider two replicas of a classical statistical model of dimers on an $L \times L$ square lattice with periodic boundary conditions (PBCs). To each link $l$ in each replica $\alpha \in \{1, 2\}$, we assign a dimer occupation number $d_l^{(\alpha)}$ which takes values 0 or 1. The close-packing constraint applies separately for each replica and requires that

$$\sum_{l \in \boldsymbol{r}} d_l^{(\alpha)} = 1 \,, \tag{2.1}$$

at each site $\boldsymbol{r}$, where the sum is over links $l$ connected to $\boldsymbol{r}$.

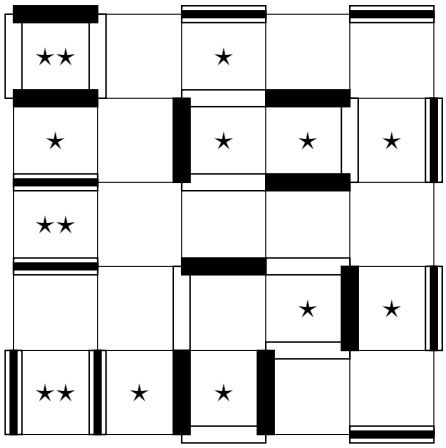

Figure 2.1: An example configuration of the double dimer model on the square lattice, in which two replicas of the close-packed dimer model (shown in black and white) are defined on the same lattice. According to Eq. (2.2), parallel pairs of nearest-neighbor dimers within each replica (marked with a star, $\star$) contribute $+J$ to the energy, and overlapping dimers contribute $+K$ to the energy. Hence, the energy of this configuration is $E = 15J + 9K$.

To each configuration, we assign an energy

$$E = J\left[N_{\parallel}^{(1)} + N_{\parallel}^{(2)}\right] + K\sum_{l} d_l^{(1)} d_l^{(2)}\,, \tag{2.2}$$

where $J$ and $K$ are, respectively, interaction strengths between parallel dimers within each replica and between overlapping dimers in the two replicas (see Fig. 2.1), and $N_{\parallel}^{(\alpha)}$ counts the number of parallel pairs of nearest-neighbor dimers in replica $\alpha$. The partition function is given by

$$Z = \sum_{\substack{c^{(1)}\in\mathfrak{C}_0\\ c^{(2)}\in\mathfrak{C}_0}} \mathrm{e}^{-E/T}\,, \tag{2.3}$$

where, for each replica $\alpha$, the sum is over the set $\mathfrak{C}_0$ of all close-packed dimer configurations (We set $k_{\mathrm{B}} = 1$ throughout.)

### 2.2.1 Magnetic field and height picture

On the square lattice, it is useful to define a (fictitious) 'magnetic field' [6, 8]

$$B_{\boldsymbol{r},\mu}^{(\alpha)} = \epsilon_{\boldsymbol{r}}\left[d_{\boldsymbol{r},\mu}^{(\alpha)} - \frac{1}{q}\right] \tag{2.4}$$

on the link $\boldsymbol{r}, \mu$ joining sites $\boldsymbol{r}$ and $\boldsymbol{r} + \boldsymbol{\delta}_\mu$, where $\boldsymbol{\delta}_\mu$ is a unit vector in direction $\mu \in \{x, y\}$ (and the lattice spacing is set to 1). Here, $\epsilon_{\boldsymbol{r}} = (-1)^{r_x + r_y} = \pm 1$ depending on the sublattice and $q = 4$ is the coordination number. (A similar construction applies to other bipartite lattices such as the honeycomb lattice.) The close-packing constraint for the dimers is then equivalent to the condition that the 'magnetic charge', given by the lattice divergence of $B^{(\alpha)}_{\boldsymbol{r},\mu}$,

$$Q^{(\alpha)}_{\boldsymbol{r}} = \sum_\mu \left[ B^{(\alpha)}_{\boldsymbol{r},\mu} - B^{(\alpha)}_{\boldsymbol{r}-\boldsymbol{\delta}_\mu,\mu} \right] , \tag{2.5}$$

is zero on every site. The normalization of $B^{(\alpha)}_{\boldsymbol{r},\mu}$ is chosen so that removing a dimer (and so breaking the close-packing constraint) leaves a pair of monomers on opposite sublattices with $Q_{\boldsymbol{r}} = \pm 1$.

In two dimensions, this divergence-free constraint is resolved by defining a scalar 'height' $z^{(\alpha)}$ on each plaquette, in terms of which

$$B^{(\alpha)}_{\boldsymbol{r},\mu} = \epsilon_{\mu\nu} \Delta_\nu z^{(\alpha)} , \tag{2.6}$$

where $\epsilon_{\mu\nu}$ is the two-dimensional Levi-Civita symbol and $\Delta_\nu$ denotes the lattice derivative [31, 32]. (This is the two-dimensional analog of $\boldsymbol{B} = \boldsymbol{\nabla} \times \boldsymbol{A}$.)

Together, Eqs. (2.4) and (2.6) define a one-to-one mapping between dimer configurations and their height representations, which is usually expressed as the following set of rules [10]: One first chooses a plaquette to be the zero of height. Then, moving anticlockwise around sites on sublattice A (B), the height increases (decreases) by $1 - 1/q$ when an occupied bond is crossed. If, instead, an empty bond is crossed, the height decreases (increases) by $1/q$. Example height representations are shown in Fig. 2.2.

The flux $\boldsymbol{\Phi}^{(\alpha)}$ for each replica $\alpha$ can be defined by

$$\Phi^{(\alpha)}_\mu = \frac{1}{L} \sum_{\boldsymbol{r}} B^{(\alpha)}_{\boldsymbol{r},\mu} = \frac{1}{L} \sum_{\boldsymbol{r}} \epsilon_{\boldsymbol{r}} d^{(\alpha)}_{\boldsymbol{r},\mu} , \tag{2.7}$$

which, because of the divergence-free constraint, is equivalent to the sum of the magnetic fields on links crossing a surface normal to $\boldsymbol{\delta}_\mu$. The latter definition highlights that $\Phi^{(\alpha)}_\mu$ is integer valued, and can only be changed by shifting dimers

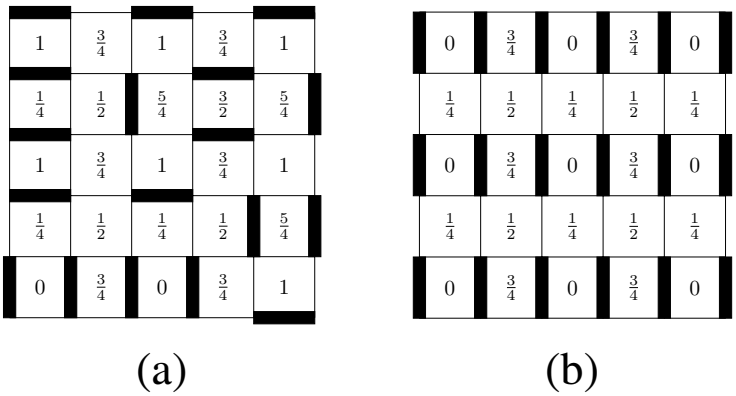


Figure 2.2: Example height representations $z$ of (a) an arbitrary dimer configuration and (b) the columnar configuration with magnetization order parameter $\boldsymbol{M} = \boldsymbol{\delta}_y$, which has average height $\langle z \rangle = \frac{3}{8}$.

around a loop encircling the whole system [4]. The flux thus plays the role of a topological invariant.

### 2.2.2 Phase diagram

Our phase diagram for the square-lattice double dimer model, Eq. (2.2), is shown in Fig. 2.3. The fact that the Coulomb, synchronized and antisynchronized phases meet at $K = J = 0$ is determined solely from a renormalization group (RG) analysis in Sec. 2.3.2. All other points are obtained numerically using a MC worm algorithm [42], as we describe in Sec. 2.5. In the remainder of this section, we define the phases appearing in Fig. 2.3.

#### Independent replicas

For $K = 0$ the two replicas are independent and behave as single dimer models with interactions that favor ($J < 0$) or disfavor ($J > 0$) parallel dimers. For $J = 0$, this model exhibits a Coulomb phase [6], where no symmetries are broken and the connected dimer–dimer correlation function $\langle d_l d_{l'} \rangle_{\mathrm{c}}$ decreases algebraically with separation. This phase extends to small nonzero $J$, but gives way to ordered phases for sufficiently large $|J|/T$.

For negative $J$, there is a transition to a phase with columnar order, as illustrated in Figs. 2.4(a) and (b), breaking translation and rotation symmetries [9,10].

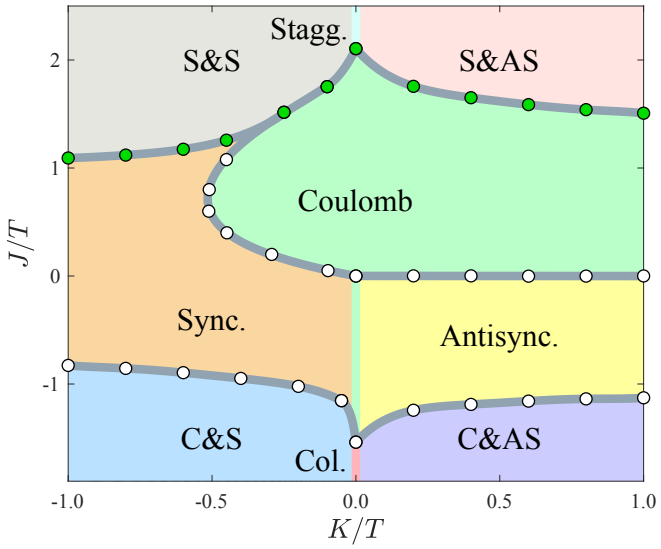


Figure 2.3: Phase diagram for the double dimer model of Eq. (2.2) on the square lattice, in the $(J/T, K/T)$ plane. Dots show points where the phase boundary has been determined using an RG analysis ($J = K = 0$) or MC simulations (all other points), and thick grey lines are guides to the eye. The ordered phases are: columnar ('Col'), staggered ('Stagg.'), synchronized ('Sync.'), antisynchronized ('Antisync.'), columnar & synchronized ('C&S'), columnar & antisynchronized ('C&AS'), staggered & synchronized ('S&S') and staggered & antisynchronized ('S&AS'). White dots represent BKT transitions, while green dots represent apparently continuous transitions.

An appropriate order parameter for this phase is the 'magnetization'

$$M_\mu = \frac{2}{L^d} \sum_{\boldsymbol{r}} (-1)^{r_\mu} d_{\boldsymbol{r},\mu} \,, \tag{2.8}$$

where $d = 2$ is the spatial dimension, which takes the values $\boldsymbol{M} = \pm\boldsymbol{\delta}_\mu$ in the four columnar states that maximize $N_\parallel$.

Besides the symmetry-breaking order parameter, the two phases are also distinguished by the probability distribution $P(\boldsymbol{\Phi})$ for the flux $\boldsymbol{\Phi}$. In the thermodynamic limit, the Coulomb phase has $P(\boldsymbol{\Phi}) \propto \mathrm{e}^{-\frac{\kappa}{2}|\boldsymbol{\Phi}|^2}$, where $\kappa$ is a function of $J/T$ (see Appendix 2.A.1). In the ordered phase, by contrast, $P(\boldsymbol{\Phi})$ is suppressed exponentially with system size for nonzero $\boldsymbol{\Phi}$, since changing the flux requires shifting a row of dimers that spans the whole system, with energy cost proportional to $L$. The mean square flux $\langle|\boldsymbol{\Phi}|^2\rangle$ therefore changes its behavior across the transition, being independent of $L$ in the Coulomb phase but vanishing in the thermodynamic limit in the columnar phase [10].

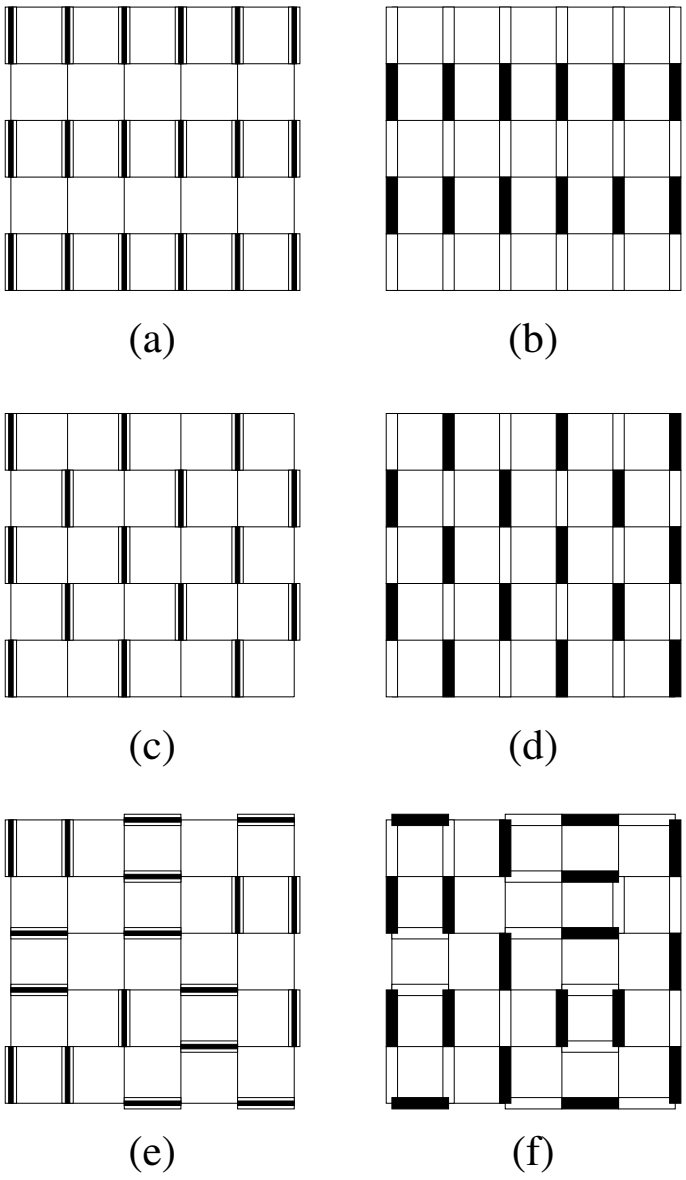


Figure 2.4: Example ground states of the double dimer model of Eq. (2.2) on the square lattice. (a)–(b) Columnar configurations, with maximal number of parallel plaquettes $N_{\parallel}^{(\alpha)}$, which minimize the energy for $J < 0$, $K = 0$. For $J < 0$, $K < 0$ configuration (a), with maximal overlap, is a columnar & synchronized ground state. Configuration (b) is a columnar & antisynchronized ground state when $J < 0$, $K > 0$, because it has zero overlap between replicas. (c)–(d) Staggered configurations, with zero parallel plaquettes $N_{\parallel}^{(\alpha)}$, which minimize the energy for $J > 0$, $K = 0$. For $J > 0$, $K < 0$, configuration (c) is a staggered & synchronized ground state, while for $J > 0$, $K > 0$, configuration (d) is a staggered & antisynchronized ground state. (e) A fully synchronized configuration, which is a ground state for $J = 0$, $K < 0$. (f) A fully antisynchronized configuration which is a ground state for $J = 0$, $K > 0$.

We also make use of a third diagnostic of the transition, which is based on confinement of 'monomers', empty sites in the otherwise close-packed configuration. Removing one dimer leaves a pair of monomers on adjacent sites, with unit charges $Q_{\boldsymbol{r}} = \pm 1$, which one can separate by locally rearranging the remaining dimers [6]. We define the monomer distribution function $G_{\mathrm{m}}(\boldsymbol{r}_+ - \boldsymbol{r}_-) = Z_{\mathrm{m}}(\boldsymbol{r}_+, \boldsymbol{r}_-)/Z$, where $Z_{\mathrm{m}}$ is the sum of Boltzmann weights of all configurations with a pair of monomers fixed at $\boldsymbol{r}_+$ and $\boldsymbol{r}_-$.

In the Coulomb phase, $G_{\mathrm{m}}$ decreases algebraically with separation (see Appendix 2.A.3), corresponding to a logarithmic effective potential $U_{\mathrm{m}}(\boldsymbol{R}) \equiv -\ln G_{\mathrm{m}}(\boldsymbol{R}) \sim \ln|\boldsymbol{R}|$ [4]. In the columnar phase, separating the monomers disturbs the ordered configuration, causing a linear potential $U_{\mathrm{m}}(\boldsymbol{R}) \sim |\boldsymbol{R}|$, and so $G_{\mathrm{m}}(\boldsymbol{R})$ decreases exponentially with $|\boldsymbol{R}|$. The potential $U_{\mathrm{m}}$ therefore grows without limit in both phases; this is in contrast with the 3D case, where the potential is bounded in the Coulomb phase, and the monomers are said to be 'deconfined' [6]. The different asymptotic behaviors nonetheless allow the phases to be distinguished, and we refer to the 2D Coulomb phase as 'quasideconfined' by analogy with quasi-long-range order in the low-temperature phase of the XY model [43].

For large positive $J$, the system instead reduces the number of parallel dimers. The square lattice has a large but subextensive set of 'staggered' configurations with the minimal value $N_{\parallel} = 0$ and $\boldsymbol{\Phi}$ of order $L$ [see, for example, Figs. 2.4(c) and (d)]. As a result, there is a transition at large positive $J/T$ to a phase where the flux vector takes a nonzero expectation value of order $L$ [9, 38, 39]. We treat this phase and the transition in detail in Sec. 2.5.3.

The Coulomb, columnar, and staggered phases of the single dimer model are shown in Fig. 2.3 on the vertical line $K/T = 0$. Note that the Coulomb phase extends to $J < 0$ along the line $K/T = 0$.

### Coupled replicas

For $K \neq 0$, the two replicas are coupled, with overlapping dimers favored for $K < 0$ and disfavored for $K > 0$.

The columnar and staggered phases at large $|J|/T$ have order parameters,

$\boldsymbol{M}^{(\alpha)}$ and $\boldsymbol{\Phi}^{(\alpha)}$ respectively, in each replica $\alpha$. In the thermodynamic limit, any nonzero coupling $K$ fixes the relative values in the two replicas in order to maximize or minimize the overlap, as illustrated for the ground states in Figs. 2.4(a)–(d). We refer to the resulting phases as columnar/staggered & (anti)synchronized. In particular, order by disorder selects $\boldsymbol{M}^{(1)} = -\boldsymbol{M}^{(2)}$ in the columnar & antisynchronized phase (we will discuss this in detail in Chapter 5), while $\boldsymbol{\Phi}^{(1)} = -\boldsymbol{\Phi}^{(2)}$ in the staggered & antisynchronized phase (see Sec. 2.5.3).

For smaller values of $|J|/T$, phase transitions occur that do not involve symmetry breaking, but can be characterized through the flux distribution and monomer confinement.

The flux distribution in the double dimer model can be described by the $2 \times 2$ covariance matrix $\langle \boldsymbol{\Phi}^{(\alpha)} \cdot \boldsymbol{\Phi}^{(\alpha')} \rangle$, but symmetry under replica exchange means we need only consider $\langle |\boldsymbol{\Phi}^{(\pm)}|^2 \rangle$, where $\boldsymbol{\Phi}^{(\pm)} = \boldsymbol{\Phi}^{(1)} \pm \boldsymbol{\Phi}^{(2)}$ are the total and relative fluxes corresponding to the fields $B^{(\pm)} = B^{(1)} \pm B^{(2)}$. For $K < 0$, one can postulate a phase where both replicas remain disordered and their flux variances $\boldsymbol{\Phi}^{(\alpha)}$ remain nonzero, but where their fluctuations are strongly correlated so that the variance of the relative flux $\langle |\boldsymbol{\Phi}^{(-)}|^2 \rangle$ vanishes in the thermodynamic limit [see Fig. 2.4(e)]. For $K > 0$, we similarly identify an 'antisynchronized' phase, where fluctuations are correlated between the replicas in order to reduce the amount of overlap [see Fig. 2.4(f)]. The relative flux $\langle |\boldsymbol{\Phi}^{(-)}|^2 \rangle$ also vanishes in the antisynchronized phase, as we argue in Sec. 2.3.2.

The monomer-confinement criterion can also be applied in the double dimer model, where we define $G_{\mathrm{m}}$ using a pair of monomers of opposite charge in the same replica, say $\alpha = 1$. Each monomer then has nonzero charge for $B^{(1)}$ and hence for both $B^{(-)}$ and $B^{(+)}$. They are therefore confined, with $G_{\mathrm{m}}(\boldsymbol{R})$ decreasing exponentially with $|\boldsymbol{R}|$, in the (anti)synchronized phases, where fluctuations of $\boldsymbol{\Phi}^{(-)}$ are suppressed.

To distinguish the columnar-ordered phases from the (anti)synchronized phases, one can instead insert pairs of monomers in both replicas simultaneously. Two monomers, one in each replica, on the same lattice site form a double charge for $B^{(+)}$, but have zero net charge for $B^{(-)}$. We therefore expect such objects to be confined only when the total flux variance is suppressed. Explicitly, we de-

fine the double monomer distribution function as $G_{\mathrm{d}}(\boldsymbol{r}_+ - \boldsymbol{r}_-) = Z_{\mathrm{d}}(\boldsymbol{r}_+, \boldsymbol{r}_-)/Z$, where $Z_{\mathrm{d}}$ is the sum of Boltzmann weights of all configurations with a pair of monomers fixed at $\boldsymbol{r}_+$ and $\boldsymbol{r}_-$ in each replica. In the columnar-ordered phases, $G_{\mathrm{d}}(\boldsymbol{R})$ decreases exponentially with $|\boldsymbol{R}|$, whereas in both the (unsynchronized) Coulomb phase and the (anti)synchronized phases, $G_{\mathrm{d}}(\boldsymbol{R})$ decreases only algebraically with $|\boldsymbol{R}|$. [For the (anti)synchronized phases, we show this directly in Appendix 2.A.5 using an effective field theory.]

**Infinite coupling between replicas**

The point $J = 0$, $K/T \to +\infty$ corresponds to the dimer loop model [20], which is equivalent to a fully-packed loop model with fugacity $n = 2$. The latter is known to be nonintegrable on the square lattice [44, 45] but solvable on the honeycomb lattice, where it is equivalent to a three-coloring model [46].

In the opposite limit $K/T \to -\infty$, the two replicas are perfectly aligned, and so act as a single dimer model with coupling $2J$ between parallel dimers. The values of $J/T$ at the columnar and staggered phase boundaries in this limit are therefore exactly half their values at $K = 0$. (For $K/T \to +\infty$, the critical couplings lie in between these two values, because the dimer loop model has higher entropy than the single dimer model.)

## 2.3 Field theories and critical properties

Using the height mapping, the long-wavelength properties of the Coulomb phase can be described in terms of a free field theory. In this section, we use symmetry to determine the perturbations to this action that are most relevant under the RG, and hence establish the critical properties at each transition.

### 2.3.1 Single dimer model

To construct a continuum theory we replace the effective magnetic field $B_{\boldsymbol{r},\mu}$ and height $z$ by coarse-grained fields $\boldsymbol{B}(\boldsymbol{r})$ and $h(\boldsymbol{r})$ obeying $B_\mu(\boldsymbol{r}) = \epsilon_{\mu\nu}\partial_\nu h(\boldsymbol{r})$. For

the single dimer model, the Coulomb phase has action

$$S_{\mathrm{SDM}} = \int d^2\boldsymbol{r}\, \frac{\kappa}{2}|\boldsymbol{B}|^2 = \int d^2\boldsymbol{r}\, \frac{\kappa}{2}|\boldsymbol{\nabla} h|^2\,, \tag{2.9}$$

where $\kappa$ is the stiffness, plus irrelevant higher-order terms. In the non-interacting limit ($J = 0$) the stiffness is

$$\kappa_\infty = \pi\,, \tag{2.10}$$

from comparison of observables, for example Eqs. (2.A.12) and (2.A.22), with exact results obtained using Pfaffian methods [28, 29].

To study the columnar-ordering transition in the single dimer model, we include additional terms in Eq. (2.9). We require that any action is local, and invariant under both $\pi/2$ rotations and translation of dimers; as discussed in Ref. [10], this imposes constraints on the form of allowed additional terms, which are summarized in Table 2.1. For example, translation of dimers by one lattice constant in the $x$ direction maps the height field $h(\boldsymbol{r}) \to -h(\boldsymbol{r} - \boldsymbol{\delta}_x) - \frac{1}{4}$, so the action must be invariant under this change. The critical theory, which includes the most relevant term (in the RG sense) consistent with all requirements, is a sine-Gordon model:

$$S_{\mathrm{SDM,col.}} = S_{\mathrm{SDM}} + \int d^2\boldsymbol{r}\, V\cos(8\pi h). \tag{2.11}$$

Note that if the symmetry of the single dimer model is reduced [15], such as in the case of anisotropic interaction strengths, i.e., $J_x \neq J_y$, between parallel dimers [39], the form of the allowed cosine term is modified.

A standard perturbative RG calculation [10] applied to the general sine-Gordon action

$$S_{\mathrm{SG}} = \int d^2\boldsymbol{r}\, \Big[\, \frac{\kappa}{2}|\boldsymbol{\nabla} h|^2 + V\cos(2\pi p h)\Big]\,, \tag{2.12}$$

with $p$ an integer, leads to the following conclusions: There is a BKT phase transition at a critical value of the stiffness

$$\kappa_{\mathrm{c}} = \frac{1}{2}\pi p^2\,. \tag{2.13}$$

| Requirement | Constraint | | |
|---|---|---|---|
| | SDM | coupled DDM, $h^{(-)}$ | coupled DDM, $h^{(+)}$ |
| Locality | $S[h] = S[h+1]$ | $S[h^{(-)}] = S[h^{(-)}+1]$ | $S[h^{(+)}] = S[h^{(+)}+1]$ |
| $\pi/2$ rotation symmetry | $S[h] = S[-h]$ | $S[h^{(-)}] = S[-h^{(-)}]$ | $S[h^{(+)}] = S[-h^{(+)}]$ |
| Translation symmetry | $S[h] = S[-h-1/4]$ | $S[h^{(-)}] = S[-h^{(-)}]$ | $S[h^{(+)}] = S[-h^{(+)}-1/2]$ |

Table 2.1: Requirements for the action of the single dimer model (SDM) and the double dimer model (DDM) with coupled replicas on the square lattice, and their corresponding constraints on allowed additional terms. (In the case of the DDM with independent replicas, SDM constraints apply separately to both $h^{(1)}$ and $h^{(2)}$.) Here, $\pi/2$ rotation symmetry refers to rotations about a plaquette center, and translation symmetry refers to translations by one lattice constant in the $x$ direction. For the SDM '$S$' means $S_{\mathrm{SDM,col.}}$, which describes the columnar-ordering transition [see Eq. (2.11)]. For the coupled DDM '$S$' means $S_{\mathrm{DDM,sync.}}$, which describes the synchronization transition [see Eq. (2.18)], or $S_{\mathrm{DDM,col.}}$, which describes columnar ordering of coupled replicas [see Eq. (2.20)]. The SDM constraints on $S[h]$ are discussed in detail in Ref. [10], and can be used to deduce the coupled DDM constraints on $S[h^{(\pm)}]$.

When $\kappa < \kappa_c$ the cosine term is irrelevant, i.e., it renormalizes to zero in the long distance theory, which is thus a free Coulomb phase. When $\kappa > \kappa_c$ it is relevant and locks the height field to discrete values.[1]

In the case of the columnar-ordering transition where the action, Eq. (2.11), has $p = 4$, we have

$$\kappa_c = 8\pi \,. \tag{2.14}$$

In the columnar phase ($\kappa > \kappa_c$) the cosine term locks the height field to values $h \in \left\{\frac{1}{8}, \frac{3}{8}, \frac{5}{8}, \frac{7}{8}\right\}$, which correspond to the average values of the height $z$ in the four columnar ground states [see, for example, Fig. 2.2(b)] [10].

### 2.3.2 Double dimer model

In the double dimer model, each replica has height field $h^{(\alpha)}$ with identical stiffness $\kappa$, and replicas are coupled by the term $\lambda \boldsymbol{\nabla} h^{(1)} \cdot \boldsymbol{\nabla} h^{(2)}$, with $\lambda \sim K$. The resulting

[1] A more detailed discussion of this RG calculation is provided in Sec. 4.3.4.

action for the unsynchronized Coulomb phase may be written

$$S_{\rm DDM} = \int d^2\boldsymbol{r}\, \left[\frac{\kappa_+}{2}|\boldsymbol{\nabla} h^{(+)}|^2 + \frac{\kappa_-}{2}|\boldsymbol{\nabla} h^{(-)}|^2\right] , \tag{2.15}$$

where $h^{(\pm)} = h^{(1)} \pm h^{(2)}$ and

$$\kappa_\pm = \frac{1}{2}(\kappa \pm \lambda)\,. \tag{2.16}$$

Note that in the non-interacting limit, i.e., $J = K = 0$, one has $\lambda = 0$, $\kappa = \kappa_\infty$ and

$$\kappa_{\pm,\infty} = \frac{\pi}{2}\,. \tag{2.17}$$

We now construct field theories that describe phase transitions in the double dimer model. For independent replicas, rotation and translation symmetry constraints apply separately to both $h^{(1)}$ and $h^{(2)}$, so each replica has an action given by Eq. (2.11). Therefore, when $K = 0$, one expects a columnar-ordering transition with the same critical properties as the single-replica case.

For the double dimer model with non-zero coupling $K$, we require an action local in both replicas, but now invariant under *simultaneous* $\pi/2$ rotations, and translations, of both replicas. To study the synchronization transition, we focus on the relative height $h^{(-)}$ [$h^{(+)}$ remains non-critical] and include additional terms in Eq. (2.15). The constraints on allowed terms are easily derived using results for the single dimer model, and are included in Table 2.1. For example, simultaneous translation of dimers by one lattice constant in both replicas maps the height fields $h^{(\alpha)}(\boldsymbol{r}) \to -h^{(\alpha)}(\boldsymbol{r} - \boldsymbol{\delta}_x) - \frac{1}{4}$, so that the relative height $h^{(-)}(\boldsymbol{r}) \to -h^{(-)}(\boldsymbol{r} - \boldsymbol{\delta}_x)$, which must be a symmetry of the action. In this case, the critical theory is a sine-Gordon model with $p = 1$:

$$S_{\rm DDM,sync.} = S_{\rm DDM} + \int d^2\boldsymbol{r}\, V^{(-)} \cos(2\pi h^{(-)})\,, \tag{2.18}$$

where, since the cosine term is forbidden by symmetry constraints when $K = 0$, we require $V^{(-)} \sim K$ to leading order. The constraints imposed by rotation and translation symmetry are identical (see Table 2.1), and hence Eq. (2.18) remains the correct critical theory for $h^{(-)}$ in reduced symmetry variations of the double

dimer model.

From Eq. (2.13), the critical stiffness for the synchronization transition is

$$\kappa_{-,\mathrm{c}} = \frac{\pi}{2}\,, \tag{2.19}$$

and ordering occurs when $\kappa_- > \kappa_{-,\mathrm{c}}$. The ordered phase is synchronized (antisynchronized) in regions of the phase diagram with negative (positive) coupling $K$, because the cosine term locks $h^{(-)} = 0\,(\frac{1}{2})$ in order to minimize the action. (The relative height of any synchronized ground state is clearly $h^{(-)} = 0$.) We identify the (high-temperature) Coulomb phase in the double dimer model with the low-temperature phase of the XY model, in accordance with the duality mapping from integer loops to the XY model [47]. Hence, the synchronization transition is a BKT transition but with an inverted temperature axis.

To locate the phase boundary at fixed $J/T$, we measure $\kappa_-$ as a function of $K/T$ using MC simulations and, from the crossing with its critical value $\kappa_{-,\mathrm{c}}$, identify a critical coupling $(K/T)_\mathrm{c}$. However, in the absence of interactions within replicas ($J = 0$) MC simulations are not necessary, because $\kappa_{-,\mathrm{c}}$ precisely coincides with the non-interacting limit ($K = 0$) of Eq. (2.17). Hence, in this case, the critical coupling $(K/T)_\mathrm{c} = 0$, and replicas synchronize for infinitesimal $K < 0$ [using Eq. (2.16) with $\lambda \sim K$].

In our phase diagram, $h^{(-)}$ is locked in the vicinity of columnar-ordering transitions when $K \neq 0$, and columnar ordering of coupled replicas is thus described by a critical theory in $h^{(+)}$. Adding to Eq. (2.15) the most relevant term consistent with the constraints on $S[h^{(+)}]$ in Table 2.1, one obtains

$$S_{\mathrm{DDM,col.}} = S_{\mathrm{DDM}} + \int d^2\boldsymbol{r}\, V^{(+)} \cos(4\pi h^{(+)})\,, \tag{2.20}$$

which is a sine-Gordon model with $p = 2$.

The critical stiffness for columnar-ordering of coupled replicas is therefore

$$\kappa_{+,\mathrm{c}} = 2\pi\,. \tag{2.21}$$

(In principle, $h^{(+)}$ could lock before $h^{(-)}$ if $\kappa_+ > \kappa_{+,\mathrm{c}}$ while $\kappa_- < \kappa_{-,\mathrm{c}}$, but we

do not observe this.) The ordered phases, for which $\kappa_+ > \kappa_{+,\mathrm{c}}$, are columnar & (anti)synchronized. In the columnar & synchronized phase, for example, where $h^{(-)} = 0$, the cosine term locks the total height to values $h^{(+)} = 2h^{(1)} \in \left\{\frac{1}{4}, \frac{3}{4}\right\}$. This is consistent with average values of the height $z$ for a single dimer model in the columnar phase (see Sec. 2.3.1).

### 2.3.3 Honeycomb lattice

In passing, we consider the double dimer model defined on the honeycomb lattice, which is also bipartite and thus amenable to a height description. As we outline in the following, in the absence of interactions within replicas, i.e., $J = 0$, synchronization on the honeycomb lattice occurs at a critical coupling $(K/T)_{\mathrm{c}} = 0$, as for the square lattice.

The Coulomb phase action for the single dimer model on the honeycomb lattice is given by Eq. (2.9), with stiffness fixed to $\kappa = \pi$ by exact calculations [4]. This is the same as for the square lattice, Eq. (2.10), and it follows that the double dimer model is again specified by Eqs. (2.15)–(2.17) in the non-interacting limit.

The constraints on $S[h]$ for the single dimer model are dependent on lattice type: For the honeycomb lattice they become $S[h] = S[h+1]$ from locality, $S[h] = S[-h]$ from $\pi/3$ rotation symmetry and $S[h] = S[-h - 1/3]$ from translation symmetry (cf. Table 2.1). However, for the double dimer model with non-zero coupling $K$, the constraints on $S[h^{(-)}]$ are unchanged and Eq. (2.18) remains the correct critical theory. Hence, as discussed in Sec. 2.3.2, the replicas synchronize for infinitesimal $K < 0$.

This finding may be interpreted in the context of a simple geometrically frustrated magnet, the triangular lattice Ising antiferromagnet (TLIAFM), which has Hamiltonian

$$\mathcal{H}_{\mathrm{TLIAFM}} = -\mathcal{J} \sum_{\langle i,j \rangle} \sigma_i \sigma_j \,, \tag{2.22}$$

where $\langle i, j \rangle$ denotes nearest-neighbor pairs of sites, $\mathcal{J} < 0$ and $\sigma_i = \pm 1$. The TLIAFM has an extensive number of ground states and, as illustrated in Fig. 2.5, each ground state is in one-to-one correspondence with a close-packed dimer configuration on the honeycomb lattice [4].

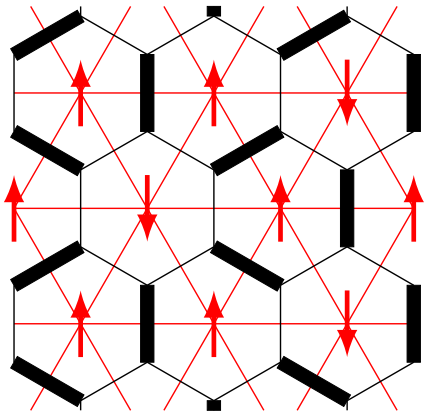

Figure 2.5: Red: a ground state of the triangular lattice Ising antiferromagnet; each plaquette contains a single frustrated bond [parallel spins contributing energy $+|\mathcal{J}|$ in Eq. (2.22)]. Black: corresponding close-packed dimer configuration on the dual (honeycomb) lattice, in which dimers lie across frustrated bonds.

In the limit $\mathcal{J}/T \to -\infty$, the double dimer model on the honeycomb lattice is equivalent to a bilayer TLIAFM with Hamiltonian

$$\mathcal{H} = \mathcal{H}^{(1)}_{\text{TLIAFM}} + \mathcal{H}^{(2)}_{\text{TLIAFM}} + \frac{K}{4} \sum_{\langle i,j \rangle} \sigma_i^{(1)} \sigma_j^{(1)} \sigma_i^{(2)} \sigma_j^{(2)} \,, \tag{2.23}$$

up to additive constants, where the four-spin interaction [48–50] derives from the term that counts overlapping dimers in Eq. (2.2). Hence, in this limit, spins in both replicas are either all aligned ($\sigma_i^{(1)} = \sigma_i^{(2)} \,\forall\, i$) or all antialigned ($\sigma_i^{(1)} = -\sigma_i^{(2)} \,\forall\, i$) for infinitesimal $K/T < 0$, according to our height analysis.

In fact, for general $\mathcal{J}$, Eq. (2.23) is the Hamiltonian of the Ashkin–Teller model on the triangular lattice. The phase diagram of this model, obtained using MC simulations in Fig. 7 of Ref. [51], includes a BKT critical point at $(\mathcal{J}, K) = (-\infty, 0)$ and is thus consistent with our conclusion.

Finally, because the honeycomb-lattice dimer loop model is solvable (see Sec. 2.2.2), one may also calculate the stiffnesses $\kappa_\pm$ exactly at $(J, K) = (0, +\infty)$, with result $\kappa_- = \frac{\pi}{2} = \kappa_{-,\text{c}}$ [52]. Hence, this point lies on the synchronization phase boundary. We also observe this feature in the square-lattice phase diagram, Fig. 2.3, where an exact calculation is not possible.

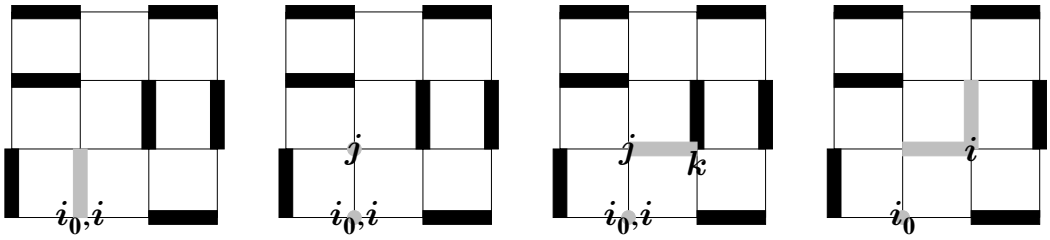


Figure 2.6: Local steps involved in a single-loop update of the worm algorithm (see main text for details).

## 2.4 Worm algorithm

We obtain numerical results using the MC worm algorithm [42], in which non-local loop updates are performed. With PBCs, loops can span the boundaries, allowing changes in flux.

### 2.4.1 Single loops

We begin by reviewing the standard implementation of the worm algorithm, using single loops. As illustrated in Fig. 2.6, the process is broken down into a series of local steps:

1. Choose a lattice site $i = i_0$ and a replica $\alpha$ at random.

2. In the current configuration of replica $\alpha$, site $i$ is connected by a dimer to a neighboring site $j$. Delete this dimer, denoted by $(i,j)^{(\alpha)}$.

3. Select a neighbour of $j$, called $k$, using a local detailed balance rule (described below), and insert a new dimer $(j,k)^{(\alpha)}$.

4. If $k = i_0$, close the loop. Otherwise return to step 2, using $i = k$.

Since all loops are performed without rejection, the worm algorithm is highly efficient.

The transition probability $P\big((i,j)^{(\alpha)} \to (j,k)^{(\alpha)}\big)$, with which the site $k$ is selected in step 3, is determined as follows. The requirement for global detailed balance translates into the local detailed balance condition [42]

$$w\big((i,j)^{(\alpha)}\big)P\big((i,j)^{(\alpha)} \to (j,k)^{(\alpha)}\big) = w\big((j,k)^{(\alpha)}\big)P\big((j,k)^{(\alpha)} \to (i,j)^{(\alpha)}\big)\,. \quad (2.24)$$

Here, $w\big((j,k)^{(\alpha)}\big)$ is the equilibrium probability of the configuration obtained on insertion of the dimer $(j,k)^{(\alpha)}$ in step 3. For the double dimer model, Eq. (2.2) implies

$$w\big((j,k)^{(\alpha)}\big) \propto \exp\left[-\left(JN_{(j,k)}^{(\alpha)} + Kd_{(j,k)}^{(\bar{\alpha})}\right)/T\right], \tag{2.25}$$

where $N_{(j,k)}^{(\alpha)} \in \{0,1,2\}$ is the number of nearest-neighbour dimers parallel to $(j,k)^{(\alpha)}$ in the same replica, whilst $d_{(j,k)}^{(\bar{\alpha})}$ is the dimer occupation number of the other replica $\bar{\alpha}$ on bond $(j,k)$. A solution for the transition probabilities, chosen to reduce backtracks (where $k=i$), is then

$$P\big((i,j)^{(\alpha)} \to (j,k)^{(\alpha)}\big) = \frac{w\big((j,k)^{(\alpha)}\big) - \min(\boldsymbol{w})\delta_{i,k}}{\sum_k w\big((j,k)^{(\alpha)}\big) - \min(\boldsymbol{w})}, \tag{2.26}$$

where $\boldsymbol{w}$ is a 4-component vector containing elements $w\big((j,k)^{(\alpha)}\big)$ for all $k$ [53].

Step 2 produces configurations containing two test monomers: a stationary monomer at site $i_0$, and a moving monomer at site $j$ (see Fig. 2.6). Hence, single-loop updates may be used to construct the monomer distribution function $G_{\mathrm{m}}(\boldsymbol{R})$, by tallying the monomer separation $\boldsymbol{R}$ after each step 2. Since the local detailed balance rule correctly samples only configurations produced by step 3, it is necessary to tally an amount $1/\sum_k w\big((j,k)^{(\alpha)}\big)$, rather than unity [10].

### 2.4.2 Double loops

Since they necessarily disrupt the order, single loops are suppressed in the synchronized phase, whereas simultaneous loops in both replicas are not. Therefore, to avoid problems with ergodicity, it is necessary to perform double-loop updates.

Double loops are constructed as follows. In step 1, loops begin in both replicas from the same randomly chosen site $i=l=i_0$. Both loops perform step 2 as for a single-loop update, deleting dimers $(i,j)^{(1)}$ and $(l,m)^{(2)}$. Step 3 now corresponds to 16 choices, with 4 in each replica. The insertion of new dimers $(j,k)^{(1)}$ and $(m,n)^{(2)}$ is associated with a configuration probability

$$w\big((j,k)^{(1)},(m,n)^{(2)}\big) = w\big((j,k)^{(1)}\big)w\big((m,n)^{(2)}\big)\exp(K\delta_{j,m}\delta_{k,n}/T), \tag{2.27}$$

where the factor $\exp(K\delta_{j,m}\delta_{k,n}/T)$ prevents double-counting of dimer overlap

when the bonds $(j,k)$ and $(m,n)$ are identical. Eq. (2.26) is then used to obtain the transition probabilities, with $\boldsymbol{w}$ a 16-component vector containing elements $w\big((j,k)^{(1)},(m,n)^{(2)}\big)$. In step 4, the process terminates when both loops close simultaneously, i.e. $k=n=i_0$. Otherwise we return to step 2, using $i=k$ and $l=n$.

Double-loop updates are performed without rejection, but their efficiency is poor at higher temperatures. This is because the probability of simultaneous closure is small, and so updates are unnecessarily long. To reduce this problem, we use double loops only for large $|K|/T$. We also define a spring potential $V\big((j,k)^{(1)},(m,n)^{(2)}\big)=\frac{1}{2}k_{\mathrm{s}}|\boldsymbol{r}_k-\boldsymbol{r}_n|^2$, where $k_{\mathrm{s}}$ is a spring constant and $\boldsymbol{r}_k$ denotes the position vector of site $k$. This is imposed by multiplying the equilibrium probabilities of Eq. (2.27) by $\exp(V)$, and favours the selection of sites $k$ and $n$ with smaller separation in step 3. The potential only modifies equilibrium probabilities of configurations during the double-loop construction, and so does not affect detailed balance for the close-packed dimer configurations.

### 2.4.3 Simulation parameters

We performed simulations on systems up to a maximum linear size $L=320$ with PBCs. Following equilibration, data points are typically obtained by averaging over $10^6$ MC sweeps, where a sweep is defined such that all lattice bonds are visited once on average. Statistical errors are estimated using a jackknife resampling method. A spring constant $k_{\mathrm{s}}=2$ is used for double loops.

We have checked the MC data by comparing with exact results for the cases $L\in\{2,4,6\}$ and with the limits discussed in Sec. 2.2.2.

## 2.5 Numerical results

In this section we use MC results, obtained using the worm algorithm [42], to map out the phase diagram shown in Fig. 2.3 and study the nature of each transition. There are three types of phase boundaries, which we consider in turn: synchronization, columnar ordering, and staggered ordering.

### 2.5.1 Synchronization transitions

In Sec. 2.3.2 we identified, when $J/T = 0$, a synchronization transition at infinitesimal coupling between replicas, i.e., $(K/T)_{\mathrm{c}} = 0$. The transition is BKT type, where the Coulomb and synchronized phases correspond to the low- and high-temperature phases of the XY model, respectively. In this section, we first provide MC evidence to support this finding, and then describe how the phase boundary, which divides the Coulomb and (anti)synchronized phases, is located in the case $J/T \neq 0$.

MC data for the synchronization transition when $J/T = 0$ are shown in Fig. 2.7. According to theoretical arguments, the mean-square flux difference $\langle|\boldsymbol{\Phi}^{(-)}|^2\rangle$, shown in the top-left panel, is system-size independent in the Coulomb phase (see Appendix 2.A.2) and decreases exponentially with $L$ in the synchronized phase. Hence, the extent of the $L$-independent region in $\langle|\boldsymbol{\Phi}^{(-)}|^2\rangle$ provides a rough bound $|(K/T)_{\mathrm{c}}| \lesssim 0.2$ on the critical coupling. In the thermodynamic limit, however, we expect that $(K/T)_{\mathrm{c}}$ scales to zero (see Sec. 2.3.2), while $\langle|\boldsymbol{\Phi}^{(-)}|^2\rangle$ jumps discontinuously to zero across the transition. The latter is typical of a BKT transition; for example, in the XY model there is a universal jump in the helicity modulus at the critical point [37, 47].

As expected for a BKT transition, the synchronization transition [at $(K/T)_{\mathrm{c}} = 0$] is not accompanied by a peak in the heat capacity per site $c$, as shown in the top-right panel of Fig. 2.7. Instead, near the transition, theory predicts a non-divergent essential singularity, which is unobservable [47, 54]. In the XY model, the main feature of the heat capacity per site is a broad peak, which is above the critical temperature and does not diverge with system size. We observe this in the synchronized phase of the double dimer model, i.e., when $K/T < 0$, consistent with the correspondence between the phases in the two models.

As discussed in Sec. 2.2.2, the Coulomb and synchronized phases may be distinguished through the monomer confinement criterion. In the bottom-left panel of Fig. 2.7, we show the confinement length $\xi$, defined by

$$\xi^2 = \frac{\sum_{\boldsymbol{R}} |\boldsymbol{R}|^2 G_{\mathrm{m}}(\boldsymbol{R})}{\sum_{\boldsymbol{R}} G_{\mathrm{m}}(\boldsymbol{R})}\,, \tag{2.28}$$

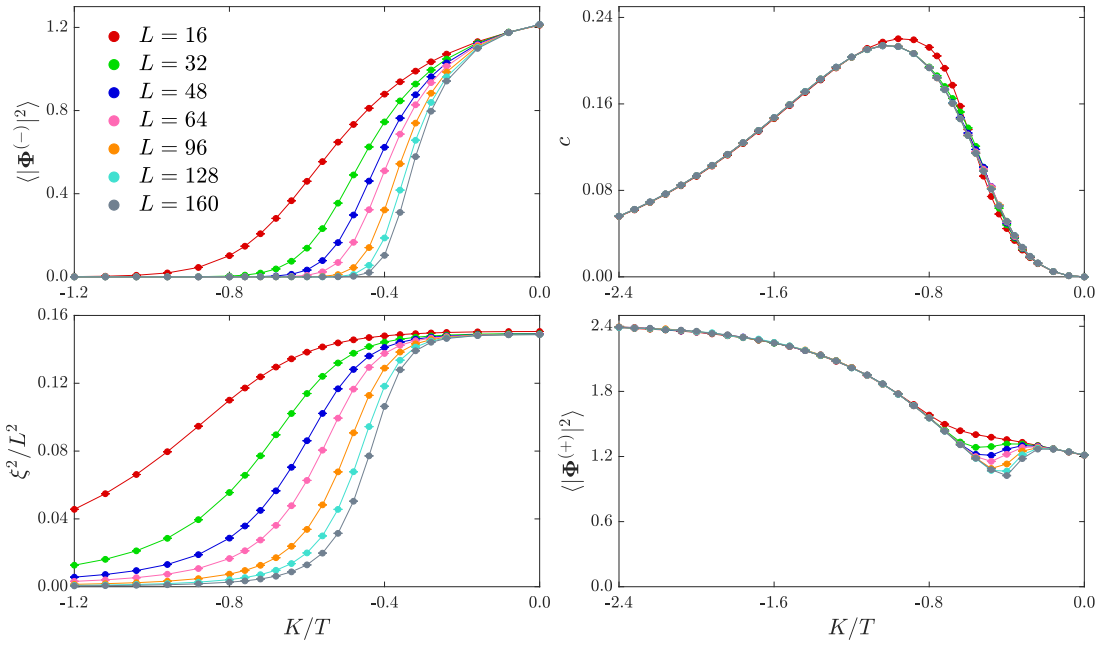


Figure 2.7: Mean-square flux difference $\langle|\mathbf{\Phi}^{(-)}|^2\rangle$ (top-left panel), heat capacity per site $c$ (top-right panel), square of the normalized confinement length $\xi^2/L^2$ (bottom-left panel) and mean-square total flux $\langle|\mathbf{\Phi}^{(+)}|^2\rangle$ (bottom-right panel) vs $K/T$, for the square-lattice double dimer model with $J = 0$ and different system sizes $L$. There is a synchronization transition at infinitesimal coupling between replicas, i.e., $(K/T)_\mathrm{c} = 0$. The transition is BKT type, where the Coulomb and synchronized phases correspond to the low- and high-temperature phases of the XY model, respectively.

which is equivalent to the root-mean-square separation of the test monomers. In the Coulomb phase, where monomers are quasideconfined with $G_\mathrm{m}(\boldsymbol{R}) \sim |\boldsymbol{R}|^{-\eta}$ (see Appendix 2.A.4), the confinement length has asymptotic dependence

$$\xi \sim \begin{cases} L & \text{for} \quad \eta < 2 \\ L^{2-\eta/2} & 2 < \eta < 4 \\ L^0 & 4 < \eta \end{cases} \tag{2.29}$$

(cf. the cubic-lattice case of Chapter 5, where fully-deconfined monomers have $\xi \sim L$ independent of stiffness). One also has $\xi \sim L^0$ in the synchronized phase, where monomers are confined. In our MC data, the region with $\xi \sim L$ at small $|K/T|$ is thus a signature of a quasideconfined phase. The behavior for large $|K/T|$ is consistent with a confined phase or quasideconfined monomers with $\eta > 4$; we have checked that $G_\mathrm{m}$ decays exponentially in this region (not shown),

implying the former. Note that for quasideconfined monomers we observe saturation at $\xi^2/L^2 \simeq 0.15$, which is less than the value expected for fully-deconfined monomers $\xi^2/L^2 \approx 1/6$ [using the result $(L^2+2)/6$ for the mean-square separation of free monomers hopping on an empty lattice].

In the synchronized phase, where the replicas become strongly correlated, fluctuations in the relative flux $\mathbf{\Phi}^{(-)}$ are suppressed. However, both replicas remain disordered so fluctuations in the total flux $\mathbf{\Phi}^{(+)}$ are large in both phases, as shown in the bottom-right panel of Fig. 2.7. In particular, at $K/T = 0$ where the replicas are independent, $\langle \mathbf{\Phi}^{(1)} \cdot \mathbf{\Phi}^{(2)} \rangle = \langle \mathbf{\Phi}^{(1)} \rangle \cdot \langle \mathbf{\Phi}^{(2)} \rangle = 0$ and $\langle |\mathbf{\Phi}^{(+)}|^2 \rangle = 2\langle |\mathbf{\Phi}^{(1)}|^2 \rangle$. This is half the value at $K/T \to -\infty$ for perfectly synchronized replicas, where $\langle \mathbf{\Phi}^{(1)} \cdot \mathbf{\Phi}^{(2)} \rangle = \langle |\mathbf{\Phi}^{(1)}|^2 \rangle$ and $\langle |\mathbf{\Phi}^{(+)}|^2 \rangle = 4\langle |\mathbf{\Phi}^{(1)}|^2 \rangle$.

For general $J/T$, we locate the phase boundary between the (anti)synchronized and Coulomb phases as follows. In the Coulomb phase, the mean-square total and relative flux are given by [10]

$$\langle |\mathbf{\Phi}^{(\pm)}|^2 \rangle = 2 \frac{\sum_{n_1,n_2 \in \mathbb{Z}} n_\pm^2 \mathrm{e}^{-\frac{\kappa_+}{2} n_+^2} \mathrm{e}^{-\frac{\kappa_-}{2} n_-^2}}{\sum_{n_1,n_2 \in \mathbb{Z}} \mathrm{e}^{-\frac{\kappa_+}{2} n_+^2} \mathrm{e}^{-\frac{\kappa_-}{2} n_-^2}} , \tag{2.30}$$

where $n_\pm = n_1 \pm n_2$, as derived in Appendix 2.A.2 starting from the continuum theory of Eq. (2.15). In the MC simulations we measure both $\langle |\mathbf{\Phi}^{(\pm)}|^2 \rangle$, and solve these equations numerically for the stiffnesses $\kappa_\pm$ using the Newton–Raphson method [55]. As shown in Fig. 2.8 for $J/T = 0.2$, the phase boundary is then located by scanning through $K/T$ until $\kappa_-$ crosses its critical value $\kappa_{-,\mathrm{c}} = \frac{\pi}{2}$ [see Eq. (2.19)].

To accurately determine the critical coupling, we use quadratic fits to measure a crossing point $(K/T)_\times$ for each system size (bottom-left inset of Fig. 2.8). For a BKT transition, the appropriate finite-size scaling form is [56, 57]

$$\left(\frac{K}{T}\right)_\times = \left(\frac{K}{T}\right)_\mathrm{c} + \frac{A}{\log(L/L_0)^2} , \tag{2.31}$$

where $A$ and $L_0$ are constants. From our fit for $J/T = 0.2$ (top-right inset of Fig. 2.8), we obtain $(K/T)_\mathrm{c} = -0.293(3)$. Ten further critical points located in this way are shown in the phase diagram of Fig. 2.3; this includes transitions into the antisychronized phase at $K > 0$ which, notably, all scale onto the line

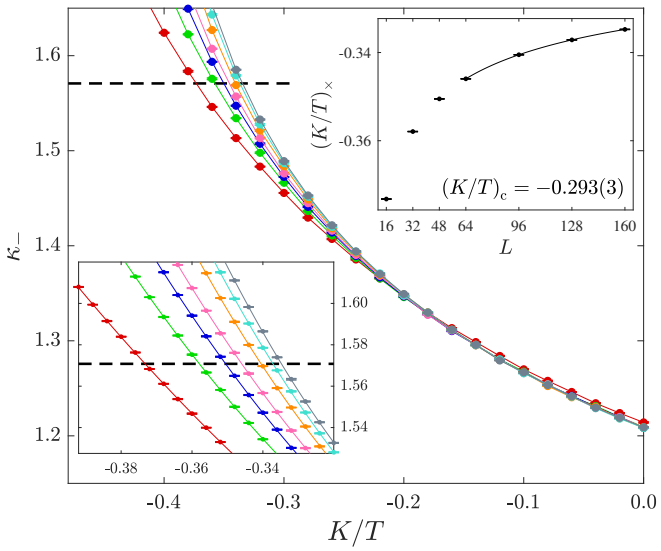


Figure 2.8: Stiffness $\kappa_-$ vs $K/T$ for $J/T = 0.2$. MC data crosses the critical value $\kappa_{-,c} = \frac{\pi}{2}$ (dashed line) at the synchronization transition. (Colors indicate different values of $L$ as in Fig. 2.7.) Bottom-left inset: Quadratic fits used to measure a crossing point $(K/T)_\times$ for each system size. Top-right inset: $(K/T)_\times$ vs system size $L$. The solid line is a fit to Eq. (2.31) for $L \geq 64$, from which a value for the critical coupling $(K/T)_c = -0.293(3)$ is obtained.

$J/T = 0$.

### 2.5.2 Columnar-ordering transitions

Next, we consider transitions into all columnar-ordered phases. For the case of independent replicas, i.e., when $K = 0$, columnar ordering at $J < 0$ separates the columnar and Coulomb phases. This transition has been studied in detail by Alet *et al.* in Refs. [9, 10] for the single dimer model, where the critical temperature is determined using an order parameter. We first review this approach.

The magnetization $\boldsymbol{M}$, defined in Eq. (2.8), breaks both translation and rotation symmetry in the columnar phase. Denoting by $N_\mu$ the number of dimers with orientation $\mu$, a simpler choice of order parameter is the dimer rotation symmetry breaking

$$D = \frac{2}{L^2} \left| N_y - N_x \right| , \tag{2.32}$$

a scalar that is sensitive only to rotation symmetry breaking.

This is still sufficient to indicate a columnar-ordering transition: In the Coulomb phase, by symmetry one expects $\langle N_x \rangle = \langle N_y \rangle$ so that $\langle D \rangle$ is small.

In the columnar phase, rotation symmetry is broken and all dimers are either horizontal or vertical. Hence, one expects $\langle D \rangle = 1$ (the total number of dimers is $L^2/2$). Alet *et al.* observe this behavior in Fig. 9 of Ref. [10].

The critical temperature may be determined accurately using the dimer rotation symmetry breaking Binder cumulant

$$B_D = 1 - \frac{\langle D^4 \rangle}{3\langle D^2 \rangle^2} \,. \tag{2.33}$$

In the vicinity of the critical point, the $k^{\text{th}}$ moment of the dimer rotation symmetry breaking has scaling form [58]

$$\langle D^k \rangle \sim L^{ka} f_k(L/\zeta) \,, \tag{2.34}$$

where, for a BKT transition, the correlation length diverges as [47]

$$\zeta \sim \exp\left(bt^{-\frac{1}{2}}\right) . \tag{2.35}$$

Here, $a$ and $b$ are unknown constants, $f_k$ is a universal function, and $t = (T - T_{\text{c}})/T_{\text{c}}$ is the reduced temperature. Hence, the Binder cumulant has zero scaling dimension, i.e.,

$$B_D \sim g(L/\zeta) \,, \tag{2.36}$$

where $g$ is a new universal function, because Eq. (2.33) has equal powers of $D$ in both numerator and denominator.

At the critical temperature $t = 0$, the correlation length diverges and, to leading order, the Binder cumulant has no system size dependence. Hence, depending on the finite-size behavior either side of $t = 0$, MC data for different system sizes may cross at the critical temperature. This is observed for $B_D$ in Fig. 11 of Ref. [10], from which Alet *et al.* report $T_{\text{c}} = 0.65(1)$ when $J = -1$, but not for the Binder cumulant of $\boldsymbol{M}$ [10, 59].

We now generalize this method to locate the phase boundary when $K/T \neq 0$, i.e., for coupled replicas. In this case, columnar-ordering transitions separate the (anti)synchronized phases from the columnar & (anti)synchronized phases. Since translation and rotation symmetry are broken in all columnar-ordered phases, we

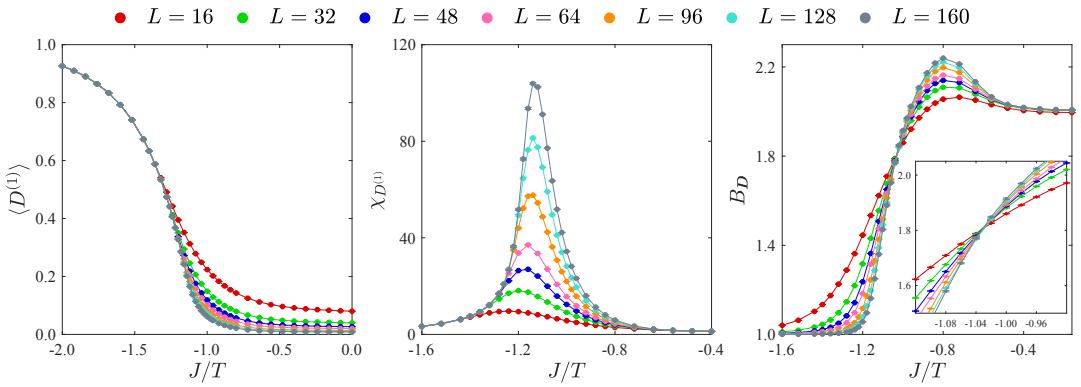


Figure 2.9: Dimer rotation symmetry breaking mean $\langle D^{(1)} \rangle$ (left panel), susceptibility $\chi_{D^{(1)}}$ (middle panel), and Binder cumulant $B_{\boldsymbol{D}}$ (right panel) vs $J/T$, for $K/T = -0.2$ and different system sizes $L$. The sharp drop in $\langle D^{(1)} \rangle$, and the corresponding sharp peak in $\chi_{D^{(1)}}$, indicate a phase transition between columnar & synchronized and synchronized phases. From the crossing in $B_{\boldsymbol{D}}$ (right panel, inset), we estimate the critical coupling $(J/T)_{\rm c} = -1.03(2)$. This is the generalization of Figs. 9–11 in Ref. [10] to the case of coupled replicas.

again expect a sharp drop in the mean dimer rotation symmetry breaking $\langle D^{(\alpha)} \rangle$ for both replicas, as well as a peak in the corresponding susceptibility

$$\chi_{D^{(\alpha)}} = L^2 \left( \langle \left[ D^{(\alpha)} \right]^2 \rangle - \langle D^{(\alpha)} \rangle^2 \right) , \tag{2.37}$$

in the vicinity of a transition. This is shown in Fig. 2.9 (left and middle panels) for the transition at $K/T = -0.2$, between the columnar & synchronized and synchronized phases.

To measure the critical coupling, we have analyzed the Binder cumulant $B_{D^{(\alpha)}}$ of Eq. (2.33) for both replicas, but no longer observe a distinct crossing point in the MC data when $K \neq 0$. Instead, we define the two-component vector $\boldsymbol{D} = (D^{(1)}, D^{(2)})$, with corresponding Binder cumulant

$$B_{\boldsymbol{D}} = \frac{\langle |\boldsymbol{D}|^4 \rangle}{\langle |\boldsymbol{D}|^2 \rangle^2} , \tag{2.38}$$

which is shown in Fig. 2.9 (right panel). Up to normalization, this is equivalent to Eq. (2.33) in the limits $K = 0$ and $K/T \to -\infty$. Deep within the columnar & (anti)synchronized phases, the probability distribution for $\boldsymbol{D}$ is sharply peaked at $D^{(1)} = D^{(2)} = 1$. Then $\langle |\boldsymbol{D}|^4 \rangle = \langle |\boldsymbol{D}|^2 \rangle^2$ so $B_{\boldsymbol{D}}$ saturates to unity. In

the (anti)synchronized phases, $D^{(\alpha)}$ follows a half-normal distribution for which $\langle \left[D^{(\alpha)}\right]^4 \rangle = 3\langle \left[D^{(\alpha)}\right]^2 \rangle^2$. The limiting value depends on $K/T$ through the correlator $\langle \left[D^{(1)}D^{(2)}\right]^2 \rangle$, which can only be calculated at $K = 0$ and $K/T \to -\infty$, where $B_{\boldsymbol{D}} = 2$ and 3, respectively.

As shown in Fig. 2.9 (right panel, inset), MC data for this Binder cumulant, $B_{\boldsymbol{D}}$, does exhibit a crossing point when $K \neq 0$. From this, we estimate a critical coupling $(J/T)_{\rm c} = -1.03(2)$ at $K/T = -0.2$. Our phase diagram, Fig. 2.3, includes this point along with ten others that have been obtained in the same way, but using only system sizes $L = 32$ and $L = 48$.

Columnar ordering in the limits $K = 0$, studied in Refs. [9, 10], and $K/T \to -\infty$, equivalent to columnar ordering of a single dimer model with $J_{\rm eff} = 2J$ (see Sec. 2.2.2), is known to be a BKT transition with an inverted temperature axis. We expect the whole phase boundary to share the same critical properties as these points.

We now use the field theory and RG analysis of Sec. 2.3 to verify our results. In Fig. 2.10 (top panel), we measure the monomer distribution function $G_{\rm m}(\boldsymbol{R})$ at the columnar-ordering transition for independent replicas ($J = -1$, $K = 0$ and $T = T_{\rm c} = 0.65$), counting only monomers on the same row, i.e., $\boldsymbol{R} = (X, 0)$. Each MC simulation can only construct $G_{\rm m}$ up to an arbitrary multiplicative constant, so we fix $G_{\rm m}(1, 0) = 1$.

The Coulomb phase monomer distribution function has asymptotic form

$$G_{\rm m}(X, 0) \sim X^{-\kappa/2\pi}\,, \tag{2.39}$$

which is derived in Appendix 2.A.3 starting from the continuum theory of Eq. (2.9). Due to PBCs, $G_{\rm m}(X, 0)$ is symmetric around $X = L/2$ in the MC simulations, hence the algebraic decay is cut off and Eq. (2.39) is only valid for $1 \ll X \ll L/2$. A fit to Eq. (2.39) over a suitable range in the inset yields an estimate for the critical stiffness $\kappa_{\rm c} = 8.028(3)\pi$, which is comparable with the RG prediction $\kappa_{\rm c} = 8\pi$ of Eq. (2.14) [the discrepancy perhaps arises due to the uncertainty in $T_{\rm c}$ and finite-size effects in $G_{\rm m}(X, 0)$]. Alet *et al.* instead measure the flux and invert Eq. (2.A.12) to obtain the stiffness (see Fig. 31 of Ref. [10]).

In the case of coupled replicas, one requires the asymptotic form of $G_{\rm m}(\boldsymbol{R})$

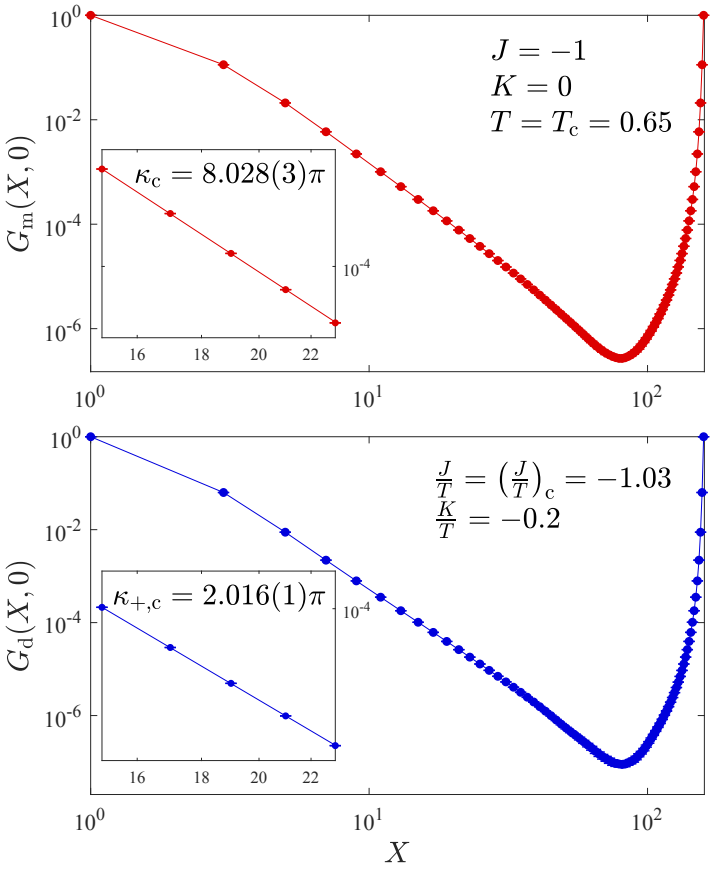


Figure 2.10: Top panel: Log–log plot of monomer distribution function $G_{\rm m}(X,0)$ vs monomer separation $X$ at the columnar-ordering transition for independent replicas. Bottom panel: Log–log plot of double monomer distribution function $G_{\rm d}(X,0)$ vs $X$ at a columnar-ordering transition for coupled replicas. In each case, the system size is $L = 160$. Insets: Solid lines are fits to Eqs. (2.39) and (2.40) for $15 \geq X \geq 23$, from which values for the critical stiffness $\kappa_{\rm c} = 8.028(3)\pi$ and $\kappa_{+,{\rm c}} = 2.016(1)\pi$ are obtained, respectively.

in the (anti)synchronized phases, which is less straightforward. Instead, it is convenient to consider the double monomer distribution function $G_{\rm d}(\boldsymbol{R})$ (see Sec. 2.2.2) which, as derived in Appendix 2.A.5, has asymptotic form[2]

$$G_{\rm d}(X,0) \sim X^{-2\kappa_+/\pi}\,. \tag{2.40}$$

In Fig. 2.10 (bottom panel), we show $G_{\rm d}(\boldsymbol{R})$ for the columnar-ordering transition

[2]The height description of the columnar-ordering transitions necessarily implies a discontinuity in the phase boundary at $K = 0^{\pm}$. To see this, compare $G_{\rm d}$ on the phase boundary at $K = 0$ and $K = 0^{\pm}$: the former is equivalent to $G_{\rm m}^2$, where $G_{\rm m}$ is given by Eq. (2.A.22) and $\kappa = \kappa_{\rm c} = 8\pi$, hence $G_{\rm d} \sim |\boldsymbol{R}|^{-8}$. The latter, however, is given by Eq. (2.A.27) with $\kappa_+ = \kappa_{+,{\rm c}} = 2\pi$, i.e., $G_{\rm d} \sim |\boldsymbol{R}|^{-4}$. We have checked that this discontinuity is small and, indeed, it is not resolved by our Binder cumulant method. Such an effect, though, can be seen in the phase diagram of Ref. [39].

at $K/T = -0.2$ and $J/T = (J/T)_{\rm c} = -1.03$. In the inset, a fit to Eq. (2.40) over a suitable range gives $\kappa_{+,{\rm c}} = 2.016(1)\pi$, which is close to the expected value $\kappa_{+,{\rm c}} = 2\pi$ of Eq. (2.21).

### 2.5.3 Staggered-ordering transitions

We begin by describing the nature of the staggered phase in the single dimer model. The simplest staggered ground states (which contain no parallel pairs of dimers) have all dimers horizontal, such as Fig. 2.11(a), or vertical, such as Fig. 2.11(d). More complicated ground states are obtained by shifting dimers along diagonal loops, or 'staircases', that span the periodic boundaries. For example, Fig. 2.11(b) is a staggered ground state related to Fig. 2.11(a) by translation of dimers around the red staircase. Translation of dimers around further staircases results in Fig. 2.11(c), and then Fig. 2.11(d).

From Eq. (2.7), the ground state in Fig. 2.11(a) has flux $\mathbf{\Phi} = (L/2, 0)$. Introduction of each staircase reduces (increases) the number of horizontal (vertical) dimers by $L$, resulting in a flux change $\Delta\mathbf{\Phi} = (-1, 1)$. Consequently, the subset of ground states in Figs. 2.11(a)–(d) occupy the line $\Phi_x + \Phi_y = L/2$ in flux space, as illustrated by the center of Fig. 2.11. More generally, the full ground state manifold is given by the equation

$$|\Phi_x| + |\Phi_y| = \frac{L}{2}\,. \tag{2.41}$$

This simple representation of the staggered ground states is specific to two dimensions, and cannot be generalized to the cubic lattice.

There is only one ground state, shown in Fig. 2.11(a), with flux $\mathbf{\Phi} = (L/2, 0)$. To construct configurations with $\Phi_y > 0$ [for example Figs. 2.11(b)–(d)] one must insert $\Phi_y$ staircases into $L/2$ slots, for which the number of choices is given by the binomial coefficient ${}^{L/2}C_{\Phi_y}$. In general, the degeneracy of a staggered ground state with flux $\mathbf{\Phi} = (\Phi_x, \Phi_y)$ is ${}^{L/2}C_{|\Phi_y|}$ [or equivalently, by Eq. (2.41), ${}^{L/2}C_{|\Phi_x|}$].

Using this binomial distribution, one may calculate observables deep within

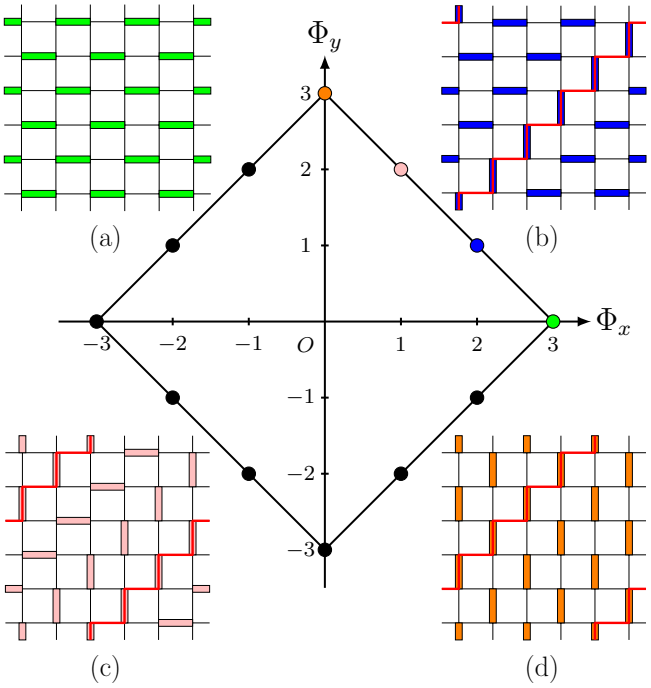


Figure 2.11: Examples of staggered ground states for a single dimer model on a $6 \times 6$ lattice with PBCs. Ground states (a) and (d) have all dimers horizontal and vertical, respectively. Ground states (b), (c) and (d) are related to (a), (b) and (c), respectively, by translation of dimers around red 'staircases'. Center: Ground state manifold in flux space, described by the equation $|\Phi_x| + |\Phi_y| = L/2$; a dot with flux $\mathbf{\Phi} = (\Phi_x, \Phi_y)$ corresponds to ${}^{L/2}C_{|\Phi_x|}$ degenerate ground states (see text for explanation). Colored dots correspond to the positions of ground states (a)–(d).

the staggered phase. For example, the total number of ground states is

$$N = 4 \left( \sum_{\Phi_x=0}^{L/2} {}^{L/2}C_{|\Phi_x|} - 1 \right) \tag{2.42}$$

$$= 4(2^{L/2} - 1), \tag{2.43}$$

which corresponds to a subextensive entropy $\log N \approx \frac{L}{2} \log 2$. We also infer that, since the quantity $|\Phi_x|/L$ is distributed around $1/4$ with standard deviation $\propto L^{-1/2}$, the flux takes one of the four values $\mathbf{\Phi}/L = (\pm\frac{1}{4}, \pm\frac{1}{4})$ in the thermodynamic limit, thus spontaneously breaking rotation and translation symmetries. At finite $J$ there are fluctuations out of these extremal states, but the symmetry-breaking transition remains.

For the double dimer model, the above discussion allows one to write down

the partition function exactly, as a function of $K/T$, in the limit $J/T \to \infty$. For example, for both replicas consider only ground states in the first quadrant of Fig. 2.11, i.e., $0 \leq \Phi_{x,y} \leq L/2$. A staircase can be covered by either horizontal or vertical dimers within each replica, and so, including a field $\boldsymbol{h}$ that couples to the flux difference $\boldsymbol{\Phi}^{(-)}$, has four possible Boltzmann weights: $\exp(-KL/T)$ when both replicas have the same orientation (i.e., both horizontal or vertical), and $\exp[\pm \boldsymbol{h} \cdot (1,-1)]$ when both replicas have different orientations. Since, in total, there are $L/2$ staircases, the contribution of these ground states to the partition function is

$$Z_{11} = 2^{L/2} \left[ \mathrm{e}^{-KL/T} + \cosh\left(h_x - h_y\right) \right]^{L/2} . \tag{2.44}$$

Because $Z_{11}$ contains all configurations with maximal overlap, we expect that, for $K = 0^-$, the full partition function asymptotically approaches $Z_{11}$ in the thermodynamic limit. By taking suitable derivatives with respect to $\boldsymbol{h}$, one finds that the flux difference $\boldsymbol{\Phi}^{(-)}$ is distributed around $\mathbf{0}$ with variance $\approx L\mathrm{e}^{-|K|L/T}$. Hence, as illustrated in Fig. 2.3, in the staggered phase infinitesimal negative coupling is sufficient to synchronize the two replicas. Similarly, for $K > 0$, one expects $\boldsymbol{\Phi}^{(1)}/L = (\pm\frac{1}{4}, \pm\frac{1}{4})$ in the thermodynamic limit, $\boldsymbol{\Phi}^{(2)} = -\boldsymbol{\Phi}^{(1)}$ to minimize overlap, and hence $\boldsymbol{\Phi}^{(+)} = 0$ (we note that there are also, for example, configurations with $\boldsymbol{\Phi}^{(-)} = 0$ and zero overlap, but their degeneracy is less by a factor exponentially small in $L$).

We now use MC results to examine transitions into all staggered-ordered phases. To begin, we focus on the case $K = 0$, where staggered ordering at $J > 0$ separates the staggered and Coulomb phases. One expects the same critical properties as for the single-replica case so, for simplicity, we consider a single dimer model with $J = +1$ and vary the temperature.

By analogy with the columnar-ordering transitions (cf. Fig. 2.9), we use the staggered order parameter [60]

$$s = \frac{2}{L} \left( |\Phi_x| + |\Phi_y| \right) \tag{2.45}$$

to determine the critical temperature. At low temperatures, deep within the staggered phase, one has $\langle s \rangle = 1$ by definition of the ground state manifold,

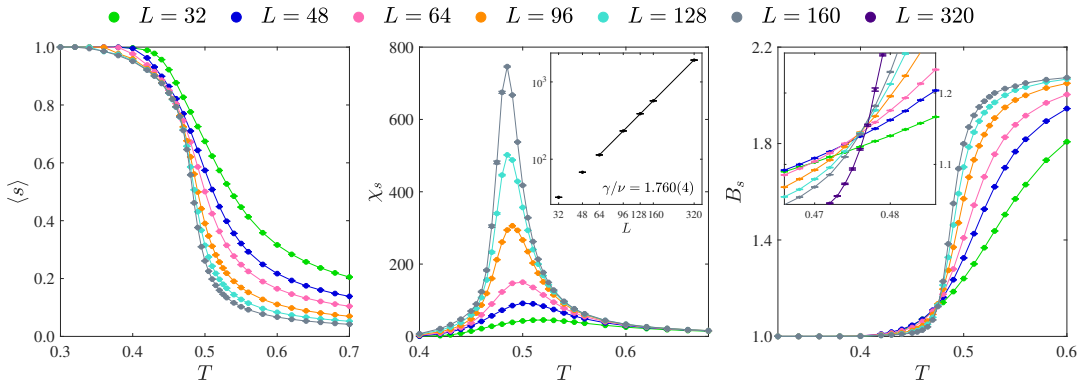


Figure 2.12: Staggered order parameter mean $\langle s \rangle$ (left panel), susceptibility $\chi_s$ (middle panel), and Binder cumulant $B_s$ (right panel) vs temperature $T$, for the square-lattice dimer model (two independent replicas, $K = 0$) with $J = +1$ and different system sizes $L$. The sharp drop in $\langle s \rangle$, and the corresponding sharp peak in $\chi_s$, indicate a phase transition between staggered and Coulomb phases. Right panel, inset: From the crossing in $B_s$, we estimate the critical temperature $T_c = 0.477(2)$. Middle-panel, inset: Log–log plot of $\chi_s$, evaluated at the critical temperature $T_c = 0.477$, versus system size $L$. The solid line is a fit to Eq. (2.48) for $L \geq 64$, from which a value $\gamma/\nu = 1.760(4)$ is obtained.

Eq. (2.41), whereas in the Coulomb phase $\langle s \rangle$ is small because the flux distribution $P(\mathbf{\Phi})$ is peaked at $\mathbf{\Phi} = \mathbf{0}$ with width $\sim L^0$ [see Eq. (2.A.11)]. Between these regimes, the sharp drop in $\langle s \rangle$ and peak in the corresponding susceptibility

$$\chi_s = L^2 \left( \langle s^2 \rangle - \langle s \rangle^2 \right) , \tag{2.46}$$

shown in Fig. 2.12 (left and middle panels), are characteristic of a phase transition.

In Fig. 2.12 (right panel), we obtain the critical temperature from the crossing point in the staggered order parameter Binder cumulant [60]

$$B_s = \frac{\langle s^4 \rangle}{\langle s^2 \rangle^2} . \tag{2.47}$$

Our estimate, $T_c = 0.477(2)$, is close to existing results $T_c = 0.449(1)$ and $T_c = 0.51$ of Refs. [9, 39], respectively [see also Ref. [38], which reports $T_c = 0.72(5)$].

The absence of relevant cosine terms in the action for $J > 0$ implies that staggered ordering does not occur through a BKT transition, and is consistent with either a first-order transition, as suggested by Castelnovo *et al.* [38], or a standard Landau-type ordering transition. Our MC data suggest that the

transition is in fact continuous: $B_s$ has a crossing point, while the heat capacity per site $c$ (not shown) does not diverge strongly with system size (i.e., not $\sim L^2$).

At the critical point for a continuous transition, the susceptibility has finite-size scaling form [47]

$$\chi_s \sim L^{\gamma/\nu}\,, \tag{2.48}$$

where $\gamma$ and $\nu$ are the susceptibility and correlation-length exponents, respectively. A fit to this form in Fig. 2.12 (middle panel, inset) yields a rough estimate $\gamma/\nu = 1.760(4)$, where the error reflects the quality of the fit, but ignores uncertainty in $T_\mathrm{c}$ and higher-order corrections to Eq. (2.48). This is close to $\gamma/\nu$ in the Ising ($\gamma = 7/4$, $\nu = 1$), 3-state Potts ($\gamma = 13/9$, $\nu = 5/6$) and Ashkin–Teller ($\gamma = 7/6$, $\nu = 2/3$) 2D universality classes [61]. Based on the four values $\boldsymbol{\Phi}/L = (\pm\frac{1}{4}, \pm\frac{1}{4})$ taken by the flux deep within the ordered phase, a naïve Landau theory would be that of the 4-state clock model, which is equivalent to two uncoupled Ising models [62] and thus supports the Ising universality class. Confirmation of this would require a more detailed analysis, which is beyond the scope of this work.

In the height picture, the transition occurs when the stiffness $\kappa = 0$ in the Gaussian action, Eq. (2.9). For this reason, Otsuka [39] and Alet [60] have made the connection with the quantum spin-$\frac{1}{2}$ XXZ chain, and spin ice subjected to uniaxial pressure [63], for which all terms in the action vanish to infinite order at the critical point (by symmetry for the XXZ chain; 'accidentally' for spin ice under pressure). Such infinite-order multicritical points [64] exhibit both first-order and continuous features. Since we do not observe the former, our results suggest that higher-order terms do not vanish in the dimer model, i.e., $P(\boldsymbol{\Phi})$ is not flat [see Eq. (2.A.11)], at $T_\mathrm{c}$.

To locate the full phase boundary our approach is straightforwardly extended to the case of coupled replicas, using crossing points in the Binder cumulant

$$B_{\boldsymbol{s}} = \frac{\langle |\boldsymbol{s}|^4 \rangle}{\langle |\boldsymbol{s}|^2 \rangle^2}\,, \tag{2.49}$$

where $\boldsymbol{s} = (s^{(1)}, s^{(2)})$. Eleven such points are included in our phase diagram, Fig. 2.3, obtained for system sizes $L = 64$ and $L = 96$. We again infer the critical

properties of the whole phase boundary from the limits $K = 0$ and $K/T \to -\infty$.

## 2.6 Conclusions

The central result of this chapter is the phase diagram of the classical double dimer model on the square lattice, shown in Fig. 2.3. Our results demonstrate the presence of a synchronization phase transition at which fluctuations between the two replicas become more strongly correlated, with signatures in the variance of the relative flux and in the monomer distribution function, but no symmetry breaking. The critical properties at this transition are of the BKT type, as expected for such a transition in 2D.

In addition, we find an antisynchronized phase, where overlaps between the two replicas are reduced. Our numerical results indicate that the phase boundary with the Coulomb phase runs along the line $J/T = 0$ for positive $K/T$ (except possibly close to $K = 0$, where the finite-size scaling becomes more difficult), as has previously been conjectured [20].

Remarkably, we find that these three phases meet at the noninteracting point $J = K = 0$, implying that an infinitesimal coupling between replicas is sufficient to drive the synchronization transition. This conclusion is supported both by our numerical results and by theoretical considerations based on a height field theory.

In the following two chapters, we will apply bosonization to the transfer-matrix solution of the dimer model [23]. This provides an alternative perspective on the fact that the synchronization transition is at infinitesimal coupling, because it can be understood as a pairing transition for fermions at zero temperature in 1D. It also allows one to predict the asymptotic form of the phase boundary exactly, based on perturbation theory in terms of the couplings.

# Appendices

## 2.A Calculation of observables using field theories

In this Appendix, we calculate various observables in the single dimer model (SDM) and double dimer model (DDM) using the continuum theories introduced in Sec. 2.3.

### 2.A.1 SDM flux in the Coulomb phase

We first calculate flux moments in the SDM Coulomb phase; a similar version of this derivation can be found in Refs. [7, 10]. The SDM Coulomb phase action is given by

$$S_{\mathrm{SDM}} = \int d^2\boldsymbol{r}\, \frac{\kappa}{2} |\boldsymbol{B}|^2 \,, \tag{2.A.1}$$

and the probability associated with magnetic field $\boldsymbol{B}(\boldsymbol{r})$ is $P[\boldsymbol{B}] = \mathrm{e}^{-S_{\mathrm{SDM}}[\boldsymbol{B}]}/Z$, where $Z$ is the partition function.

We write the magnetic field as a Fourier series

$$\boldsymbol{B}(\boldsymbol{r}) = \frac{1}{L} \sum_{\boldsymbol{k}} \mathrm{e}^{-\mathrm{i}\boldsymbol{k}\cdot\boldsymbol{r}} \tilde{\boldsymbol{B}}(\boldsymbol{k}) \,, \tag{2.A.2}$$

with Fourier coefficients

$$\tilde{\boldsymbol{B}}(\boldsymbol{k}) = \frac{1}{L} \int d^2\boldsymbol{r}\, \mathrm{e}^{\mathrm{i}\boldsymbol{k}\cdot\boldsymbol{r}} \boldsymbol{B}(\boldsymbol{r}) \,. \tag{2.A.3}$$

Formally, the coarse-graining procedure is defined by

$$B_\mu(\boldsymbol{r}) = \sum_{\boldsymbol{r}'} B_{\boldsymbol{r}',\mu} \mathcal{K}_w(\boldsymbol{r} - \boldsymbol{r}') \,, \tag{2.A.4}$$

where $\mathcal{K}_w$ is a coarse-graining kernel with width $w$ on the order of a few lattice spacings, and normalization

$$\int d^2\boldsymbol{r}\, \mathcal{K}_w(\boldsymbol{r} - \boldsymbol{r}') = 1. \tag{2.A.5}$$

Hence, the Fourier coefficient

$$\tilde{B}_\mu(\mathbf{0}) = \frac{1}{L}\int d^2\boldsymbol{r}\, B_\mu(\boldsymbol{r}) \tag{2.A.6}$$

$$= \frac{1}{L}\sum_{\boldsymbol{r}'} B_{\boldsymbol{r}',\mu}\int d^2\boldsymbol{r}\, \mathcal{K}_w(\boldsymbol{r}-\boldsymbol{r}') \tag{2.A.7}$$

$$= \Phi_\mu\,, \tag{2.A.8}$$

where $\Phi_\mu$ is the flux defined by Eq. (2.7).

In terms of the Fourier coefficients, the action becomes

$$S_{\mathrm{SDM}}[\boldsymbol{B}] = \sum_{\boldsymbol{k}} \frac{\kappa}{2}|\tilde{\boldsymbol{B}}(\boldsymbol{k})|^2\,. \tag{2.A.9}$$

The probability of flux $\boldsymbol{\Phi}$ is obtained by integrating out all other Fourier modes with $\boldsymbol{k} \neq \mathbf{0}$, so

$$P(\boldsymbol{\Phi}) = \int \prod_{\boldsymbol{k}\neq\mathbf{0}} d^2\tilde{\boldsymbol{B}}(\boldsymbol{k})\, P[\boldsymbol{B}] \tag{2.A.10}$$

$$= \frac{\mathrm{e}^{-\frac{\kappa}{2}\boldsymbol{\Phi}^2}}{\sum_{\boldsymbol{\Phi}} \mathrm{e}^{-\frac{\kappa}{2}\boldsymbol{\Phi}^2}}\,, \tag{2.A.11}$$

where $\Phi_\mu$ is integer valued. As expected, the mean flux vanishes while the mean-square flux is given by [10]

$$\langle|\boldsymbol{\Phi}|^2\rangle = 2\frac{\sum_{n\in\mathbb{Z}} n^2 \mathrm{e}^{-\frac{\kappa}{2}n^2}}{\sum_{n\in\mathbb{Z}} \mathrm{e}^{-\frac{\kappa}{2}n^2}}\,. \tag{2.A.12}$$

Unlike in the case of the cubic lattice [11], the discreteness of the flux is important in two dimensions and the sum over flux sectors cannot be converted into an integral.

### 2.A.2 DDM flux in the Coulomb phase

The generalization to flux moments in the DDM Coulomb phase is straightforward. The DDM Coulomb phase action is

$$S_{\mathrm{DDM}} = \int d^2\boldsymbol{r}\, \left[\frac{\kappa_+}{2}|\boldsymbol{B}^{(+)}|^2 + \frac{\kappa_-}{2}|\boldsymbol{B}^{(-)}|^2\right]\,, \tag{2.A.13}$$

and the probability associated with magnetic fields $\boldsymbol{B}^{(\pm)}(\boldsymbol{r})$ is $P[\boldsymbol{B}^{(+)},\boldsymbol{B}^{(-)}] = \mathrm{e}^{-S_{\mathrm{DDM}}[\boldsymbol{B}^{(+)},\boldsymbol{B}^{(-)}]}/Z$, where $Z$ is the partition function.

After Fourier expansion of $\boldsymbol{B}^{(\pm)}(\boldsymbol{r})$ in terms of Fourier coefficients $\tilde{\boldsymbol{B}}^{(\pm)}(\boldsymbol{k})$, where $\tilde{\boldsymbol{B}}^{(\pm)}(\boldsymbol{0}) = \boldsymbol{\Phi}^{(\pm)}$, the action becomes

$$S_{\mathrm{DDM}} = \sum_{\boldsymbol{k}} \left[ \frac{\kappa_+}{2} |\tilde{\boldsymbol{B}}^{(+)}(\boldsymbol{k})|^2 + \frac{\kappa_-}{2} |\tilde{\boldsymbol{B}}^{(-)}(\boldsymbol{k})|^2 \right] . \tag{2.A.14}$$

The probability of fluxes $\boldsymbol{\Phi}^{(\pm)}$ is obtained by integrating out all other Fourier modes with $\boldsymbol{k} \neq \boldsymbol{0}$, so

$$P(\boldsymbol{\Phi}^{(+)},\boldsymbol{\Phi}^{(-)}) = \frac{\mathrm{e}^{-\frac{\kappa_+}{2}|\boldsymbol{\Phi}^{(+)}|^2} \mathrm{e}^{-\frac{\kappa_-}{2}|\boldsymbol{\Phi}^{(-)}|^2}}{\sum_{\boldsymbol{\Phi}^{(1)},\boldsymbol{\Phi}^{(2)}} \mathrm{e}^{-\frac{\kappa_+}{2}|\boldsymbol{\Phi}^{(+)}|^2} \mathrm{e}^{-\frac{\kappa_-}{2}|\boldsymbol{\Phi}^{(-)}|^2}} , \tag{2.A.15}$$

where $\Phi_\mu^{(1,2)}$ are integer valued (we avoid summing over $\Phi_\mu^{(\pm)} = \Phi_\mu^{(1)} \pm \Phi_\mu^{(2)}$, which are instead pairs of integers with the same parity). Again, the mean flux vanishes while the mean-square total and relative flux are given by

$$\langle |\boldsymbol{\Phi}^{(\pm)}|^2 \rangle = 2 \frac{\sum_{n_1,n_2\in\mathbb{Z}} n_\pm^2 \mathrm{e}^{-\frac{\kappa_+}{2}n_+^2} \mathrm{e}^{-\frac{\kappa_-}{2}n_-^2}}{\sum_{n_1,n_2\in\mathbb{Z}} \mathrm{e}^{-\frac{\kappa_+}{2}n_+^2} \mathrm{e}^{-\frac{\kappa_-}{2}n_-^2}} , \tag{2.A.16}$$

where $n_\pm = n_1 \pm n_2$.

### 2.A.3 SDM $G_{\mathbf{m}}(\boldsymbol{R})$ in the Coulomb phase

Next, we calculate the monomer distribution function in the SDM Coulomb phase (see also Refs. [4, 7]). In the continuum description, this is given by

$$G_{\mathrm{m}}(\boldsymbol{R}) = \frac{1}{Z} \int \mathcal{D}\boldsymbol{B}(\boldsymbol{r})\, \mathrm{e}^{-S_{\mathrm{SDM}}[\boldsymbol{B}]} , \tag{2.A.17}$$

where $Z$ is the partition function in the close-packed case, $S_{\mathrm{SDM}}$ is given by Eq. (2.A.1) and $\boldsymbol{B}$ is now the magnetic field in the presence of a pair of test monomers, i.e., $\boldsymbol{\nabla}\cdot\boldsymbol{B} = Q(\boldsymbol{r})$ with $Q(\boldsymbol{r}) = \mathcal{K}_w(\boldsymbol{r}-\boldsymbol{r}_+) - \mathcal{K}_w(\boldsymbol{r}-\boldsymbol{r}_-)$ [this follows from coarse graining Eq. (2.5) with $Q_{\boldsymbol{r}} = \delta_{\boldsymbol{r},\boldsymbol{r}_+} - \delta_{\boldsymbol{r},\boldsymbol{r}_-}$].

The general solution for the magnetic field is [65]

$$B_\mu = -\partial_\mu \phi + \epsilon_{\mu\nu}\partial_\nu h , \tag{2.A.18}$$

where $\phi$ is fixed by the Poisson equation $\nabla^2\phi = -Q(\boldsymbol{r})$, and $h$ is a Coulomb phase height. After simplification, the action reads

$$S_{\mathrm{SDM}} = \int d^2\boldsymbol{r}\, \frac{\kappa}{2}\left(|\boldsymbol{\nabla}\phi|^2 + |\boldsymbol{\nabla}h|^2\right) \tag{2.A.19}$$

(cross terms vanish after integration by parts) and, since the second contribution returns $Z$, Eq. (2.A.17) reduces to

$$G_{\mathrm{m}}(\boldsymbol{R}) = \mathrm{e}^{-\int d^2\boldsymbol{r}\, \frac{\kappa}{2}|\boldsymbol{\nabla}\phi|^2}\,. \tag{2.A.20}$$

The remaining integral is the energy associated with an electrostatic potential $\phi$ due to two extended charge distributions $\pm\mathcal{K}_w$ separated by $\boldsymbol{R} = \boldsymbol{r}_+ - \boldsymbol{r}_-$ [66]. For large monomer separation $|\boldsymbol{R}| \gg w$, the charge distributions 'see' one another as point charges, hence (in two dimensions)

$$\int d^2\boldsymbol{r}\, \frac{1}{2}|\boldsymbol{\nabla}\phi|^2 = \frac{1}{2\pi}\log|\boldsymbol{R}|\,, \tag{2.A.21}$$

up to additive constants, and the asymptotic behavior is

$$G_{\mathrm{m}}(\boldsymbol{R}) \sim |\boldsymbol{R}|^{-\kappa/2\pi}\,. \tag{2.A.22}$$

### 2.A.4 DDM $G_{\mathbf{m}}(\boldsymbol{R})$ in the Coulomb phase

By extension, the monomer distribution function in the DDM Coulomb phase, with a pair of monomers in one replica, say $\alpha = 1$, is given by

$$G_{\mathrm{m}}(\boldsymbol{R}) = \frac{1}{Z}\int \mathcal{D}\boldsymbol{B}^{(+)}(\boldsymbol{r})\mathcal{D}\boldsymbol{B}^{(-)}(\boldsymbol{r})\, \mathrm{e}^{-S_{\mathrm{DDM}}[\boldsymbol{B}^{(+)},\boldsymbol{B}^{(-)}]}\,, \tag{2.A.23}$$

where $Z$ is the partition function in the close-packed case, $S_{\mathrm{DDM}}$ is given by Eq. (2.A.13) and $\boldsymbol{\nabla}\cdot\boldsymbol{B}^{(\pm)} = Q(\boldsymbol{r})$ [because $\boldsymbol{B}^{(\pm)} = \boldsymbol{B}^{(1)} \pm \boldsymbol{B}^{(2)}$, $\boldsymbol{\nabla}\cdot\boldsymbol{B}^{(1)} = Q(\boldsymbol{r})$, and $\boldsymbol{\nabla}\cdot\boldsymbol{B}^{(2)} = 0$].

The calculation proceeds as in the previous section, now with two fields $\boldsymbol{B}^{(\pm)}$ and their stiffnesses $\kappa_\pm$, giving

$$G_{\mathrm{m}}(\boldsymbol{R}) \sim |\boldsymbol{R}|^{-\eta}\,, \tag{2.A.24}$$

where $2\pi\eta = \kappa_+ + \kappa_-$. As required, this reduces to Eq. (2.A.22) when $K = 0$ [since then $\kappa_\pm = \frac{\kappa}{2}$ from Eq. (2.16)].

### 2.A.5 DDM $G_{\mathrm{d}}(\boldsymbol{R})$ in the (anti)synchronized phases

Finally, we calculate the double monomer distribution function in the DDM (anti)synchronized phases. In these phases, the cosine term in Eq. (2.18) is relevant and locks the relative height to values $h^{(-)} = 0\,(\frac{1}{2})$. Hence, from the continuum version of Eq. (2.6), the corresponding magnetic field $\boldsymbol{B}^{(-)} = 0$. For the total magnetic field, this implies $\boldsymbol{B}^{(+)} = 2\boldsymbol{B}^{(1)}$, since the cosine term in Eq. (2.20) is irrelevant. In this case, Eq. (2.A.13) reduces to

$$S_{\mathrm{DDM}} = \int d^2\boldsymbol{r}\, 2\kappa_+ |\boldsymbol{B}^{(1)}|^2 \,, \tag{2.A.25}$$

which is the correct action for the (anti)synchronized phases.

In terms of this, the continuum version of the double monomer distribution function is

$$G_{\mathrm{d}}(\boldsymbol{R}) = \frac{1}{Z} \int \mathcal{D}\boldsymbol{B}^{(1)}(\boldsymbol{r})\, \mathrm{e}^{-S_{\mathrm{DDM}}[\boldsymbol{B}^{(1)}]} \,, \tag{2.A.26}$$

where $Z$ is the partition function in the close-packed case and $\boldsymbol{B}^{(1)} = \boldsymbol{B}^{(2)}$ is the magnetic field in the presence of a pair of test monomers, i.e., $\boldsymbol{\nabla} \cdot \boldsymbol{B}^{(1)} = Q(\boldsymbol{r})$. The derivation proceeds as in Appendix 2.A.3 but with $\kappa \to 4\kappa_+$, and the asymptotic behavior is

$$G_{\mathrm{d}}(\boldsymbol{R}) \sim |\boldsymbol{R}|^{-2\kappa_+/\pi} \,. \tag{2.A.27}$$

# Chapter 3

# Topological sectors, dimer correlations and monomers from the transfer-matrix solution of the dimer model

## 3.1 Introduction

Noninteracting classical dimer models in two dimensions were first solved independently by Kasteleyn [12, 24] and Temperley and Fisher [25, 26] in 1961 using a combinatoric method, in which the partition function is expressed as the Pfaffian of a signed adjacency matrix known as the Kasteleyn matrix. Because they are exactly solvable, these models offer a useful setting to explore the physics of Coulomb phases [6]. In particular, using the Pfaffian method Fisher and Stephenson have calculated dimer occupation numbers, dimer–dimer correlation functions and the mononomer distribution function in 1963 [29], while, more recently, Boutillier and de Tilière have calculated partial partition functions for the topological sectors [28].

Perhaps a more elegant solution of the dimer model is Lieb's transfer-matrix method [23], analogous to the well-known solution of the Ising model by Schultz *et al.* [67], which maps the problem to free fermions. In this approach, the partition function is expressed in terms of a transfer matrix, which, given a configuration

on a row of vertical bonds, generates all dimer configurations compatible with the close-packing constraint on the subsequent row of horizontal and vertical bonds. This can be expressed in terms of spin-$\frac{1}{2}$ operators and mapped to fermions through a Jordan–Wigner transformation.

This method has been used in the literature to derive the partition function [23] and to determine its vertical-flux decomposition [68, 69]. In this chapter, we show how Lieb's transfer matrix can be modified in order to calculate the full flux-sector decomposition. We also provide a general framework for the calculation of expectation values and explicitly calculate dimer occupation numbers, dimer–dimer correlation functions and the monomer distribution function. For the last of these, we show how the asymptotic dependence for large monomer separation, which was only deduced by numerical means in Ref. [29], can be evaluated exactly by applying the Fisher–Hartwig conjecture [70].

This chapter is organized as follows: In Sec. 3.2 we define the model before showing how it can be formulated in terms of a transfer matrix in Sec. 3.3. We then diagonalize the two-row transfer matrix in Sec. 3.4, whose spectrum is used to calculate the partition function, including its flux-sector decomposition, in Sec. 3.5, and various expectation values in Sec. 3.6. We conclude in Sec. 3.7.

## 3.2 Model

We consider the standard close-packed dimer model on an $L_x \times L_y$ square lattice with PBCs, assuming both $L_x$, $L_y$ even (we will return to the interacting double dimer model in Sec. 4.3). To each configuration, we assign weight $\alpha^{N_x} \mathrm{e}^{\mathrm{i}\boldsymbol{t}\cdot\boldsymbol{\Phi}}$. In the first factor $\alpha > 0$ and $N_x$ are the 'activity' and number of horizontal dimers, respectively (the activity of vertical dimers is unity). Hence, for $\alpha \neq 1$, the model is anisotropic, with horizontal (vertical) dimers favored for $\alpha > 1$ ($\alpha < 1$). In the second factor $\boldsymbol{t}$ is a field, with components $t_\mu \in (-\pi, \pi]$, that couples to the flux $\boldsymbol{\Phi}$, which was defined Sec. 2.2.1. An example configuration is shown in Fig. 3.1.

The partition function is

$$Z(\boldsymbol{t}) = \sum_{c \in \mathfrak{C}_0} \alpha^{N_x} \mathrm{e}^{\mathrm{i}\boldsymbol{t}\cdot\boldsymbol{\Phi}} , \tag{3.1}$$

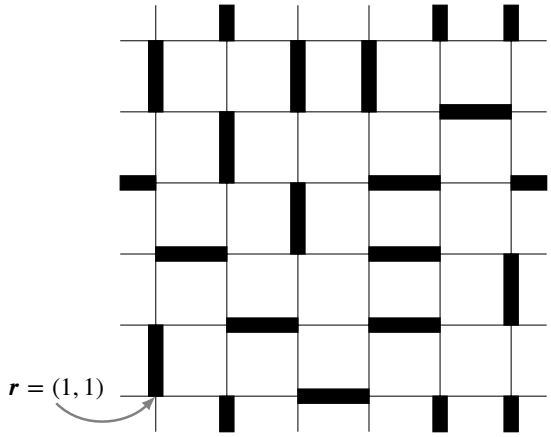


Figure 3.1: An example configuration of the close-packed dimer model on a $6 \times 6$ lattice with PBCs. The number of horizontal dimers is $N_x = 8$ and the flux is $\boldsymbol{\Phi} = (1, 1)$ [see Eq. (2.7) and text thereafter]. Hence, this configuration has weight $\alpha^8 \mathrm{e}^{\mathrm{i}\boldsymbol{t}\cdot(1,1)}$.

where $\mathfrak{C}_0$ denotes the set of all close-packed dimer configurations, and can be thought of as a moment-generating function for $\Phi_\mu$. Similarly, expectation values of a function $O$ of the dimer occupation numbers $d_{\boldsymbol{r},\mu}$ are given by

$$\langle O \rangle = \frac{1}{Z(\boldsymbol{t})} \sum_{c \in \mathfrak{C}_0} O \alpha^{N_x} \mathrm{e}^{\mathrm{i}\boldsymbol{t}\cdot\boldsymbol{\Phi}} \,. \tag{3.2}$$

## 3.3 Transfer matrix

We construct the partition function, Eq. (3.1), by modifying Lieb's transfer matrix [23] to include the $\Phi_x$ weighting (the $\Phi_y$ weighting can be included without modifying the transfer matrix).

We first define a vector space whose basis vectors $|\bar{\boldsymbol{d}}_y\rangle$ correspond to all possible configurations $\bar{\boldsymbol{d}}_y$ of the dimer occupation numbers on a single row of vertical bonds. As illustrated in Fig. 3.2, the transfer matrix $V$ is defined so that

$$V|\bar{\boldsymbol{d}}_y\rangle = \sum_{\bar{\boldsymbol{d}}'_y} |\bar{\boldsymbol{d}}'_y\rangle \sum_{\bar{\boldsymbol{d}}_x \in \mathfrak{C}(\bar{\boldsymbol{d}}_y, \bar{\boldsymbol{d}}'_y)} w(\bar{\boldsymbol{d}}_x) \,, \tag{3.3}$$

where $\bar{\boldsymbol{d}}'_y$ is the configuration on the subsequent row of vertical bonds and $\mathfrak{C}(\bar{\boldsymbol{d}}_y, \bar{\boldsymbol{d}}'_y)$ is the (possibly empty) set of configurations $\bar{\boldsymbol{d}}_x$ of the intermediate row of horizontal bonds that are compatible with $\bar{\boldsymbol{d}}_y$ and $\bar{\boldsymbol{d}}'_y$. The weight function

$w$ is chosen to give the correct weights for $N_x$ and $\Phi_x$ in the partition function of Eq. (3.1). On even rows, where $\epsilon_{\boldsymbol{r}} = (-1)^{r_x}$ in Eq. (2.7), it is given by

$$w(\bar{\boldsymbol{d}}_x) = \prod_{j=1}^{L_x} \mu_j^{\bar{d}_{j,x}} \,, \tag{3.4}$$

where

$$\mu_j = \alpha \exp\left[\mathrm{i}(-1)^j \frac{t_x}{L_x}\right] \,, \tag{3.5}$$

while on odd rows $w$ is defined in the same way, but with $\mu_j$ replaced by $\mu_j^*$. (Here, $\bar{d}_{j,x}$ denotes the occupation number of the bond between sites $r_x = j$ and $j+1$ in the configuration $\bar{\boldsymbol{d}}_x$ of the horizontal bonds.)

It is convenient to split the action of $V$ into two steps:

1. Generate the (single) configuration $\bar{\boldsymbol{d}}'_y = (1, 1, \ldots, 1) - \bar{\boldsymbol{d}}_y$ with all horizontal bonds on the intermediate row empty (left configuration in Fig. 3.2).

2. Starting with the result of step 1, one may produce all other configurations by replacing pairs of neighboring vertical dimers with a horizontal dimer (middle and right configurations in Fig. 3.2). The effect on $\bar{\boldsymbol{d}}'_y$ is that an adjacent pair of dimers is removed.

In order to reproduce the weight function $w$, a horizontal dimer on the bond between sites $j$ and $j+1$ in step 2 comes with a factor $\mu_j$ ($\mu_j^*$) on even (odd) rows.

An explicit operator expression for the transfer matrix is obtained by representing occupied and empty vertical bonds by spin up $|\uparrow\rangle$ and down $|\downarrow\rangle$ states, respectively [i.e., eigenstates of $\sigma_j^z$, where $\boldsymbol{\sigma}_j = (\sigma_j^x, \sigma_j^y, \sigma_j^z)$ are the Pauli matrices]. The above steps are easy to formulate in the spin language. As shown in Fig. 3.2, step 1 is equivalent to flipping all spins, which is achieved by the operator

$$V_1 = \prod_{j=1}^{L_x} \sigma_j^x \,, \tag{3.6}$$

since $\sigma_j^{\pm} = \frac{1}{2}(\sigma_j^x \pm i\sigma_j^y)$ satisfy $\sigma^+|\downarrow\rangle = |\uparrow\rangle$ and $\sigma^-|\uparrow\rangle = |\downarrow\rangle$.

In step 2, pairs of neighboring up spins are flipped, so the operator

$$d_{j,x} = \mu_j \sigma_j^- \sigma_{j+1}^- \tag{3.7}$$

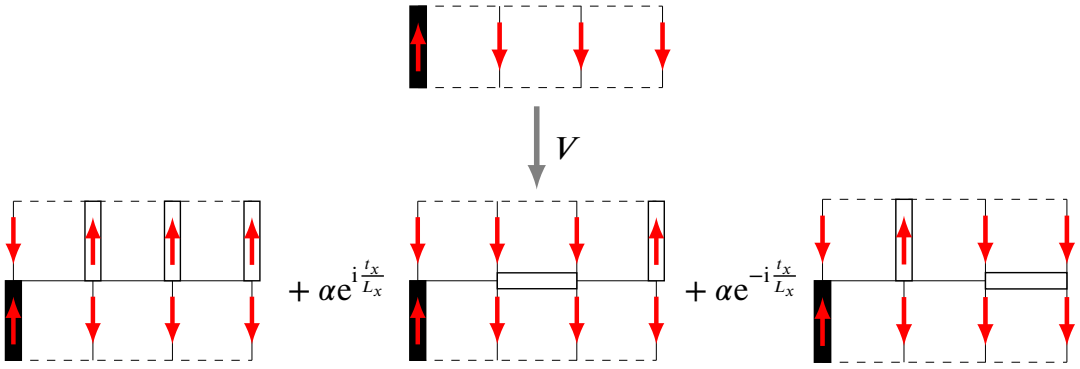


Figure 3.2: Action of the transfer matrix $V$ of Eq. (3.9) on a row of vertical bonds (top), in which occupied and empty vertical bonds are represented by spin up $|\uparrow\rangle$ and down $|\downarrow\rangle$ states (red), respectively. The result is all dimer configurations on the subsequent row of vertical bonds that are consistent with the close-packing constraint (bottom). The left configuration with all dimers vertical is generated by $V_1$, which flips all spins. The middle and right configurations, obtained from the left configuration by replacing pairs of neighboring vertical dimers with horizontal dimers, are generated by $V_3$, which flips neighboring up spins. In order to obtain the correct weights in the partition function, Eq. (3.1), $V$ and $V^* = V^\dagger$ act on alternate rows and assign weight $\mu_j = \alpha \exp\left[\mathrm{i}t_x(-1)^j/L_x\right]$ and $\mu_j^*$ to a horizontal dimer between sites $j$ and $j+1$, respectively.

effectively generates a horizontal dimer between sites $j$ and $j+1$, with the correct weight on even rows. Because $(\sigma_j^-)^2 = 0$, the operator $(m!)^{-1}\left(\sum_{j=1}^{L_x} d_{j,x}\right)^m$ generates $m$ horizontal dimers (PBCs require $\sigma_{L_x+1}^- = \sigma_1^-$), and hence

$$V_3 = \exp\left(\sum_{j=1}^{L_x} d_{j,x}\right) \tag{3.8}$$

generates an arbitrary number of horizontal dimers. To obtain the correct weights on odd rows, one should instead use the operator $V_3^*$.

It is therefore necessary to define two transfer matrices,

$$V = V_3 V_1 \tag{3.9}$$

on even rows and $V^* = V^\dagger$ on odd rows.[1] We also define the two-row transfer matrix

$$W = VV^\dagger\,, \tag{3.10}$$

[1]Lieb's transfer matrix $V = V_3V_2V_1$ includes a third operator $V_2$, which generates an arbitrary number of monomers on a row [23].

which is manifestly Hermitian, and can be simplified to

$$W = V_3 V_3^\dagger \tag{3.11}$$

after using $\sigma^x \sigma^- \sigma^x = \sigma^+$ to eliminate $V_1$.

The $\Phi_y$ weighting is included in the transfer-matrix formalism as follows: The operator for the dimer occupation number on a vertical bond is simply

$$d_{j,y} = \frac{1}{2}(1 + \sigma_j^z)\,, \tag{3.12}$$

since spin up (down) corresponds to an occupied (empty) bond. In terms of this, the vertical flux component on even rows is [see Eq. (2.7) and text thereafter]

$$\Phi_y = \sum_{j=1}^{L_x} (-1)^j d_{j,y}\,, \tag{3.13}$$

which satisfies the (anti)commutation relations $\{\Phi_y, V\} = 0$ and $[\Phi_y, W] = 0$.[2] The latter implies that it is possible to construct mutual eigenstates of the two-row transfer matrix $W$ and $\Phi_y$. The partition function, Eq. (3.1), is then given by

$$Z(\boldsymbol{t}) = \mathrm{Tr}\left[\mathrm{e}^{\mathrm{i}t_y \Phi_y} W^{\frac{L_y}{2}}\right] \tag{3.14}$$

(the trace arises due to PBCs in the vertical direction).

Similarly, the operator analog of Eq. (3.2), in the case of the correlation function between observables $O$ and $O'$ in rows $1 \le l \le l' \le L_y$, is given by

$$\langle O'(l')O(l)\rangle = \frac{1}{Z(\boldsymbol{t})}\,\mathrm{Tr}\left[\mathrm{e}^{\mathrm{i}t_y \Phi_y} W^{\frac{L_y}{2}} O'(l')O(l)\right]\,, \tag{3.15}$$

where $O(l) = U(l)^{-1} O U(l)$ and

$$U(l) = \underbrace{\cdots V^\dagger V V^\dagger}_{l} = \begin{cases} V^\dagger W^{(l-1)/2} & \text{for } l \text{ odd} \\ W^{l/2} & l \text{ even.} \end{cases} \tag{3.16}$$

Note that $[O(l)]^\dagger = O^\dagger(-l)$, where $U(-l) = [U(l)^\dagger]^{-1}$ is defined by the second

[2] $\Phi_y$ appears in Refs. [68, 69, 71] as the operator $\mathcal{V}$, whose eigenvalues are referred to as the 'variation index'.

equality of Eq. (3.16).

To compute expectation values of dimer observables, it is necessary to find operators that correspond to these quantities. While a suitable operator for the dimer occupation number on vertical bonds has already been defined in Eq. (3.12), no such operator exactly represents the dimer occupation number on horizontal bonds, since the vector space on which the transfer matrix acts contains only dimer configurations on vertical bonds.

One can nonetheless calculate expectation values involving horizontal dimers using an appropriately constructed operator. From Eqs. (3.3) and (3.4), one finds

$$\mu_j \frac{\partial}{\partial \mu_j} V |\bar{\boldsymbol{d}}_y\rangle = \sum_{\bar{\boldsymbol{d}}'_y} |\bar{\boldsymbol{d}}'_y\rangle \sum_{\bar{\boldsymbol{d}}_x \in \mathfrak{C}(\bar{\boldsymbol{d}}_y, \bar{\boldsymbol{d}}'_y)} \bar{d}_{j,x} w(\bar{\boldsymbol{d}}_x)\,, \tag{3.17}$$

whereas Eqs. (3.7)–(3.9) give the operator identity

$$\mu_j \frac{\partial}{\partial \mu_j} V = d_{j,x} V\,, \tag{3.18}$$

since $[d_{j,x}, d_{j',x}] = 0$. Comparing the right-hand sides, we therefore interpret $d_{j,x}$ as the operator corresponding to the horizontal dimer occupation number $\bar{d}_{j,x}$ on an even row, but only when appearing in the combination[3] $d_{j,x}V$. Similarly, $d^*_{j,x}$ acts as the horizontal dimer occupation number on an odd row in the combination $d^*_{j,x}V^\dagger$. Setting $O$ equal to $d_{j,x}$ ($d^*_{j,x}$) on even (odd) rows in Eq. (3.15) gives the correct combination $d_{j,x}V$ ($d^*_{j,x}V^\dagger$) in $O(l)$, allowing one to calculate expectation values involving the horizontal dimer number.

## 3.4 Diagonalization of the two-row transfer matrix

To calculate Eq. (3.14) it is sufficient to diagonalize the two-row transfer matrix $W$. We do so in this section through a series of transformations.

We map between spins and spinless fermions using the Jordan–Wigner trans-

[3]This means that, for example, $d^2_{j,x}$ does not give the square of the horizontal dimer number; in fact $d^2_{j,x} = 0$, whereas $\bar{d}^2_{j,x} = \bar{d}_{j,x}$.

formation [72–74]

$$C_j = \left(\prod_{i=1}^{j-1} -\sigma_i^z\right)\sigma_j^- \tag{3.19}$$

$$C_j^\dagger = \left(\prod_{i=1}^{j-1} -\sigma_i^z\right)\sigma_j^+ \tag{3.20}$$

$$C_j^\dagger C_j = \frac{1}{2}(1+\sigma_j^z)\,, \tag{3.21}$$

which identifies spin up and down with filled and empty fermion orbitals, respectively, while preserving the usual (anti)commutation relations

$$[\sigma_i^\mu, \sigma_j^\nu] = 2i\delta_{ij}\epsilon_{\mu\nu\rho}\sigma_\rho \tag{3.22}$$

$$\{C_i, C_j\} = \{C_i^\dagger, C_j^\dagger\} = 0 \qquad \{C_i, C_j^\dagger\} = \delta_{ij}\,. \tag{3.23}$$

In terms of fermions, Eqs. (3.7) and (3.12) become

$$d_{j,x} = -\mu_j C_j C_{j+1} \tag{3.24}$$

$$d_{j,y} = C_j^\dagger C_j\,, \tag{3.25}$$

while the condition $\sigma_{L_x+1}^- = \sigma_1^-$ is equivalent to

$$C_{L_x+1} = -C_1(-1)^{\Phi_y} = (-1)^{\Phi_y}C_1 \tag{3.26}$$

with

$$\Phi_y = \sum_j (-1)^j C_j^\dagger C_j\,. \tag{3.27}$$

We now define projectors

$$\Pi_p = \frac{1}{2}[1+(-1)^p(-1)^{\Phi_y}] \tag{3.28}$$

into the subspaces with even ($p=0$) or odd ($p=1$) $\Phi_y$, which satisfy $\sum_p \Pi_p = 1$ and $(-1)^{\Phi_y}\Pi_p = (-1)^p\Pi_p$. Then, since $(-1)^{\Phi_y}$ commutes with any quadratic

form in fermions, we have

$$W = W \sum_p \Pi_p \tag{3.29}$$

$$= \sum_p W_p \Pi_p \,, \tag{3.30}$$

where

$$W_p = \exp\left( - \sum_{j=1}^{L_x} \mu_j C_j C_{j+1} \right) \times \text{h.c.} \,, \tag{3.31}$$

and the fermion operator $C_{L_x+1}$ depends implicitly on $p$ through the boundary condition

$$C_{L_x+1} = -(-1)^p C_1 . \tag{3.32}$$

More generally, for any operator $O$ containing $C_{L_x+1}$ of Eq. (3.26), we define an operator $O_p$ that instead only contains $C_{L_x+1}$ of Eq. (3.32) (and thus depends on $p$), such that the action of both operators on a state with $\Phi_y$ parity $p$ yields the same result, i.e., $O = \sum_p O_p \Pi_p$. (For operators that do not contain $C_{L_x+1}$, such as $\Phi_y$, one has $O_p = O$.)

For later reference (see Sec. 3.6) we note that, after the Jordan–Wigner transformation, the single-row transfer matrix is given by $V = \sum_p V_p \Pi_p$, with

$$V_p = \exp\left( - \sum_{j=1}^{L_x} \mu_j C_j C_{j+1} \right) \prod_{j=1}^{L_x} \left[ C_j + (-1)^j C_j^\dagger \right] \,, \tag{3.33}$$

where the operators in the product should be ordered from right to left.

We now make a Fourier expansion

$$C_j = \frac{\mathrm{e}^{-\mathrm{i}\pi/4}}{\sqrt{L_x}} \sum_{k \in \mathbb{K}_p} \mathrm{e}^{\mathrm{i}kj} \eta_k \,, \tag{3.34}$$

with

$$\mathbb{K}_0 = \{ \pm\pi/L_x, \pm 3\pi/L_x, \ldots, \pm(L_x - 1)\pi/L_x \} \tag{3.35}$$

and

$$\mathbb{K}_1 = \{ 0, \pm 2\pi/L_x, \pm 4\pi/L_x, \ldots, \pm(L_x - 2)\pi/L_x, \pi \} \,, \tag{3.36}$$

which ensure the correct boundary condition on $C_{L_x+1}$ in Eq. (3.32) [23].[4] The $\eta_k$ fermions obey standard anticommutation relations, as follows from Eq. (3.23).

Using the result

$$\frac{1}{L_x}\sum_{j=1}^{L_x}\mu_j \mathrm{e}^{\mathrm{i}(k+k')j} = \alpha\left[\delta_{k+k',0}\cos\left(\frac{t_x}{L_x}\right) + \mathrm{i}\delta_{k+k',\pi}\sin\left(\frac{t_x}{L_x}\right)\right], \tag{3.37}$$

valid for both $k$ and $k'$ in either $\mathbb{K}_0$ or $\mathbb{K}_1$, the operator appearing in the exponential of Eq. (3.31) can be written as

$$-\sum_{j=1}^{L_x}\mu_j C_j C_{j+1} = \mathrm{i}\alpha\sum_{k\in\mathbb{K}_p}\mathrm{e}^{-\mathrm{i}k}\eta_k\left[\cos\left(\frac{t_x}{L_x}\right)\eta_{-k} - \mathrm{i}\sin\left(\frac{t_x}{L_x}\right)\eta_{\pi-k}\right]. \tag{3.38}$$

Restricting the sum to $0 \le k \le \frac{\pi}{2}$, this becomes

$$-\sum_{j=1}^{L_x}\mu_j C_j C_{j+1} = \sum_{\substack{k\in\mathbb{K}_p \\ 0\le k\le\frac{\pi}{2}}} Q_k(\mathbf{A}(k)), \tag{3.39}$$

where the quadratic form

$$Q_k(\mathbf{X}) = \begin{cases} \frac{1}{2}\boldsymbol{\eta}_k^\dagger \mathbf{X}\boldsymbol{\eta}_k & \text{for } k \in \left\{0, \frac{\pi}{2}\right\} \\ \boldsymbol{\eta}_k^\dagger \mathbf{X}\boldsymbol{\eta}_k & \text{otherwise.} \end{cases} \tag{3.40}$$

Here,

$$\boldsymbol{\eta}_k = \begin{pmatrix} \eta_k \\ \eta_{k-\pi} \\ \eta_{-k}^\dagger \\ \eta_{\pi-k}^\dagger \end{pmatrix} \tag{3.41}$$

[its Hermitian conjugate means the row vector $\boldsymbol{\eta}_k^\dagger = (\eta_k^\dagger\ \eta_{k-\pi}^\dagger\ \eta_{-k}\ \eta_{\pi-k})$], while

[4] As an alternative to the approach in Sec. 3.3, one could instead construct the $\Phi_x$ weighting using $\mu_j = \alpha$ and $\sigma_{L_x+1}^- = \mathrm{e}^{\mathrm{i}t_x}\sigma_1^-$ in place of Eq. (3.5) and $\sigma_{L_x+1}^- = \sigma_1^-$, respectively [see Eq. (2.7) and text thereafter]. However, a Fourier expansion of the new set of fermions $\tilde{C}_j$ is no longer useful because of the absence of translation symmetry [75, 76]. Instead, one would have to perform the gauge transformation $\tilde{C}_j = \mathrm{e}^{-\mathrm{i}j(-1)^j t_x/L_x}C_j$ back to $C_j$ fermions, before proceeding as in the main text.

the $4 \times 4$ matrix

$$\mathbf{A}(k) = \begin{pmatrix} 0 & 0 \\ \mathbf{A}_{21} & 0 \end{pmatrix} , \tag{3.42}$$

with

$$\mathbf{A}_{21} = 2\alpha \begin{bmatrix} -\sin k \cos\left(\frac{t_x}{L_x}\right) & \cos k \sin\left(\frac{t_x}{L_x}\right) \\ -\cos k \sin\left(\frac{t_x}{L_x}\right) & \sin k \cos\left(\frac{t_x}{L_x}\right) \end{bmatrix} . \tag{3.43}$$

The additional factor of $\frac{1}{2}$ for $k \in \{0, \frac{\pi}{2}\}$ prevents double counting of these terms in Eq. (3.39), and ensures the commutation relation

$$[Q_k(\mathbf{X}), Q_{k'}(\mathbf{Y})] = \delta_{kk'} Q_k\left([\mathbf{X}, \mathbf{Y}]\right) , \tag{3.44}$$

is valid for all $0 \leq k \leq \frac{\pi}{2}$.[5]

Since $Q_k^\dagger(\mathbf{X}) = Q_k(\mathbf{X}^\dagger)$, and all quadratic forms in Eq. (3.39) commute by Eq. (3.44), the two-row transfer matrix, Eq. (3.31), is given by

$$W_p = \left[ \prod_{\substack{k \in \mathbb{K}_p \\ 0 \leq k \leq \frac{\pi}{2}}} \mathrm{e}^{Q_k(\mathbf{A}(k))} \right] \left[ \prod_{\substack{k \in \mathbb{K}_p \\ 0 \leq k \leq \frac{\pi}{2}}} \mathrm{e}^{Q_k(\mathbf{A}^\dagger(k))} \right] , \tag{3.47}$$

which can be reordered as the following product of commuting terms:

$$W_p = \prod_{\substack{k \in \mathbb{K}_p \\ 0 \leq k \leq \frac{\pi}{2}}} \mathrm{e}^{Q_k(\mathbf{A}(k))} \mathrm{e}^{Q_k(\mathbf{A}^\dagger(k))} . \tag{3.48}$$

To proceed, we map to the corresponding one-dimensional quantum Hamiltonian $\mathcal{H}$ through

$$W = \mathrm{e}^{-2\mathcal{H}} . \tag{3.49}$$

[5]For $k \in \{0, \frac{\pi}{2}\}$, because of the nonzero anticommutator $\{\eta_{k,i}, \eta_{k,j}\} = (\mathbf{W}_k)_{i,j}$, where

$$\mathbf{W}_0 = \boldsymbol{\sigma}^x \otimes I_2 \qquad\qquad \mathbf{W}_{\pi/2} = \boldsymbol{\sigma}^x \otimes \boldsymbol{\sigma}^x , \tag{3.45}$$

with $\otimes$ denoting the Kronecker product, Eq. (3.44) is only true if $\mathbf{X}$ satisfies the condition $\mathbf{W}_k \mathbf{X}^T \mathbf{W}_k = -\mathbf{X}$ (or the same for $\mathbf{Y}$). However, it is always possible to symmetrize $\mathbf{X}$ to meet this condition: Using $(\boldsymbol{\eta}_k^\dagger)^T = \mathbf{W}_k \boldsymbol{\eta}_{k,j}$, one can show

$$Q_k(\mathbf{X}) = Q_k(\mathbf{X}') + \frac{1}{2} \operatorname{Tr}(\mathbf{W}_k \mathbf{X}^T \mathbf{W}_k) , \tag{3.46}$$

where $\mathbf{X}' = \frac{1}{2}(\mathbf{X} - \mathbf{W}_k \mathbf{X}^T \mathbf{W}_k)$ is a matrix that satisfies the condition. The matrix $\mathbf{A}(k)$ in Eq. (3.42) has been constructed in this way.

Then, by Eq. (3.30), we have

$$\mathcal{H} = \sum_p \mathcal{H}_p \Pi_p \,, \tag{3.50}$$

where

$$W_p = \mathrm{e}^{-2\mathcal{H}_p} \,, \tag{3.51}$$

since the projectors satisfy $[\Pi_p, W_{p'}] = 0$ and $\Pi_p \Pi_{p'} = \Pi_p \delta_{pp'}$. After inserting Eq. (3.48), this implies

$$\mathcal{H}_p = -\frac{1}{2} \sum_{\substack{k \in \mathbb{K}_p \\ 0 \leq k \leq \frac{\pi}{2}}} \log \left[ \mathrm{e}^{Q_k(\mathbf{A}(k))} \mathrm{e}^{Q_k(\mathbf{A}^\dagger(k))} \right] . \tag{3.52}$$

The Baker–Campbell–Hausdorff formula [77] states that the logarithm in Eq. (3.52) can be expressed in terms of nested commutators of $Q_k(\mathbf{A})$ and $Q_k(\mathbf{A}^\dagger)$. Using Eq. (3.44), these can be expressed in terms of nested commutators of $\mathbf{A}$ and $\mathbf{A}^\dagger$, giving

$$\mathcal{H}_p = -\frac{1}{2} \sum_{\substack{k \in \mathbb{K}_p \\ 0 \leq k \leq \frac{\pi}{2}}} Q_k \left( \log(\mathrm{e}^{\mathbf{A}(k)} \mathrm{e}^{\mathbf{A}^\dagger(k)}) \right) . \tag{3.53}$$

The problem is thus reduced to diagonalization of the $4 \times 4$ matrix $\mathrm{e}^{\mathbf{A}} \mathrm{e}^{\mathbf{A}^\dagger}$ for each $k$.

In order to solve the eigenvalue problem

$$\mathrm{e}^{\mathbf{A}} \mathrm{e}^{\mathbf{A}^\dagger} \boldsymbol{v} = \lambda \boldsymbol{v} \,, \tag{3.54}$$

we expand $\mathrm{e}^{\mathbf{A}}$ as a power series and use $\mathbf{A}^2 = 0$ to obtain

$$\mathrm{e}^{\mathbf{A}} \mathrm{e}^{\mathbf{A}^\dagger} = \mathbf{I} + \mathbf{A} + \mathbf{A}^\dagger + \mathbf{A}\mathbf{A}^\dagger \,. \tag{3.55}$$

After substituting Eq. (3.42) and writing $\boldsymbol{v} = (\boldsymbol{v}_1 \ \boldsymbol{v}_2)^T$, Eq. (3.54) reduces to a

pair of simultaneous equations which, on rearrangement, read

$$\boldsymbol{v}_1 = \frac{1}{\lambda - 1}\mathbf{A}_{21}^\dagger \boldsymbol{v}_2 \tag{3.56}$$

$$\mathbf{A}_{21}\mathbf{A}_{21}^\dagger \boldsymbol{v}_2 = \frac{(\lambda-1)^2}{\lambda}\boldsymbol{v}_2\,. \tag{3.57}$$

The latter is a $2\times 2$ eigenvalue problem, which is easily solved. The result implies

$$\mathrm{e}^{\mathbf{A}}\mathrm{e}^{\mathbf{A}^\dagger} = \mathbf{U}\,\mathrm{diag}[\lambda_-(k - t_x/L_x), \lambda_+(k - t_x/L_x), \lambda_-(k + t_x/L_x), \lambda_+(k + t_x/L_x)]\mathbf{U}^\dagger\,, \tag{3.58}$$

where

$$\lambda_\pm(k) = \left[\alpha \sin k \pm (1 + \alpha^2 \sin^2 k)^{\frac{1}{2}}\right]^2\,, \tag{3.59}$$

and $\mathbf{U}$ is a unitary matrix whose columns are the eigenvectors of $\mathrm{e}^{\mathbf{A}}\mathrm{e}^{\mathbf{A}^\dagger}$.

By inserting Eq. (3.58) into Eq. (3.53), we obtain the free-fermion Hamiltonian

$$\mathcal{H}_p = \sum_{k\in\mathbb{K}_p} \epsilon(k - t_x/L_x)\zeta_k^\dagger\zeta_k\,, \tag{3.60}$$

with dispersion

$$\epsilon(k) = \frac{1}{2}\log\lambda_+(k) = \sinh^{-1}(\alpha\sin k)\,, \tag{3.61}$$

where the $\zeta_k$ and $\eta_k$ fermions are related by the Bogoliubov transformation

$$\boldsymbol{\zeta}_k = \begin{pmatrix} \zeta_k \\ \zeta_{k-\pi} \\ \zeta_{-k}^\dagger \\ \zeta_{\pi-k}^\dagger \end{pmatrix} = \mathbf{U}^\dagger\boldsymbol{\eta}_k\,, \tag{3.62}$$

for $0 \le k \le \pi/2$. Both sets of fermions obey standard anticommutation relations.

The transformation of Eq. (3.62) may be expressed as a single transformation valid for all $k$:

$$\eta_k = \frac{1}{\sqrt{2}}\Big(\cos\theta_{k-t_x/L_x}\zeta_k + \cos\theta_{k+t_x/L_x}\zeta_{-k}^\dagger - \sin\theta_{k+t_x/L_x}\zeta_{\pi-k}^\dagger + \sin\theta_{k-t_x/L_x}\zeta_{k-\pi}\Big)\,, \tag{3.63}$$

with

$$\tan(2\theta_k) = \frac{1}{\alpha \sin k}, \qquad \theta_k \in \left[0, \frac{\pi}{2}\right] . \tag{3.64}$$

Combining Eqs. (3.34) and (3.63), the transformation relating the $C_j$ and $\zeta_k$ fermions is

$$C_j = \sqrt{\frac{2}{L_x}} \mathrm{e}^{-\mathrm{i}\pi/4} \sum_{k \in \mathbb{K}_p} \mathrm{e}^{\mathrm{i}kj} \times \begin{cases} \cos\theta_{k+t_x/L_x} \zeta^\dagger_{-k} & \text{for } j \text{ odd} \\ \cos\theta_{k-t_x/L_x} \zeta_k & j \text{ even,} \end{cases} \tag{3.65}$$

with inverse

$$\zeta_k = \sqrt{\frac{2}{L_x}} \mathrm{e}^{\mathrm{i}\pi/4} \cos\theta_{k-t_x/L_x} \sum_{\text{even } j} \mathrm{e}^{-\mathrm{i}kj} C_j + \sqrt{\frac{2}{L_x}} \mathrm{e}^{-\mathrm{i}\pi/4} \sin\theta_{k-t_x/L_x} \sum_{\text{odd } j} \mathrm{e}^{-\mathrm{i}kj} C^\dagger_j \, . \tag{3.66}$$

This makes it clear that the annihilation operator $\zeta_k$ removes a fermion (or equivalently, removes a vertical dimer) on even sites or adds one on odd sites. According to Eq. (3.27), it therefore reduces $\Phi_y$ by one.

We now construct the spectrum of $\mathcal{H}$. As discussed in Sec. 3.3, one can find simultaneous eigenstates of $\mathcal{H}$ and $\Phi_y$. After substituting Eq. (3.65) into Eq. (3.27), the latter is given by

$$\Phi_y = -\frac{L_x}{2} + \sum_{k \in \mathbb{K}_p} \zeta^\dagger_k \zeta_k \tag{3.67}$$

in terms of $\zeta_k$ fermions, which counts the number of occupied states relative to half filling [the number of available $k$-states is $L_x$ by Eqs. (3.35) and (3.36)].[6]

The occupation-number states of the $\zeta_k$ fermions with $k \in \mathbb{K}_p$ form a complete set of mutual eigenstates of $\mathcal{H}_p$ and $\Phi_y$. From Eq. (3.50), the complete set of eigenstates of $\mathcal{H}$ is given by the union of all eigenstates of $\mathcal{H}_0$ that have even $\Phi_y$ eigenvalue and all eigenstates of $\mathcal{H}_1$ that have odd $\Phi_y$ eigenvalue. We will denote $|\Phi_y\rangle_n$ as the $n$th excited eigenstate with vertical flux $\Phi_y$, and $E_n(\Phi_y)$ as its eigenenergy. The spectrum of the two-row transfer matrix $W$ follows from that of $\mathcal{H}$ through Eq. (3.49): $|\Phi_y\rangle_n$ is also an eigenstate of $W$, but with eigenvalue $\mathrm{e}^{-2E_n(\Phi_y)}$.

[6] $\Phi_y$ does not contain $C_{L_x+1}$ and so does not depend on $p$; either $p$ gives the same result.

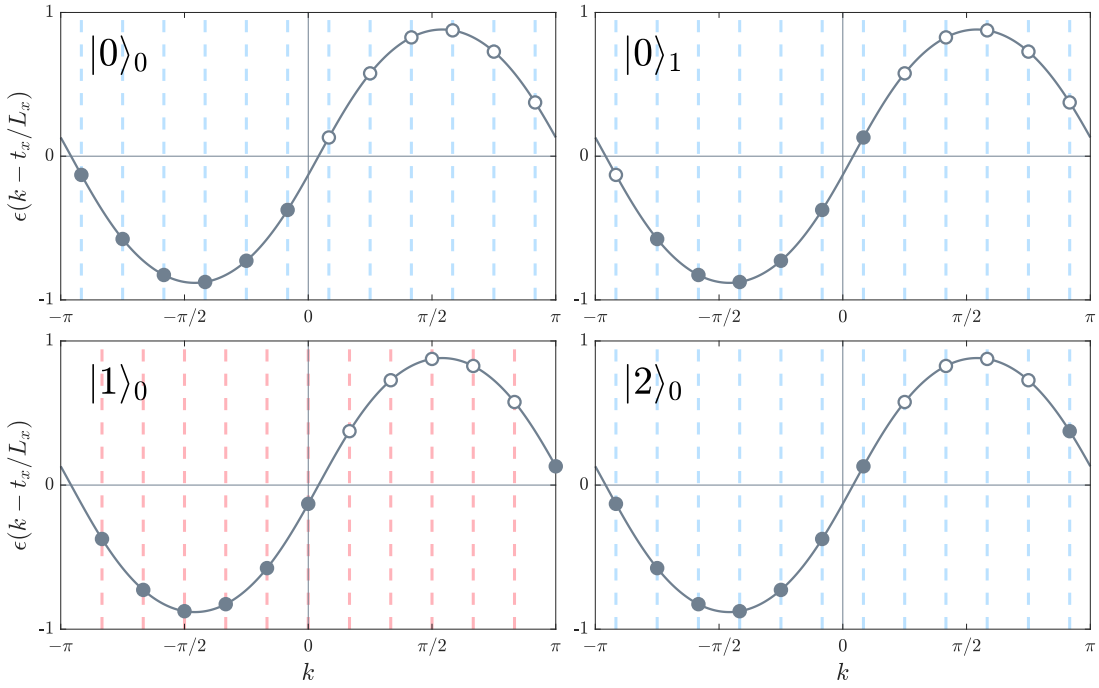


Figure 3.3: Simultaneous eigenstates of the Hamiltonian $\mathcal{H}$, given by Eqs. (3.50) and (3.60), and the vertical flux $\Phi_y$ of Eq. (3.67), for $L_x = 12$, $\alpha = 1$ and $t_x = \pi/2$: The $n$th excited eigenstate with vertical flux $\Phi_y$ is denoted by $|\Phi_y\rangle_n$, while filled and empty circles represent filled and empty $\zeta_k$ orbitals, respectively. Top-left panel: Ground state $|0\rangle_0$, where $k$-states, given by Eq. (3.35) for $\Phi_y$ even (dashed blue lines), are all occupied for $\epsilon(k - t_x/L_x) < 0$. Top-right panel: First excited state in the $\Phi_y = 0$ sector $|0\rangle_1$, obtained by adding a particle-hole excitation to $|0\rangle_0$. Bottom-left panel: Lowest-energy state in the $\Phi_y = 1$ sector $|1\rangle_0$, where $k$-states, given by Eq. (3.36) for $\Phi_y$ odd (dashed red lines), are occupied for $-\pi \leq k \leq 0$. Bottom-right panel: Lowest-energy state in the $\Phi_y = 2$ sector $|2\rangle_0$, obtained by adding two particles to $|0\rangle_0$.

As illustrated in Fig. 3.3 (top-left panel), the ground-state is half filled and thus denoted by $|0\rangle_0$. Formally, it is defined by

$$\begin{aligned} \zeta_k|0\rangle_0 &= 0 \qquad \text{for} \qquad 0 < k < \pi \\ \zeta_k^\dagger|0\rangle_0 &= 0 \qquad \text{for} \qquad -\pi < k < 0\,, \end{aligned} \tag{3.68}$$

where $k \in \mathbb{K}_0$, and has energy

$$E_0(0) = \sum_{\substack{k\in\mathbb{K}_0 \\ k<0}} \epsilon(k - t_x/L_x)\,. \tag{3.69}$$

Fig. 3.3 also illustrates some eigenstates with higher energy.

To calculate the ground-state energy $E_0(0)$, in the limit $L_x \to \infty$ and including $O(1/L_x)$ corrections, we rewrite the sum in Eq. (3.69) as an integral using the Euler–Maclaurin formula

$$\sum_{i=0}^{n} f(a+i\delta) = \frac{1}{\delta}\int_a^{a+n\delta} f(\phi)\,d\phi + \frac{1}{2}[f(a)+f(a+n\delta)] + \frac{\delta}{12}[f'(a+n\delta)-f'(a)] + O(\delta^3)\,, \quad (3.70)$$

with $a = -(L_x-1)\frac{\pi}{L_x}$, $\delta = \frac{2\pi}{L_x}$ and $n = \frac{L_x}{2} - 1$. The integral can be performed by extending the range of integration to $[-\pi, 0]$ and expanding $\epsilon(k - t_x/L_x)$ as a power series in $1/L_x$. The leading term is then

$$\frac{L_x}{2\pi}\int_{-\pi}^{0} dk\, \sinh^{-1}(\alpha \sin k) = \frac{\mathrm{i}L_x\chi_2(\mathrm{i}\alpha)}{\pi}\,, \quad (3.71)$$

where $\chi_2(z)$ is the Legendre chi function [in particular, $\chi_2(\mathrm{i}) = \mathrm{i}G$, where

$$G = \sum_{n=0}^{\infty} \frac{(-1)^n}{(2n+1)^2} \quad (3.72)$$

is Catalan's constant]. The $O(L_x^0)$ term vanishes, while the $O(1/L_x)$ term is $t_x^2\alpha/2\pi L_x$.

The correction terms

$$-\frac{1}{\delta}\left[\int_{-\pi}^{a} f(\phi)\,d\phi + \int_{a+n\delta}^{0} f(\phi)\,d\phi\right], \quad (3.73)$$

which arise when extending the integration bounds, as well as the remaining terms in Eq. (3.70), can be calculated using the Taylor expansion

$$\epsilon(k) \approx \alpha k + O(k^3), \qquad |k| \ll 1\,. \quad (3.74)$$

The final result is

$$E_0(0) = \frac{\mathrm{i}L_x\chi_2(\mathrm{i}\alpha)}{\pi} - \frac{\pi\alpha}{6L_x} + \frac{t_x^2\alpha}{2\pi L_x} + O\left(\frac{1}{L_x^3}\right), \quad (3.75)$$

and a similar calculation for the lowest-energy state in the $\Phi_y = 1$ sector gives

$$E_0(1) = E_0(0) + \frac{\pi\alpha}{2L_x} + O\left(\frac{1}{L_x^3}\right) . \tag{3.76}$$

## 3.5 Partition function

In this section, we write down the partition function $Z(\boldsymbol{t})$ using Eq. (3.14) and eigenvalues of the two-row transfer matrix, before taking the thermodynamic limit.

By Eqs. (3.30) and (3.51), one can split $Z(\boldsymbol{t})$ into contributions from each parity sector, giving

$$Z(\boldsymbol{t}) = \mathrm{Tr}\left(\sum_p \mathrm{e}^{\mathrm{i}t_y\Phi_y}\mathrm{e}^{-L_y\mathcal{H}_p}\Pi_p\right) . \tag{3.77}$$

The projector $\Pi_p$ can be expanded using Eqs. (3.28) and (3.67) as

$$\Pi_p = \frac{1}{2}\sum_{\sigma=\pm}\sigma^p \exp\left[-\mathrm{i}\pi\delta_{\sigma,-}\left(-\frac{L_x}{2} + \sum_{k\in\mathbb{K}_p}\zeta_k^\dagger\zeta_k\right)\right] , \tag{3.78}$$

and hence

$$\mathrm{e}^{\mathrm{i}t_y\Phi_y}\mathrm{e}^{-L_y\mathcal{H}_p}\Pi_p = \frac{1}{2}\sum_{\sigma=\pm}\sigma^p\mathrm{e}^{-L_y\tilde{\mathcal{H}}_{p,\sigma}} , \tag{3.79}$$

where

$$\tilde{\mathcal{H}}_{p,\sigma} = \frac{\mathrm{i}L_x}{2L_y}(t_y - \pi\delta_{\sigma,-}) + \sum_{k\in\mathbb{K}_p}\tilde{\epsilon}_\sigma(k)\zeta_k^\dagger\zeta_k , \tag{3.80}$$

with

$$\tilde{\epsilon}_\sigma(k) = \epsilon(k - t_x/L_x) - \frac{\mathrm{i}}{L_y}(t_y - \pi\delta_{\sigma,-}) . \tag{3.81}$$

The partition function, Eq. (3.77), can therefore be written as

$$Z(\boldsymbol{t}) = \frac{1}{2}\sum_{p,\sigma}\sigma^p Z_{p,\sigma} , \tag{3.82}$$

where $Z_{p,\sigma} = \mathrm{Tr}\,\mathrm{e}^{-L_y\tilde{\mathcal{H}}_{p,\sigma}}$. Because the trace of an operator is equivalent to the

sum of its eigenvalues, one has

$$Z_{p,\pm} = (\pm \mathrm{e}^{\mathrm{i}t_y})^{-L_x/2} \prod_{k \in \mathbb{K}_p} \left[1 \pm \mathrm{e}^{-L_y \epsilon(k - t_x/L_x)} \mathrm{e}^{\mathrm{i}t_y}\right] , \tag{3.83}$$

which reduces to Lieb's partition function for $\boldsymbol{t} = \boldsymbol{0}$ [see Ref. [23], Eq. (3.14)].

We now take the thermodynamic limit, retaining leading-order corrections to the free-energy density. To do so for $Z_{0,\pm}$, we factor out $\pm \mathrm{e}^{-L_y \epsilon(k - t_x/L_x)} \mathrm{e}^{\mathrm{i}t_y}$ for all terms in the product with $k < 0$ and restrict the product to $0 < k \leq \pi/2$, which gives

$$\begin{aligned} Z_{0,\pm} = \mathrm{e}^{-L_y E_0(0)} &\left\{ \prod_{n=1}^{\lceil L_x/4 \rceil} \left[1 \pm \mathrm{e}^{-L_y \epsilon(k - t_x/L_x)} \mathrm{e}^{\mathrm{i}t_y}\right] \left[1 \pm \mathrm{e}^{-L_y \epsilon(k + t_x/L_x)} \mathrm{e}^{-\mathrm{i}t_y}\right] \right\} \times \\ &\left\{ \prod_{n=1}^{\lfloor L_x/4 \rfloor} \left[1 \pm \mathrm{e}^{-L_y \epsilon(k - t_x/L_x)} \mathrm{e}^{-\mathrm{i}t_y}\right] \left[1 \pm \mathrm{e}^{-L_y \epsilon(k + t_x/L_x)} \mathrm{e}^{\mathrm{i}t_y}\right] \right\} , \end{aligned} \tag{3.84}$$

where $k = (2n-1)\frac{\pi}{L_x}$ by Eq. (3.35).

In the limit $L_x, L_y \to \infty$, we can replace $\epsilon(k \pm t_x/L_x)$ by its leading-order dependence $\alpha(k \pm t_x/L_x)$ [see Eq. (3.74)], since the next-order terms will eventually be of order $L_y/L_x^3$. Hence, Eq. (3.84) becomes

$$Z_{0,\pm} = \mathrm{e}^{-L_y E_0(0)} \prod_{n=1}^{\infty} (1 \pm y q^{n-1/2})(1 \pm y^{-1} q^{n-1/2})(1 \pm y^* q^{n-1/2})(1 \pm y^{*-1} q^{n-1/2}) , \tag{3.85}$$

where $y = \mathrm{e}^{\rho t_x} \mathrm{e}^{\mathrm{i}t_y}$, $q = \mathrm{e}^{-2\pi\rho}$ and $\rho = \alpha L_y / L_x$. This can be expressed in terms of Jacobi theta functions using the first equality of Eqs. (3.A.3) and (3.A.4):

$$Z_{0,+} = \mathrm{e}^{-L_y E_0(0)} q^{1/12} \frac{\theta_3(y|q)\theta_3(y^*|q)}{\eta^2(q)} , \tag{3.86}$$

where $\eta(q)$ is the Dedekind eta function defined in Eq. (3.A.5), and the same for $Z_{0,-}$ but with $\theta_3 \to \theta_4$. An analogous calculation for $Z_{1,\pm}$ yields

$$Z_{1,+} = \mathrm{e}^{-L_y E_0(1)} q^{-1/6} \frac{\theta_2(y|q)\theta_2(y^*|q)}{\eta^2(q)} , \tag{3.87}$$

with $\theta_2 \to \theta_1$ for $Z_{1,-}$.

Combining the results for $Z_{p,\sigma}$ with Eqs. (3.75) and (3.76), Eq. (3.82) becomes

$$Z(\boldsymbol{t}) = \exp\left[\frac{-\mathrm{i}L_xL_y\chi_2(\mathrm{i}\alpha)}{\pi}\right]\exp\left(-\frac{\rho t_x^2}{2\pi}\right)\frac{\sum_{i=1}^4\theta_i(y|q)\theta_i(y^*|q)}{2\eta^2(q)}\,, \tag{3.88}$$

which is consistent with Eq. (8.41) of Ref. [68] when $t_x = 0$. When $\boldsymbol{t} = \boldsymbol{0}$, $\theta_1(1|q) = 0$ and the partition function is

$$Z(\boldsymbol{0}) = \exp\left[\frac{-\mathrm{i}L_xL_y\chi_2(\mathrm{i}\alpha)}{\pi}\right]\frac{\sum_{i=2}^4\theta_i^2(1|q)}{2\eta^2(q)}\,, \tag{3.89}$$

in agreement with Ref. [27].

The first term in Eq. (3.89) grows exponentially with system volume, and represents the weight of dimer configurations in the bulk, i.e., it specifies the bulk free-energy density

$$f_{\mathrm{bulk}} = -\lim_{L_x,L_y\to\infty}\frac{1}{L_xL_y}\log Z(\boldsymbol{0}) \tag{3.90}$$

$$= \frac{\mathrm{i}\chi_2(\mathrm{i}\alpha)}{\pi}\,. \tag{3.91}$$

As one might expect, $f_{\mathrm{bulk}}$ does not depend on the choice of boundary conditions, although we note that this is not true in the case of the honeycomb lattice [78].

The remaining terms in $Z(\boldsymbol{0})$ are boundary dependent and, in the case of PBCs, encode information about topological flux sectors (see below). Previously, these terms have also been evaluated for closed [27] and cylindrical [79] boundaries, as well as embeddings on the Möbius strip and Klein bottle [80]. In general, one obtains terms in the free energy proportional to the edge of the system [e.g., $2(L_x + L_y)$ for closed boundaries] and of order $L_y/L_x$. However, with PBCs (i.e., a torus) the edge is zero and we only observe the latter.

## Flux sectors

We now show how the partition function, Eq. (3.89), divides into topological sectors labeled by the flux. By construction, $Z(\boldsymbol{t})$ is periodic in $t_\mu$ (with period

$2\pi$), so can be expressed as a Fourier series

$$Z(\boldsymbol{t}) = \sum_{\boldsymbol{\Phi}} \tilde{Z}_{\boldsymbol{\Phi}} \mathrm{e}^{\mathrm{i}\boldsymbol{t}\cdot\boldsymbol{\Phi}} \,. \tag{3.92}$$

Comparison of Eqs. (3.1) and (3.92) implies

$$\tilde{Z}_{\boldsymbol{\Phi}} = \sum_{c\in\mathfrak{C}_0(\boldsymbol{\Phi})} \alpha^{N_x} \,, \tag{3.93}$$

where the set $\mathfrak{C}_0(\boldsymbol{\Phi})$ contains all close-packed dimer configurations with flux $\boldsymbol{\Phi}$. In other words, the Fourier coefficient $\tilde{Z}_{\boldsymbol{\Phi}}$ can be interpreted as the partial partition function, or total weight, of flux sector $\boldsymbol{\Phi}$.

To calculate $\tilde{Z}_{\boldsymbol{\Phi}}$, we use the second equality of Eqs. (3.A.1)–(3.A.4) to rewrite Eq. (3.88) as [28]

$$Z(\boldsymbol{t}) = \mathrm{e}^{-L_x L_y f_{\mathrm{bulk}}} \frac{\sum_{m\in\mathbb{Z}} \mathrm{e}^{-\rho(t_x-2\pi m)^2/2\pi} \sum_{n\in\mathbb{Z}} \mathrm{e}^{\mathrm{i}nt_y} \mathrm{e}^{-\pi\rho n^2/2}}{\eta^2(q)} \tag{3.94}$$

(the periodicity in $t_x$ is now apparent). The sum over $m$ can be written in the same form as the sum over $n$ through the Poisson summation formula, giving

$$Z(\boldsymbol{t}) = \mathrm{e}^{-L_x L_y f_{\mathrm{bulk}}} \frac{\sum_{m\in\mathbb{Z}} \mathrm{e}^{\mathrm{i}mt_x} \mathrm{e}^{-\pi m^2/2\rho} \sum_{n\in\mathbb{Z}} \mathrm{e}^{\mathrm{i}nt_y} \mathrm{e}^{-\pi\rho n^2/2}}{\sqrt{2\rho}\eta^2(q)} \,, \tag{3.95}$$

which allows us to read off from Eqs. (3.92) and (3.95)

$$\tilde{Z}_{\boldsymbol{\Phi}} = \mathrm{e}^{-L_x L_y f_{\mathrm{bulk}}} \frac{\mathrm{e}^{-\pi(\Phi_x^2/\rho+\rho\Phi_y^2)/2}}{\sqrt{2\rho}\eta^2(q)} \,. \tag{3.96}$$

This result has previously been obtained for the honeycomb-lattice dimer model using Pfaffian methods [28], while Ref. [68] has used the transfer matrix to calculate the partial partition function of flux sector $\Phi_y$, equivalent to $\sum_{\Phi_x} \tilde{Z}_{\boldsymbol{\Phi}}$ [see their Eqs. (8.19) and (8.36)].

Knowledge of $\tilde{Z}_{\boldsymbol{\Phi}}$ can be used to calculate flux moments. The probability of

flux $\mathbf{\Phi}$ is given by

$$P(\mathbf{\Phi}) = \frac{\tilde{Z}_{\mathbf{\Phi}}}{\sum_{\mathbf{\Phi}} \tilde{Z}_{\mathbf{\Phi}}} \tag{3.97}$$

$$= \frac{\mathrm{e}^{-\pi(\Phi_x^2/\rho + \rho\Phi_y^2)/2}}{\sum_{m,n\in\mathbb{Z}} \mathrm{e}^{-\pi(m^2/\rho+\rho n^2)/2}}\,, \tag{3.98}$$

which implies that $\Phi_x$ and $\Phi_y$ are independent variables. This form is known from effective field theories (see Appendix 2.A.1) [7, 10]. The mean flux vanishes by symmetry, while the mean-square flux is given by

$$\langle \Phi_x^2 \rangle = \frac{\sum_{n\in\mathbb{Z}} n^2 \mathrm{e}^{-\pi n^2/2\rho}}{\sum_{n\in\mathbb{Z}} \mathrm{e}^{-\pi n^2/2\rho}}\,, \tag{3.99}$$

and the same for $\Phi_y$ but with $\rho \to 1/\rho$.

## 3.6 Expectation values

In this section, we compute various expectation values in the thermodynamic limit, using the spectrum of the two-row transfer matrix.

We use Eq. (3.15), and restrict to operators $O$ that conserve parity of $\Phi_y$, i.e., $[O, (-1)^{\Phi_y}] = 0$. From Eq. (3.27), this includes any product of an even number of $C_j$ fermions, and hence any operator constructed from $d_{j,x}$ and $d_{j,y}$ [see Eqs. (3.24) and (3.25)]. It also allows us to calculate the monomer distribution function, as we show in Sec. 3.6.4. With this restriction, and because $(-1)^{\Phi_y}$ commutes with any quadratic form in fermions, $O(l) = U(l)^{-1} O U(l)$ can be written as

$$O(l) = O(l) \sum_p \Pi_p \tag{3.100}$$

$$= \sum_p O(l)_p \Pi_p\,, \tag{3.101}$$

where

$$O(l)_p = U_p(l)^{-1} O_p U_p(l)\,, \tag{3.102}$$

and $U_p(l)$ is given by Eq. (3.16) but with $V$ replaced by $V_p$.

As for the partition function, the trace in Eq. (3.15) can be split into parity

sectors by inserting Eqs. (3.30), (3.51) and (3.101), which yields

$$\langle O'(l')O(l)\rangle = \frac{1}{Z(\boldsymbol{t})}\sum_p \mathrm{Tr}\left[\mathrm{e}^{\mathrm{i}t_y\Phi_y}\mathrm{e}^{-L_y\mathcal{H}_p}\Pi_p O'(l')_p O(l)_p\right] , \tag{3.103}$$

where we have used $[V_p, \Pi_p] = 0$ and assumed $[O_p, \Pi_p] = 0$ (it is always possible to choose $O_p$ in this way). By Eq. (3.79), this can be rewritten as

$$\langle O'(l')O(l)\rangle = \frac{\sum_{p,\sigma}\sigma^p Z_{p,\sigma}\langle O'(l')O(l)\rangle_{p,\sigma}}{\sum_{p,\sigma}\sigma^p Z_{p,\sigma}} , \tag{3.104}$$

where, assuming $Z_{p,\sigma} \neq 0$,

$$\langle O'(l')O(l)\rangle_{p,\sigma} = \frac{1}{Z_{p,\sigma}}\,\mathrm{Tr}\left[\mathrm{e}^{-L_y\tilde{\mathcal{H}}_{p,\sigma}}O'(l')_p O(l)_p\right] . \tag{3.105}$$

Expectation values are therefore given by an average over the four $(p,\sigma)$ sectors, each weighted by $Z_{p,\sigma}$.

### 3.6.1 Two-point correlation functions of $C_j$ fermions

For an operator $O$ given by a product of $C_j$ fermions, the corresponding time-evolved operator $O(l)_p$ can also be expressed as a product of $C_j(l)_p$, with the same $p$ for each. For example, when $O = d_{j,y}$ one has

$$\begin{aligned} d_{j,y}(l)_p &= U_p(l)^{-1}C_j^\dagger C_j U_p(l) && (3.106)\\ &= U_p(l)^{-1}C_j^\dagger U_p(l)U_p(l)^{-1}C_j U_p(l) && (3.107)\\ &= C_j^\dagger(l)_p C_j(l)_p\,. && (3.108)\end{aligned}$$

Here, $C_j(l)_p$ is defined by extending Eq. (3.102) to $C_j$, even though it does not conserve parity and so does not obey Eq. (3.101).

An expectation value $\langle O'(l')O(l)\rangle_{p,\sigma}$ can then be expressed in terms of a product of an even number of $C_j(l)$ operators. Because this is a time-ordered product and $\tilde{\mathcal{H}}_{p,\sigma}$ is a free-fermion Hamiltonian, Wick's theorem [81] applies, which allows us to write $\langle O'(l')O(l)\rangle_{p,\sigma}$ as a sum over products of two-point $C_j(l)$ correlators in each $(p,\sigma)$ sector. [We similarly extend the definition Eq. (3.105) to include $O = C_j$, even though Eq. (3.104) is not valid in this case.] We calculate these

two-point correlators in this section.

To do so, we first use Eqs. (3.16) and (3.102) to derive an expression for $C_j(l)_p$ in terms of $\zeta_k$ fermions. For $l$ even, Eq. (3.60) implies

$$W_p^{-1}\zeta_k W_p = \mathrm{e}^{-2\epsilon(k-t_x/L_x)}\zeta_k\,, \tag{3.109}$$

which can be used in Eq. (3.65) to give

$$C_j(l)_p = \sqrt{\frac{2}{L_x}}\mathrm{e}^{-\mathrm{i}\pi/4}\sum_{k\in\mathbb{K}_p}\mathrm{e}^{\mathrm{i}kj}\times\begin{cases}\cos\theta_{k+t_x/L_x}\mathrm{e}^{-l\epsilon(k+t_x/L_x)}\zeta_{-k}^\dagger & \text{for } j \text{ odd}\\ \cos\theta_{k-t_x/L_x}\mathrm{e}^{-l\epsilon(k-t_x/L_x)}\zeta_k & j \text{ even.}\end{cases} \tag{3.110}$$

For $l$ odd, as well as Eq. (3.109) we additionally require the results

$$\begin{aligned}(V_p^\dagger)^{-1}\zeta_k^* V_p^\dagger &= -\mathrm{e}^{-\epsilon(k-t_x/L_x)}\zeta_{k-\pi}^\dagger\\ (V_p^\dagger)^{-1}\big(\zeta_k^\dagger\big)^* V_p^\dagger &= -\mathrm{e}^{\epsilon(k-t_x/L_x)}\zeta_{k-\pi}\,,\end{aligned} \tag{3.111}$$

which can be derived from Eq. (3.33). This time we use these in the complex conjugate of Eq. (3.65), to find

$$C_j(l)_p = \sqrt{\frac{2}{L_x}}\mathrm{e}^{\mathrm{i}\pi/4}\sum_{k\in\mathbb{K}_p}\mathrm{e}^{\mathrm{i}kj}\times\begin{cases}\cos\theta_{k-t_x/L_x}\mathrm{e}^{-l\epsilon(k-t_x/L_x)}\zeta_k & \text{for } j \text{ odd}\\ -\cos\theta_{k+t_x/L_x}\mathrm{e}^{-l\epsilon(k+t_x/L_x)}\zeta_{-k}^\dagger & j \text{ even.}\end{cases} \tag{3.112}$$

Finally, by combining Eqs. (3.110) and (3.112), we have

$$C_j(l)_p = \sqrt{\frac{2}{L_x}}\mathrm{e}^{-\mathrm{i}(-1)^l\pi/4}\sum_{k\in\mathbb{K}_p}\mathrm{e}^{\mathrm{i}kj}\times \begin{cases}(-1)^l\cos\theta_{k+t_x/L_x}\mathrm{e}^{-l\epsilon(k+t_x/L_x)}\zeta_{-k}^\dagger & \text{for } j+l \text{ odd}\\ \cos\theta_{k-t_x/L_x}\mathrm{e}^{-l\epsilon(k-t_x/L_x)}\zeta_k & j+l \text{ even,}\end{cases} \tag{3.113}$$

for all $l$.

Since $\tilde{\mathcal{H}}_{p,\sigma}$, defined in Eq. (3.80), is a free-fermion Hamiltonian with dispersion $\tilde{\epsilon}_\sigma$, and Eq. (3.105) describes a thermal distribution with effective temperature

$1/L_y$, the two-point correlation functions of the $\zeta_k$ fermions are given by

$$\begin{aligned}
\langle \zeta_k \zeta_{k'} \rangle_{p,\sigma} &= \langle \zeta_k^\dagger \zeta_{k'}^\dagger \rangle = 0 \\
\langle \zeta_k^\dagger \zeta_{k'} \rangle_{p,\sigma} &= \delta_{kk'} n_{\mathrm{F}}\big(L_y \tilde{\epsilon}_\sigma(k)\big) \\
\langle \zeta_k \zeta_{k'}^\dagger \rangle_{p,\sigma} &= \delta_{kk'} n_{\mathrm{F}}\big(-L_y \tilde{\epsilon}_\sigma(k)\big)\,,
\end{aligned} \tag{3.114}$$

where $n_{\mathrm{F}}(z) = (\mathrm{e}^z + 1)^{-1}$ is the Fermi–Dirac distribution function.

Hence, denoting $\boldsymbol{R} = (X, Y)$, the $C_j(l)$ correlators are

$$\langle C_{j+X}(l+Y) C_j(l) \rangle_{p,\sigma} = \begin{cases} -\mathrm{e}^{\mathrm{i}\varphi(l,Y)} \Gamma_{p,\sigma}(\boldsymbol{R}, -\boldsymbol{t}) & \text{for } X+Y \text{ odd},\ j+l \text{ odd} \\ -\mathrm{e}^{-\mathrm{i}\varphi(l,Y)} \Gamma_{p,\sigma}(\boldsymbol{R}, \boldsymbol{t}) & X+Y \text{ odd},\ j+l \text{ even} \\ 0 & X+Y \text{ even} \end{cases} \tag{3.115}$$

$$\langle C_{j+X}^\dagger(l+Y) C_j^\dagger(l) \rangle_{p,\sigma} = \begin{cases} \mathrm{e}^{-\mathrm{i}\varphi(l,Y)} \Gamma_{p,\sigma}(\boldsymbol{R}, \boldsymbol{t}) & \text{for } X+Y \text{ odd},\ j+l \text{ odd} \\ \mathrm{e}^{\mathrm{i}\varphi(l,Y)} \Gamma_{p,\sigma}(\boldsymbol{R}, -\boldsymbol{t}) & X+Y \text{ odd},\ j+l \text{ even} \\ 0 & X+Y \text{ even} \end{cases} \tag{3.116}$$

$$\langle C_{j+X}^\dagger(l+Y) C_j(l) \rangle_{p,\sigma} = \begin{cases} 0 & \text{for } X+Y \text{ odd} \\ \mathrm{e}^{\mathrm{i}\varphi(l,Y)} \left[\Delta_{p,\sigma}(\boldsymbol{R}, -\boldsymbol{t}) - \Gamma_{p,\sigma}(\boldsymbol{R}, -\boldsymbol{t})\right] & X+Y \text{ even},\ j+l \text{ odd}, \\ \mathrm{e}^{-\mathrm{i}\varphi(l,Y)} \left[\Delta_{p,\sigma}(\boldsymbol{R}, \boldsymbol{t}) - \Gamma_{p,\sigma}(\boldsymbol{R}, \boldsymbol{t})\right] & X+Y \text{ even},\ j+l \text{ even} \end{cases} \tag{3.117}$$

$$\langle C_{j+X}(l+Y) C_j^\dagger(l) \rangle_{p,\sigma} = \begin{cases} 0 & \text{for } X+Y \text{ odd} \\ \mathrm{e}^{-\mathrm{i}\varphi(l,Y)} \left[\Delta_{p,\sigma}(\boldsymbol{R}, \boldsymbol{t}) + \Gamma_{p,\sigma}(\boldsymbol{R}, \boldsymbol{t})\right] & X+Y \text{ even},\ j+l \text{ odd}, \\ \mathrm{e}^{\mathrm{i}\varphi(l,Y)} \left[\Delta_{p,\sigma}(\boldsymbol{R}, -\boldsymbol{t}) + \Gamma_{p,\sigma}(\boldsymbol{R}, -\boldsymbol{t})\right] & X+Y \text{ even},\ j+l \text{ even} \end{cases} \tag{3.118}$$

where

$$\varphi(l,Y) = \begin{cases} (-1)^l \frac{\pi}{2} & \text{for } Y \text{ odd} \\ 0 & Y \text{ even,} \end{cases} \tag{3.119}$$

and

$$\Gamma_{p,\sigma}(\boldsymbol{R},\boldsymbol{t}) = \frac{1}{L_x} \sum_{k\in\mathbb{K}_p} \mathrm{e}^{-\mathrm{i}kX} \mathrm{e}^{Y\epsilon(k-t_x/L_x)} n_{\mathrm{F}}\big(L_y\tilde{\epsilon}_\sigma(k)\big) \times \begin{cases} \mathrm{i}\sin(2\theta_{k-t_x/L_x}) & \text{for } X+Y \text{ odd} \\ -\cos(2\theta_{k-t_x/L_x}) & X+Y \text{ even} \end{cases} \tag{3.120}$$

$$\Delta_{p,\sigma}(\boldsymbol{R},\boldsymbol{t}) = \frac{1}{L_x} \sum_{k\in\mathbb{K}_p} \mathrm{e}^{-\mathrm{i}kX} \mathrm{e}^{Y\epsilon(k-t_x/L_x)} n_{\mathrm{F}}\big(L_y\tilde{\epsilon}_\sigma(k)\big)\,. \tag{3.121}$$

These results are exact, with the correct (anti)periodicity in the horizontal direction, and could be used to calculate expectation values for finite system sizes as a function of flux sector.

Instead, we take the thermodynamic limit $L_x, L_y \to \infty$, keeping the ratio $L_y/L_x$ and the separation $|\boldsymbol{R}|$ finite. In this limit, $n_{\mathrm{F}}(z)$ can be replaced by a step function $\vartheta(-\operatorname{Re} z)$ and the discrete $k$ values become continuous, giving

$$\Gamma_{p,\sigma}(\boldsymbol{R},\boldsymbol{t}) \approx \Gamma(\boldsymbol{R}) = \int_0^\pi \frac{dk}{2\pi}\, \mathrm{e}^{\mathrm{i}kX} \mathrm{e}^{-Y\epsilon(k)} \times \begin{cases} \mathrm{i}\sin(2\theta_k) & \text{for } X+Y \text{ odd} \\ \cos(2\theta_k) & X+Y \text{ even} \end{cases} \tag{3.122}$$

$$\Delta_{p,\sigma}(\boldsymbol{R},\boldsymbol{t}) \approx \Delta(\boldsymbol{R}) = \int_0^\pi \frac{dk}{2\pi}\, \mathrm{e}^{\mathrm{i}kX} \mathrm{e}^{-Y\epsilon(k)}\,. \tag{3.123}$$

Some values of these integrals for small $|\boldsymbol{R}|$ are shown in Table 3.1, expressed in terms of the quantities

$$\rho_x = \frac{\arctan\alpha}{\pi} \qquad \rho_y = \frac{\arctan\left(1/\alpha\right)}{\pi}\,, \tag{3.124}$$

which satisfy $\rho_x + \rho_y = \frac{1}{2}$. For large $|\boldsymbol{R}|$, the asymptotic behavior is obtained by integrating by parts repeatedly, treating the cases $Y \gg 1$ [where Eq. (3.74) can be used] and $Y$ of order unity separately.

These expressions are independent of $p$ and $\sigma$, i.e., all four $(p,\sigma)$ sectors make

| Integral | Value |
|---|---|
| $\Gamma(\mathbf{0})$ | $\rho_x$ |
| $\Gamma(1,0)$ | $-\dfrac{\rho_x}{\alpha}$ |
| $\Gamma(0,1)$ | $\mathrm{i}\rho_y$ |
| $\Gamma(2,0)$ | $-\dfrac{1}{\pi\alpha}+\dfrac{\rho_x}{\alpha^2}$ |
| $\Gamma(1,2)$ | $-\dfrac{1}{\pi}+\alpha\rho_y$ |
| $\Gamma(2,1)$ | $-\dfrac{\mathrm{i}}{\alpha^2}\left(\rho_x-\dfrac{\alpha}{\pi}\right)$ |
| $\Gamma(3,0)$ | $-\rho_x\left(\dfrac{1}{\alpha}+\dfrac{2}{\alpha^3}\right)+\dfrac{2}{\pi\alpha^2}$ |
| $\Gamma(0,3)$ | $\mathrm{i}\left[\rho_y(1+2\alpha^2)-\dfrac{2\alpha}{\pi}\right]$ |
| $\Gamma(\lvert\boldsymbol{R}\rvert\gg 1)$, $X$ odd, $Y$ even | $-\dfrac{1}{\pi}\dfrac{X}{X^2+(\alpha Y)^2}$ |
| $\Gamma(\lvert\boldsymbol{R}\rvert\gg 1)$, $X$ even, $Y$ odd | $\dfrac{\mathrm{i}}{\pi}\dfrac{\alpha Y}{X^2+(\alpha Y)^2}$ |
| $\Gamma(\lvert\boldsymbol{R}\rvert\gg 1)$, $X$ odd, $Y$ odd | $\dfrac{2\mathrm{i}\alpha}{\pi}\dfrac{X\alpha Y}{[X^2+(\alpha Y)^2]^2}$ |
| $\Gamma(\lvert\boldsymbol{R}\rvert\gg 1)$, $X$ even, $Y$ even | $-\dfrac{\alpha}{\pi}\dfrac{X^2-(\alpha Y)^2}{[X^2+(\alpha Y)^2]^2}$ |
| $\Delta(X\text{even},0)$ | $\frac{1}{2}\delta_{X,0}$ |
| $\Delta(\lvert\boldsymbol{R}\rvert\gg 1)$, $X$ odd | $\dfrac{\mathrm{i}}{\pi}\dfrac{X}{X^2+(\alpha Y)^2}$ |
| $\Delta(\lvert\boldsymbol{R}\rvert\gg 1)$, $X$ even | $\dfrac{1}{\pi}\dfrac{\alpha Y}{X^2+(\alpha Y)^2}$ |

Table 3.1: Values of the integrals $\Gamma(\boldsymbol{R})$ and $\Delta(\boldsymbol{R})$, defined in Eqs. (3.122) and (3.123), respectively, for small $|\boldsymbol{R}|$, as well as their asymptotic behavior for $|\boldsymbol{R}|\gg 1$. Values for $X<0$ may be obtained using the relation $\Gamma(-X,Y)=(-1)^X\Gamma(\boldsymbol{R})$ and the same for $\Delta(\boldsymbol{R})$.

equal contributions in the thermodynamic limit. Hence, Eq. (3.104) is redundant to this order, and we simply have $\langle O'(l')O(l)\rangle = \langle O'(l')O(l)\rangle_{0,+}$ for operators $O$ that are products of an even number of $C_j$ fermions. We therefore drop the $(p,\sigma)$ indices from now on.

Furthermore, they are independent of $\boldsymbol{t}$, whose leading-order dependence is $O(L_x^{-1}, L_y^{-1})$. This implies that expectation values are the same in any fixed flux sector in the thermodynamic limit (but note that that we have taken $L_x, L_y \to \infty$, so this does not apply for $\boldsymbol{\Phi} \sim L_x, L_y$). To see this we rewrite Eq. (3.2) as a sum over Fourier modes [cf. Eqs. (3.92) and (3.93)]

$$\langle O\rangle = \frac{1}{Z(\boldsymbol{t})}\sum_{\boldsymbol{\Phi}}\langle O\rangle_{\boldsymbol{\Phi}}\tilde{Z}_{\boldsymbol{\Phi}}\mathrm{e}^{\mathrm{i}\boldsymbol{t}\cdot\boldsymbol{\Phi}}\,, \tag{3.125}$$

where

$$\langle O\rangle_{\boldsymbol{\Phi}} = \frac{1}{\tilde{Z}_{\boldsymbol{\Phi}}}\sum_{c\in\mathfrak{C}_0(\boldsymbol{\Phi})} O\alpha^{N_x} \tag{3.126}$$

is the expectation value of the observable $O$ in a fixed flux sector $\boldsymbol{\Phi}$. After multiplying both sides of Eq. (3.125) by $Z(\boldsymbol{t})\mathrm{e}^{-\mathrm{i}\boldsymbol{t}\cdot\boldsymbol{\Phi}'}$ and integrating over $\boldsymbol{t}$, one finds that $\langle O\rangle_{\boldsymbol{\Phi}} = \langle O\rangle$ when the latter is independent of $\boldsymbol{t}$.

In subsequent sections we use Eqs. (3.115)–(3.118) to calculate various observables in the dimer model in the thermodynamic limit. We expect our results to reproduce those of Ref. [29] in this limit, since the choice of boundary conditions (PBCs versus closed) becomes irrelevant. We also note that asymptotic behavior of correlation functions can be predicted using effective field theories, although the results depend on phenomenological parameters known as the stiffnesses (we will demonstrate this in Chapter 4) [7].

### 3.6.2 Dimer occupation numbers

We first calculate the probability that a vertical or horizontal bond is occupied by a dimer, given by $\langle d_{j,y}(l)\rangle$ and $\langle d_{j,x}(l)\rangle$, respectively. (In the thermodynamic limit, there is no $\boldsymbol{t}$ dependence, and so $d^*_{j,x} = d_{j,x}$.)

Using Eqs. (3.24) and (3.25), one finds

$$\langle d_{j,x}(l)\rangle = -\alpha\Gamma(1,0) \tag{3.127}$$

$$= \rho_x\,, \tag{3.128}$$

and

$$\langle d_{j,y}(l)\rangle = \Delta(\mathbf{0}) - \Gamma(\mathbf{0}) \tag{3.129}$$

$$= \rho_y\,, \tag{3.130}$$

consistent with Sec. 5 of Ref. [29]. As required, each lattice site is touched by a dimer with probability unity, since $\langle d_{j,x}(l)\rangle + \langle d_{j,y}(l)\rangle = \frac{1}{2}$. In the isotropic case, $\alpha = 1$, one has $\langle d_{j,x}(l)\rangle = \langle d_{j,y}(l)\rangle = \frac{1}{4}$, whereas in the limit $\alpha \to 0$ ($\alpha \to \infty$) only vertical (horizontal) bonds are occupied.

### 3.6.3 Dimer–dimer correlation functions

Due to the close-packing constraint, the occupation of a given bond by a dimer is influenced by dimers far away. Hence, dimer–dimer correlations are non-trivial even in the absence of interactions. In this section, we show how they can be calculated by extending the above discussion to two-point correlators of $d_{j,x}$ and $d_{j,y}$.

The connected correlation function of two horizontal dimers with separation $\boldsymbol{R}$, illustrated in Fig. 3.4 (top), is given by (we assume $Y > 0$ throughout this section)

$$G^{xx}(\boldsymbol{R}) = \langle d_{j+X,x}(l+Y)d_{j,x}(l)\rangle - \langle d_{j+X,x}(l+Y)\rangle\langle d_{j,x}(l)\rangle, \qquad \boldsymbol{R} \neq \mathbf{0} \tag{3.131}$$

[for $\boldsymbol{R} = \mathbf{0}$ the first term vanishes due to $C_j^2(l) = 0$; see Footnote 3]. Inserting Eq. (3.24) and using Wick's theorem [81] yields

$$\frac{G^{xx}(\boldsymbol{R})}{\alpha^2} = \langle C_{j+X+1}(l+Y)C_j(l)\rangle\langle C_{j+X}(l+Y)C_{j+1}(l)\rangle - \langle C_{j+X+1}(l+Y)C_{j+1}(l)\rangle\langle C_{j+X}(l+Y)C_j(l)\rangle\,, \tag{3.132}$$

hence, by Eq. (3.115),

$$\frac{G^{xx}(\boldsymbol{R})}{\alpha^2} = \begin{cases} -\Gamma(\boldsymbol{R})^2 & \text{for } X+Y \text{ odd} \\ \Gamma(X-1,Y)\Gamma(X+1,Y) & X+Y \text{ even.} \end{cases} \tag{3.133}$$

From Table 3.1, some values for small $|\boldsymbol{R}|$ are

$$G^{xx}(1,0) = -\rho_x^2 \tag{3.134}$$

$$G^{xx}(0,1) = \alpha^2\rho_y^2 \tag{3.135}$$

$$G^{xx}(1,1) = \rho_y\left(\rho_x - \frac{\alpha}{\pi}\right) \tag{3.136}$$

$$G^{xx}(2,1) = \left(\frac{\rho_x}{\alpha} - \frac{1}{\pi}\right)^2 \tag{3.137}$$

$$G^{xx}(0,2) = -\left(\frac{\alpha}{\pi} - \alpha^2\rho_y\right)^2 \tag{3.138}$$

$$G^{xx}(0,3) = \alpha^2\left[\rho_y(1+2\alpha^2) - \frac{2\alpha}{\pi}\right]^2, \tag{3.139}$$

while the asymptotic behavior for $|\boldsymbol{R}| \gg 1$ is algebraic, rather than exponential:

$$\frac{G^{xx}(\boldsymbol{R})}{\alpha^2} \approx (-1)^X \frac{1}{\pi^2[X^2+(\alpha Y)^2]^2} \times \begin{cases} X^2 & \text{for } X \text{ odd, } Y \text{ even} \\ (\alpha Y)^2 & X \text{ even, } Y \text{ odd} \\ (\alpha Y)^2 & X \text{ odd, } Y \text{ odd} \\ X^2-1 & X \text{ even, } Y \text{ even.} \end{cases} \tag{3.140}$$

Similarly, the connected correlation function of two vertical dimers with separation $\boldsymbol{R}$, illustrated in Fig. 3.4 (bottom left), is

$$G^{yy}(\boldsymbol{R}) = \langle d_{j+X,y}(l+Y)d_{j,y}(l)\rangle - \langle d_{j+X,y}(l+Y)\rangle\langle d_{j,y}(l)\rangle\,. \tag{3.141}$$

Following the same procedure as for $G^{xx}(\boldsymbol{R})$, but now using Eqs. (3.25) and (3.115)–(3.118), yields

$$G^{yy}(\boldsymbol{R}) = \begin{cases} \Gamma(\boldsymbol{R})^2 & \text{for } X+Y \text{ odd} \\ \Delta(\boldsymbol{R})^2 - \Gamma(\boldsymbol{R})^2 & X+Y \text{ even.} \end{cases} \tag{3.142}$$

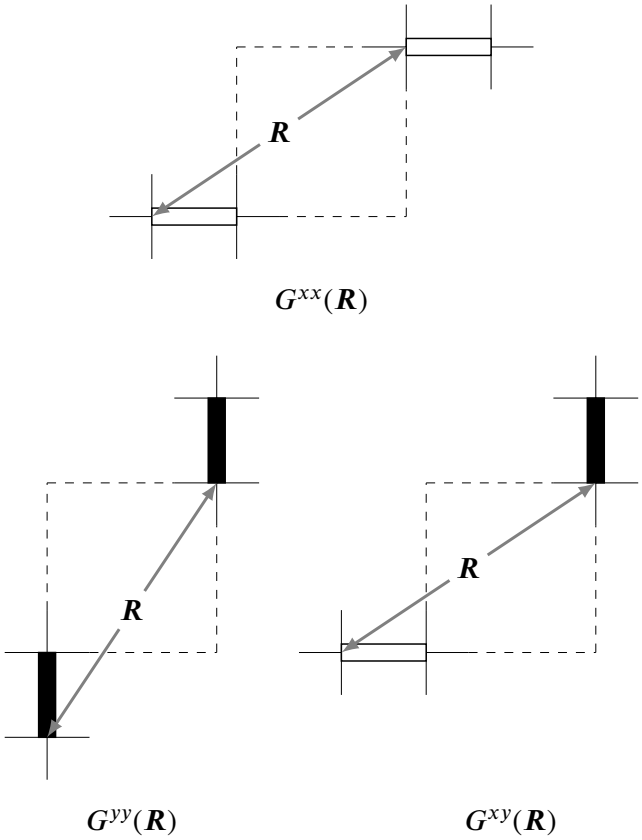


Figure 3.4: Dimer–dimer correlation function between two horizontal dimers (top), two vertical dimers (bottom left), and a horizontal and vertical dimer (bottom right). In each case, the disconnected part of the correlator [i.e., the first term in Eqs. (3.131), (3.141) and (3.143)] is equal to the probability that the two bonds with separation $\boldsymbol{R}$ are both occupied.

Note that, showing the $\alpha$ dependence of the correlators explicitly, one must have $G^{yy}(\boldsymbol{R};\alpha) = G^{xx}(Y,X;\alpha^{-1})$, which follows from Eq. (3.2) and $\alpha^{N_x} \propto \alpha^{-N_y}$ (the number of dimers is conserved).

The third possibility is the connected correlation function of a horizontal and vertical dimer with separation $\boldsymbol{R}$, illustrated in Fig. 3.4 (bottom right), which is

$$G^{xy}(\boldsymbol{R}) = \langle d_{j+X,y}(l+Y) d_{j,x}(l)\rangle - \langle d_{j+X,y}(l+Y)\rangle\langle d_{j,x}(l)\rangle\,. \tag{3.143}$$

The result is

$$\frac{G^{xy}(\boldsymbol{R})}{\alpha} = \begin{cases} \Gamma(\boldsymbol{R})[\Delta(X-1,Y) - \Gamma(X-1,Y)] & \text{for } X+Y \text{ odd} \\ \Gamma(X-1,Y)[\Gamma(\boldsymbol{R}) - \Delta(\boldsymbol{R})] & X+Y \text{ even,} \end{cases} \tag{3.144}$$

with asymptotic behavior

$$\frac{G^{xy}(\boldsymbol{R})}{\alpha} \approx (-1)^{X+Y} \frac{1}{\pi^2[X^2+(\alpha Y)^2]^2} \times \begin{cases} X\alpha(Y+1) & \text{for } X \text{ odd, } Y \text{ even} \\ (X-1)\alpha Y & X \text{ even, } Y \text{ odd} \\ X\alpha Y & X \text{ odd, } Y \text{ odd} \\ (X-1)\alpha(Y+1) & X \text{ even, } Y \text{ even.} \end{cases} \tag{3.145}$$

The results in this section are in agreement with Sec. 7 of Ref. [29].

### 3.6.4 Monomer distribution function

Finally, we characterize the (entropic) interaction between a pair of inserted test monomers by calculating the monomer distribution function

$$G_{\mathrm{m}}(\boldsymbol{R}) = \frac{1}{Z(\boldsymbol{t})} \sum_{c \in \mathfrak{C}(\boldsymbol{r}_+, \boldsymbol{r}_-)} \alpha^{N_x} \,, \tag{3.146}$$

where the set $\mathfrak{C}(\boldsymbol{r}_+, \boldsymbol{r}_-)$ contains all configurations with monomers at sites $\boldsymbol{r}_\pm$. For simplicity, we consider the case of two monomers on the same row.

Because $\sigma_j^-$ inserts a monomer on site $j$, in the transfer-matrix formalism one has

$$G_{\mathrm{m}}(X,0) = \langle \sigma_j^-(l) \sigma_{j+X}^-(l) \rangle \,, \tag{3.147}$$

which becomes

$$G_{\mathrm{m}}(X,0) = -\left\langle C_j \left[ \prod_{i=j+1}^{j+X-1} (1 - 2C_i^\dagger C_i) \right] C_{j+X} \right\rangle \tag{3.148}$$

after performing the Jordan–Wigner transformation, Eqs. (3.19)–(3.21) (from here on we do not explicitly show dependence on the row $l$).[7]

[7] In the case of two monomers on different rows, the operator on each row has an odd number of $C_j$ operators and so does not commute with $(-1)^{\Phi_y}$. We therefore cannot use Eq. (3.104); instead, we require the case where $O$ anticommutes with $(-1)^{\Phi_y}$.

Following Refs. [67, 73, 74], we now define operators

$$A_j = C_j^\dagger + C_j \tag{3.149}$$

$$B_j = C_j^\dagger - C_j \tag{3.150}$$

(note that $1 - 2C_j^\dagger C_j = A_j B_j$), which, by Eqs. (3.115)–(3.118), satisfy

$$\langle A_j A_{j+X} \rangle = \delta_{X,0} \tag{3.151}$$

$$\langle B_j B_{j+X} \rangle = -\delta_{X,0} \tag{3.152}$$

$$\langle B_j A_{j+X} \rangle = -\langle A_{j+X} B_j \rangle = -2\Gamma(X,0)\,. \tag{3.153}$$

In terms of these, Eq. (3.148) is a sum of four $2X$-point correlators, each of which can be expressed as a sum of products of two-point correlators through Wick's theorem [81]. Then, by Eqs. (3.151) and (3.152), the two correlators containing an unequal number of $A_j$ and $B_j$ vanish, while the remaining two are

$$\mathcal{W}(B,A) = \frac{1}{4}\left\langle \prod_{i=j}^{j+X-1} B_i A_{i+1} \right\rangle \tag{3.154}$$

$$= \frac{1}{4}\sum_{\sigma\in S_X} \operatorname{sgn}(\sigma) \prod_{i=1}^{X} \langle B_{j+i-1} A_{j+\sigma_i} \rangle\,, \tag{3.155}$$

where $S_X$ denotes the symmetric group of order $X$, and $(-1)^{X-1}\mathcal{W}(A,B)$. Inserting Eq. (3.153) and using the relation $\Gamma(-X,0) = (-1)^X \Gamma(X,0)$ with $\prod_{i=1}^{X}(-1)^{i-\sigma_i} = 1$, it follows that $\mathcal{W}(A,B) = \mathcal{W}(B,A)$, and hence

$$G_{\mathrm{m}}(X,0) = \begin{cases} \dfrac{1}{2}\displaystyle\sum_{\sigma\in S_X} \operatorname{sgn}(\sigma) \prod_{j=1}^{X} -2\Gamma(1-(j-\sigma_j),0) & \text{for } X \text{ odd} \\ 0 & X \text{ even,} \end{cases} \tag{3.156}$$

which can be expressed as a Toeplitz determinant

$$G_{\mathrm{m}}(X,0) = \frac{1}{2}\det T_X \qquad \text{for } X \text{ odd,} \tag{3.157}$$

where $T_X$ is an $X \times X$ matrix with elements $(T_X)_{j,j'} = -2\Gamma(1-(j-j'),0)$.

From Table 3.1, the first two non-zero values are

$$G_{\mathrm{m}}(1,0) = \frac{\rho_x}{\alpha} \tag{3.158}$$

$$G_{\mathrm{m}}(3,0) = \frac{4\rho_x}{\alpha^5}\left[(1+\alpha^2)^2\rho_x^2 - \frac{\alpha^2}{\pi^2}\right] \tag{3.159}$$

[cf. Eqs. (11.1) and (11.3) of Ref. [29]], where, up to a factor of $\alpha$, the former is equivalent to the occupation probability of a horizontal bond as calculated in Sec. 3.6.2.

To calculate the asymptotic behavior for large $X$, we define $\varphi(k) = -2\sum_{j=-\infty}^{\infty} \mathrm{e}^{\mathrm{i}kj}\Gamma(1-j,0) = -\mathrm{e}^{\mathrm{i}k}\mathrm{e}^{2\mathrm{i}\theta_k}\,\mathrm{sgn}(k)$ for $-\pi \le k < \pi$. Unlike on the triangular lattice [82, 83], Szegő's limit theorems do not apply, since $\varphi$ is not a continuous function, and instead we apply the Fisher–Hartwig conjecture [70].

The discontinuities at $k = 0$ and $k = \pm\pi$ can be expressed by defining $t_\beta(k) = \mathrm{e}^{-\mathrm{i}\beta(\pi-k)}$ for $0 < k < 2\pi$ [84], in terms of which $\varphi(k) = b(k)t_{1/2}(k)t_{1/2}(k-\pi)$. Here, $b(k) = -\mathrm{i}\mathrm{e}^{2\mathrm{i}\theta_k}$ is continuous and has zero winding number when viewed as a map from $\mathrm{e}^{\mathrm{i}k}$ to the unit circle. Its Wiener–Hopf factorization, $b(k) = b_+(\mathrm{e}^{\mathrm{i}k})b_-(\mathrm{e}^{\mathrm{i}k})$, with $b_+$ ($b_-$) analytic and nonzero everywhere inside (outside) the unit circle [85], is

$$b_\pm(z) = \sqrt{\pm\frac{c_\pm - z}{c_\pm + z}}\,, \tag{3.160}$$

where $c_\pm = \alpha^{-1} \pm \sqrt{1+\alpha^{-2}}$.

According to the Fisher–Hartwig conjecture [84], we then have

$$\det T_X \approx G[b]^X X^\Omega E\,, \tag{3.161}$$

for large $X$, with $G[b] = 1$, $\Omega = -\frac{1}{2}$ and

$$E = \frac{2^{2/3}\mathrm{e}^{6\zeta'(-1)}}{(1+\alpha^2)^{1/4}} \simeq \left(\frac{1+\alpha^2}{2}\right)^{-1/4} \times 0.494744\,, \tag{3.162}$$

where $\zeta'$ is the derivative of the Riemann zeta function.

The monomer distribution function therefore obeys

$$G_{\mathrm{m}}(X,0) \approx \frac{E}{2\sqrt{X}} \qquad \text{for } X \gg 1, \text{ odd}, \tag{3.163}$$

which is consistent with the numerical result reported in Ref. [29] for $\alpha = 1$. Note that the algebraic dependence on $X$, stemming mathematically from the discontinuity in $\varphi$, contrasts with the exponential behavior on the triangular lattice [82, 83].

## 3.7 Conclusions

We have expressed Lieb's transfer matrix for the classical square-lattice dimer model in terms of a free-fermion Hamiltonian, and used its spectrum to rederive some useful results. Although these can equally be derived using Pfaffian techniques, the second quantized approach presented in this chapter is perhaps more elegant.

Specifically, our results include the torus partition function which, by including a field $\boldsymbol{t}$, can be interpreted as a moment-generating function of the flux. We have also shown how expectation values can be expressed in terms of the fermionic operators, and evaluated dimer occupation numbers, dimer–dimer correlation functions and the monomer distribution function in the thermodynamic limit, all of which are independent of flux sector for not-too-large flux. Finally, we have derived a new result, namely the asymptotic behavior of the monomer distribution function for large monomer separation.

The results in this chapter are also relevant to the corresponding quantum dimer model at its Rokhsar–Kivelson point [86], while the transfer-matrix method can be extended to other two-dimensional lattices. Indeed, the straightforward generalization of Lieb's transfer matrix to the (bipartite) honeycomb and square-octagon lattices, which can both be viewed as a square lattice with certain horizontal bonds removed [i.e., certain terms omitted from the sum in $V_3$; see Eq. (3.8)], has already been demonstrated in Ref. [87].

One advantage of the transfer-matrix method is that dimer–dimer interactions can be easily included in the operator formalism, in terms of products of the dimer occupation numbers $d_{j,x}$ and $d_{j,y}$. For example, on a row of vertical bonds, the operator $\sum_j d_{j,y} d_{j+1,y}$ describes interactions between parallel pairs of nearest-neighbor dimers, as studied in Refs. [9, 10]. This is a four-fermion interaction,

which is non-integrable [10] but could be included perturbatively using standard diagrammatic perturbation theory.

Furthermore, the well-known height field theory [31,32] of the two-dimensional classical dimer model can be rigorously derived from the free-fermion form, by taking a long-wavelength limit and using the technique of bosonization [30]. Interaction operators included perturbatively in this context manifest themselves through renormalization of the 'stiffness' as well as the introduction of (cosine) potential terms consistent with symmetry requirements. A detailed account of this derivation will be the subject of the next chapter.

# Appendices

## 3.A Jacobi theta functions

In terms of the complex number $y$ and the nome $q$ with $|q| < 1$, the Jacobi theta functions are [68]

$$\begin{aligned}\theta_1(y|q) &= -\mathrm{i}\sqrt{y}q^{1/12}\eta(q)\prod_{n=1}^{\infty}(1-yq^n)(1-y^{-1}q^{n-1}) \\ &= -\mathrm{i}\sum_{r\in\mathbb{Z}+1/2}(-1)^{r-1/2}y^r q^{r^2/2}\end{aligned} \tag{3.A.1}$$

$$\begin{aligned}\theta_2(y|q) &= \sqrt{y}q^{1/12}\eta(q)\prod_{n=1}^{\infty}(1+yq^n)(1+y^{-1}q^{n-1}) \\ &= \sum_{r\in\mathbb{Z}+1/2}y^r q^{r^2/2}\end{aligned} \tag{3.A.2}$$

$$\begin{aligned}\theta_3(y|q) &= q^{-1/24}\eta(q)\prod_{n=1}^{\infty}(1+yq^{n-1/2})(1+y^{-1}q^{n-1/2}) \\ &= \sum_{n\in\mathbb{Z}}y^n q^{n^2/2}\end{aligned} \tag{3.A.3}$$

$$\begin{aligned}\theta_4(y|q) &= q^{-1/24}\eta(q)\prod_{n=1}^{\infty}(1-yq^{n-1/2})(1-y^{-1}q^{n-1/2}) \\ &= \sum_{n\in\mathbb{Z}}(-1)^n y^n q^{n^2/2}\,,\end{aligned} \tag{3.A.4}$$

where the Dedekind eta function

$$\eta(q) = q^{1/24} \prod_{n=1}^{\infty} (1 - q^n) \,. \tag{3.A.5}$$

# Chapter 4

# Derivation of field theory for the classical dimer model using bosonization

## 4.1 Introduction

In statistical mechanics, certain two-dimensional lattice models with hard constraints can be described in terms of effective field theories known as 'height models'. These include vertex, coloring and frustrated spin models [4, 31, 32, 52], as well as the dimer model defined on bipartite lattices [4, 10]. As discussed in detail in Chapter 2 for the dimer model, configurations are in one-to-one correspondence with an appropriately defined discrete-valued 'height' on the dual lattice, which encodes the hard constraints in a way amenable to coarse graining. Based on its non-trivial transformation properties under the symmetries [10], one can write down a field theory in terms of the coarse-grained height.

Height models have proven to be a powerful tool in understanding the physics of strongly-correlated systems. For the non-interacting dimer model, the Gaussian field theory has been used to calculate static properties, e.g., asymptotic behavior of dimer–dimer correlation functions for large separation [7], as well as to study dynamics [88,89]. Moreover, in the interacting case, the Gaussian action is perturbed by cosine terms consistent with the symmetries, which drive BKT phase transitions, as we have already discussed in Chapter 2.

As shown in Chapter 3, the square-lattice dimer model is exactly solvable and can be mapped to a free-fermion Hamiltonian in $1+1$ dimensions. Previously, Refs. [59,90] have pointed out that the height model can be viewed as a bosonized version of the fermionic description [30]. In this chapter, we start from the results of Chapter 3 and show these steps in full detail for a dimer model with anisotropic bond weights.

Our motivation for this is twofold. First, existing expressions in the literature for the dimer occupation variables in terms of the height [7, 59, 91, 92] allow one to correctly evaluate exponents of asymptotic dimer–dimer correlation functions, but not their coefficients. In our rigorous treatment, we show that this ambiguity is resolved by consistently including a cutoff in the height model, which arises naturally in the bosonization formalism. Second, the bosonization approach provides precise values for phenomenological parameters in the field theory, which are usually put in by hand. Although not particularly powerful in the non-interacting case, we return to the interacting double dimer model of Chapter 2 and show that, when combined with an RG analysis, this feature allows one to predict the shape of the phase boundary in the vicinity of the noninteracting point.

While most applications of height models in the physics literature are somewhat heuristic, previous studies of the dimer model have proven rigorously that the height converges to a Gaussian free field in the scaling limit [93, 94], and moreover that this holds even when the dimer model is rendered non-integrable by interactions [95, 96]. The case of general edge weights has also been investigated by Ref. [97].

We now give an outline of this chapter. Using the results of Chapter 3, we derive the field theory in Sec. 4.2, which includes both the action and dimer occupation variables, before making the connection with the height. This is extended to the interacting case in Sec. 4.3, allowing us to predict the phase boundary of the interacting double dimer model in the vicinity of the non-interacting point. We conclude in Sec. 4.4.

## 4.2 Derivation of field theory

In this section, we derive an effective field theory description of the standard dimer model using bosonization, starting from the transfer-matrix solution. A similar (but simpler) calculation for the XXZ spin chain is outlined in Appendix 4.C.3.

### 4.2.1 Action

The free-fermion Hamiltonian, Eq. (3.60), has dispersion $\epsilon(k)$ with 'left' and 'right' Fermi points, i.e., where $\epsilon(k) = 0$, at

$$k_{\mathrm{L}} = \pi \qquad \text{and} \qquad k_{\mathrm{R}} = 0\,, \tag{4.1}$$

respectively. Their corresponding Fermi velocities are

$$\partial_k \epsilon(k)\big|_{k=k_{\mathrm{L}}} = -\alpha \qquad \text{and} \qquad \partial_k \epsilon(k)\big|_{k=k_{\mathrm{R}}} = \alpha\,. \tag{4.2}$$

We wish to linearize the dispersion around the two Fermi points and extend each branch to infinity, as illustrated in Fig. 4.1. Hence, we define left- and right-moving fermions through

$$\zeta_k = L_{k_{\mathrm{L}}-k} + R_{k-k_{\mathrm{R}}}\,, \tag{4.3}$$

with Fourier series

$$r(x) = \frac{1}{\sqrt{L_x}} \sum_{k=-\infty}^{\infty} \mathrm{e}^{\mathrm{i}rkx} r_k\,, \tag{4.4}$$

and inverse

$$r_k = \frac{1}{\sqrt{L_x}} \int_0^{L_x} dx\, \mathrm{e}^{-\mathrm{i}rkx} r(x)\,, \tag{4.5}$$

where $r$ means $\{L, R\}$ in symbols and $\{-, +\}$ in equations, respectively. These definitions are chosen to be consistent with the bosonization prerequisites of Ref. [30] (see Appendix 4.C). [In real space, with $\psi_x = L_x^{-1/2} \sum_k \mathrm{e}^{\mathrm{i}kx} \zeta_k$, Eq. (4.3) reads $\psi_x = \mathrm{e}^{\mathrm{i}k_{\mathrm{L}}x} L(x) + \mathrm{e}^{\mathrm{i}k_{\mathrm{R}}x} R(x)$.] The linearization scheme is a good approximation provided one is only interested in low-lying excited states; otherwise the curvature of the dispersion becomes important. Hence, it is a long-wavelength

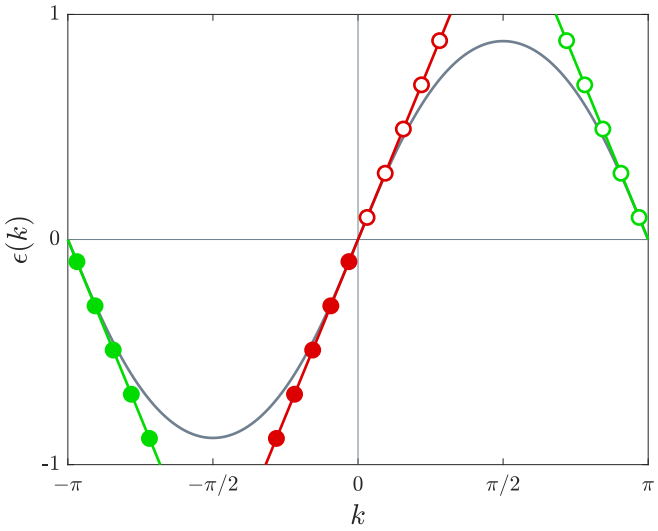


Figure 4.1: The dispersion $\epsilon(k) = \log\left[\sin k + (1+\sin^2 k)^{1/2}\right]$ (gray) is linearized around the two Fermi points at $k_{\mathrm{L}} = \pi$ and $k_{\mathrm{R}} = 0$; the left- (green) and right- (red) moving branches are then extended to infinity.

(small $k$) description, as is the case for a field theory.

Before linearizing an operator, it is necessary to normal-order all fermions in order to prevent divergences in the linearized theory. The procedure for fermion normal ordering is discussed in Appendix 4.B; for bilinears it only amounts to subtracting off the ground-state expectation value [see Eq. (4.B.2)], hence

$$\mathcal{H} = E_0(0) + \sum_k \epsilon(k) {:}\zeta_k^\dagger \zeta_k{:} \tag{4.6}$$

(we omit this constant from now on). Insertion of Eq. (4.3) and expansion of $\epsilon(k)$ to leading order around the Fermi points then yields

$$\mathcal{H} = \alpha \sum_k k \left( {:}L_k^\dagger L_k + R_k^\dagger R_k{:} \right) . \tag{4.7}$$

Here, the cross-terms $\alpha \sum_k k(L_k^\dagger R_{\pi-k} + R_k^\dagger L_{\pi-k})$ are dropped because they only contribute to high-energy processes. We transform to real space by inserting Eq. (4.5), and obtain

$$\mathcal{H} = \mathrm{i}\alpha \int_0^{L_x} dx \, \left[ {:}L^\dagger(x)\partial_x L(x) - R^\dagger(x)\partial_x R(x){:} \right] , \tag{4.8}$$

which is in a form suitable for bosonization. Note that this is now defined in

the continuum rather than on the lattice, since there is no Brillouin zone in the linearized theory.

The left- and right- moving fermions can be expressed, according to the bosonization identity [30], in terms of a boson field $\Phi$ and its canonically conjugate momentum variable $\Pi$ [see Eq. (4.C.26); we assume $L_x \to \infty$]. In Appendix 4.C, we provide full details of this mapping; however, in the main text we refer to the results summarized in Table 4.1. For the Hamiltonian, this implies

$$\mathcal{H} = \frac{\alpha}{2} \int_0^{L_x} dx \, \left[ :(\partial_x \phi)^2 + \Pi^2 : \right] , \tag{4.9}$$

where the right-hand side is now boson normal ordered (see Appendix 4.B.2), and

$$\phi(x) = (\delta_a * \Phi)(x) = \int_{-\infty}^{\infty} dx' \, \delta_a(x - x') \Phi(x') , \tag{4.10}$$

with $*$ denoting convolution and $\delta_a(x)$ a Lorentzian of width $a$. Here, $a > 0$ is an infinitesimal cutoff that arises in the bosonization formalism. In particular, Eq. (4.10) reduces to $\phi(x) = \Phi(x)$ in the limit $a \to 0$.

The partition function, Eq. (3.1), may be written as a path integral

$$Z = \int \mathcal{D}\Phi \, \mathrm{e}^{-S} , \tag{4.11}$$

where $S$ is the action. Correspondingly, the probability density functional for the field $\Phi(\boldsymbol{r})$ is

$$P[\Phi] = \frac{\mathrm{e}^{-S[\Phi]}}{Z} . \tag{4.12}$$

For the general boson Hamiltonian

$$\mathcal{H} = \frac{v_\mathrm{F}}{2} \int_0^{L_x} dx \, \left[ : \frac{1}{\mathcal{K}} (\partial_x \phi)^2 + \mathcal{K} \Pi^2 : \right] , \tag{4.13}$$

the action may be calculated by unnormal ordering and inserting complete sets of $\Phi$ eigenstates into Eq. (3.1), with result

$$S[\Phi] = \frac{1}{2\mathcal{K}} \int dx d\tau \, \left[ v_\mathrm{F} (\partial_x \phi)^2 + \frac{1}{v_\mathrm{F}} (\partial_\tau \Phi)^2 \right] , \tag{4.14}$$

where $\tau$ denotes imaginary time and $\phi(\boldsymbol{r}) = (\delta_a * \Phi)(\boldsymbol{r})$ (the convolution acts on

the $x$ coordinate only). Note that in the limit $a \to 0$ the action becomes

$$S[\phi] = \frac{1}{2\mathcal{K}} \int dx d\tau \, \left[ v_{\rm F} (\partial_x \phi)^2 + \frac{1}{v_{\rm F}} (\partial_\tau \phi)^2 \right] , \tag{4.15}$$

which is the usual Gaussian action for a free boson.

In the case of the dimer model, where $v_{\rm F} = \alpha$, $\mathcal{K} = 1$ and $\tau = y$, one obtains

$$S[\Phi] = \frac{1}{2} \int d^2 \boldsymbol{r} \, \left[ \alpha (\partial_x \phi)^2 + \frac{1}{\alpha} (\partial_y \Phi)^2 \right] . \tag{4.16}$$

This is the first element of our field theory: The entropic weight of dimer configurations with field $\Phi(\boldsymbol{r})$ is given by Eqs. (4.12) and (4.16). (All dimer configurations have equal weight in the non-interacting case, but the mapping between dimer configurations and $\Phi$ is many-to-one.) We previously conjectured an action of this form (with $\alpha = 1$ and $a \to 0$) in Eq. (2.9).

We now derive correlation functions of $\phi$, which will be useful in subsequent sections. In terms of the Fourier transform of $\Phi$,

$$\tilde{\Phi}(\boldsymbol{k}) = \frac{1}{2\pi} \int d^2 \boldsymbol{r} \, {\rm e}^{{\rm i} \boldsymbol{k} \cdot \boldsymbol{r}} \Phi(\boldsymbol{r}) \, , \tag{4.17}$$

the action is

$$\tilde{S}[\tilde{\Phi}] = \int d^2 \boldsymbol{k} \, \frac{1}{2} \left[ \alpha k_x^2 \tilde{\delta}_a(k_x)^2 + \frac{k_y^2}{\alpha} \right] |\tilde{\Phi}(\boldsymbol{k})^2| \, , \tag{4.18}$$

where $\tilde{\delta}_a(k) = \int_{-\infty}^{\infty} dx \, {\rm e}^{{\rm i}kx} \delta_a(x) = {\rm e}^{-|k|a}$, and so the correlation functions of $\tilde{\Phi}$ are

$$\langle \tilde{\Phi}(\boldsymbol{k}) \tilde{\Phi}(-\boldsymbol{k'}) \rangle = \frac{\delta^2(\boldsymbol{k} - \boldsymbol{k}')}{\alpha k_x^2 \tilde{\delta}_a(k_x)^2 + \frac{k_y^2}{\alpha}} \, . \tag{4.19}$$

Although the correlation function $\langle [\Phi(\boldsymbol{r}) - \Phi(\boldsymbol{r}')]^2 \rangle$ diverges in the UV (in fact linearly, rather than logarithmically as when $a = 0$), the correlation functions of $\phi$ are finite. From Eq. (4.10) and the inverse of Eq. (4.17) we have

$$\phi(\boldsymbol{r}) = \int \frac{d^2 \boldsymbol{k}}{2\pi} {\rm e}^{-{\rm i} \boldsymbol{k} \cdot \boldsymbol{r}} \tilde{\delta}_a(k_x) \tilde{\Phi}(\boldsymbol{k}) \, , \tag{4.20}$$

and hence

$$\left\langle [\phi(\boldsymbol{r}) - \phi(\boldsymbol{r}')]^2 \right\rangle = \frac{1}{\pi} \log\left(\frac{|\tilde{\boldsymbol{r}} - \tilde{\boldsymbol{r}}'|}{a}\right) + O\left(\frac{|\tilde{\boldsymbol{r}} - \tilde{\boldsymbol{r}}'|}{a}\right)^{-1}, \tag{4.21}$$

where $\tilde{\boldsymbol{r}} = (x, \alpha y)$. The cutoff $a$ therefore regularizes $\phi$ correlators. In a typical treatment, one would write down a field theory in the form of Eq. (4.15), i.e., with no cutoff built in. It is then necessary to insert a UV cutoff by hand when calculating $\phi$ correlators [4], leading to the same asymptotic form as Eq. (4.21) (but possibly with leading order corrections of order $a^0$).

### 4.2.2 Dimer occupation numbers

The entropic weights, i.e., Eqs. (4.12) and (4.16), are only useful when paired with expressions that relate the microscopic degrees of freedom, i.e., dimers, and the field $\Phi$, so that one can use the field theory to calculate observables. Therefore, in this section we derive expressions for the dimer occupation numbers on vertical and horizontal bonds in terms of $\Phi$, thus completing the field theory.

The calculation proceeds in analogy with the previous section, although the operators are more complicated. The first step is to normal order Eqs. (3.24) and (3.25) with respect to the ground state of the free-fermion Hamiltonian, Eq. (3.60). To do this we use Eqs. (4.B.2), (3.115) and (3.117) to find

$$d_{j,x} - \rho_x = -\alpha {:} C_j C_{j+1} {:} \tag{4.22}$$

$$d_{j,y} - \rho_y = {:} C_j^\dagger C_j {:} \tag{4.23}$$

(we have taken the thermodynamic limit).

To proceed, we derive a transformation from $C_j$ fermions to left- and right-moving fermions $r(x)$, by linearizing the transformation between $C_j$ and $\zeta_k$, Eq. (3.65). After inserting Eq. (4.3), extending the sum over $k$ to infinity and shifting the summation index we obtain

$$C(x) = \sqrt{\frac{2}{L_x}} \mathrm{e}^{-\mathrm{i}\pi/4} \sum_k \mathrm{e}^{\mathrm{i}kx} \times \begin{cases} \sin\theta_{k_\mathrm{R}-k} R_{-k}^\dagger - \sin\theta_{k_\mathrm{L}-k} L_k^\dagger & \text{for } x \text{ odd} \\ \cos\theta_{k_\mathrm{R}+k} R_k + \cos\theta_{k_\mathrm{L}+k} L_{-k} & x \text{ even.} \end{cases} \tag{4.24}$$

The low-energy description corresponds to $k \simeq 0$, so we expand around this value to leading order in $k$ using the Taylor series $\theta_{k_r - k} = \frac{\pi}{4} + r\frac{\alpha}{2}k$, which can be derived from Eq. (3.64). The remaining sums can be identified with real-space fermions according to Eq. (4.4), which yields

$$C(x) = \mathrm{e}^{-\mathrm{i}\pi/4} \times \begin{cases} (1 - \frac{\mathrm{i}\alpha}{2}\partial_x)R^\dagger - (1 + \frac{\mathrm{i}\alpha}{2}\partial_x)L^\dagger & \text{for } x \text{ odd} \\ (1 - \frac{\mathrm{i}\alpha}{2}\partial_x)R + (1 + \frac{\mathrm{i}\alpha}{2}\partial_x)L & x \text{ even.} \end{cases} \tag{4.25}$$

For the dimer occupation number on vertical bonds, inserting this result gives

$$\begin{aligned} d_y(x) - \rho_y = (-1)^x &\left(:L^\dagger L + R^\dagger R:\right) + \\ & L^\dagger R + R^\dagger L + \\ & \frac{\mathrm{i}\alpha}{2}\left[:L^\dagger \partial_x L - \left(\partial_x L^\dagger\right) L - R^\dagger \partial_x R + \left(\partial_x R^\dagger\right) R:\right] - \\ & \frac{\mathrm{i}\alpha}{2}(-1)^x \partial_x \left(L^\dagger R - R^\dagger L\right) , \end{aligned} \tag{4.26}$$

which is easily bosonized term-by-term using the results of Table 4.1:

$$\begin{aligned} d_y(x) - \rho_y = \frac{(-1)^x}{\sqrt{\pi}}\partial_x\phi + \frac{1}{\pi a}\cos(\sqrt{4\pi}\phi) + \\ \frac{\alpha}{2}\left[:(\partial_x\phi)^2 + \Pi^2:\right] + \frac{(-1)^x\alpha}{2\pi a}\partial_x \sin(\sqrt{4\pi}\phi) . \end{aligned} \tag{4.27}$$

Retaining only the most RG relevant terms, writing this in the path integral formulation is trivial and yields

$$d_y(\boldsymbol{r}) - \rho_y = \frac{(-1)^x}{\sqrt{\pi}}\partial_x\phi + \frac{1}{\pi a}\cos(\sqrt{4\pi}\phi) . \tag{4.28}$$

The constant on the left-hand side is the mean dimer occupation number [see Eq. (3.130)], while terms on the right-hand side encode (long-wavelength) fluctuations, including changes in flux sector. Note that the coefficient of the cosine term is cutoff dependent.

Similarly, for the dimer occupation number on horizontal bonds, the most RG relevant terms are

$$d_x(x) - \rho_x = \mathrm{i}\alpha(-1)^x(:L^\dagger L - R^\dagger R: + L^\dagger R - R^\dagger L) , \tag{4.29}$$

and bosonization yields

$$d_x(x) - \rho_x = \frac{\mathrm{i}(-1)^x \alpha}{\sqrt{\pi}} \Pi - \frac{(-1)^x \alpha}{\pi a} \sin(\sqrt{4\pi}\phi) \,. \tag{4.30}$$

In this case, the path integral step is non-trivial, and effectively removes the $\Pi$ term according to the equation of motion $\alpha\Pi = \mathrm{i}\partial_\tau \Phi$. Identifying $\tau = y$, we find

$$d_x(\boldsymbol{r}) - \rho_x = -\frac{(-1)^x}{\sqrt{\pi}} \partial_y \phi - \frac{(-1)^x \alpha}{\pi a} \sin(\sqrt{4\pi}\phi) \tag{4.31}$$

(we can safely take the limit $a \to 0$ in the first term). As expected from rotation symmetry requirements, the terms are similar in nature to those for $d_y$ in Eq. (4.28).

When $\alpha = 1$, Eqs. (4.28) and (4.31) are the same as the mappings between the dimer occupation numbers and the height (up to a linear transformation of $\phi$ that depends on the convention chosen for the height), which have previously been written down to leading order based on the definition of the height and symmetry considerations [7, 59, 91, 92]. We therefore identify $\phi$ as the height. In particular, requiring translation invariance of Eqs. (4.28) and (4.31) implies that $\phi(\boldsymbol{r}) \to -\phi(\boldsymbol{r} - \boldsymbol{\delta}_x)$ under translation in the $x$ direction by one lattice constant, while invariance under $\phi(\boldsymbol{r}) \to \phi(\boldsymbol{r}) + \sqrt{\pi}$, which is a consequence of the compactification radius of the boson in the bosonization identity of Eq. (4.C.12), reflects locality [10]. Taken together, these imply $\phi = \sqrt{\pi}(h + \frac{1}{8})$ in terms of the height $h$ defined in Chapter 2.

Our results for the dimer occupation numbers can be used to calculate asymptotic behavior of dimer–dimer correlation functions for large separation. As an example, we consider the connected correlation function of two horizontal dimers with separation $\boldsymbol{R}$:

$$G^{xx}(\boldsymbol{R}) = \langle d_x(\boldsymbol{r} + \boldsymbol{R}) d_x(\boldsymbol{r}) \rangle - \langle d_x(\boldsymbol{r} + \boldsymbol{R}) \rangle \langle d_x(\boldsymbol{r}) \rangle \,. \tag{4.32}$$

The only non-trivial terms are

$$\langle (\partial_y \phi(\boldsymbol{r} + \boldsymbol{R})) \, \partial_y \phi(\boldsymbol{r}) \rangle = \frac{\alpha^2}{2\pi} \frac{X^2 - (\alpha Y)^2}{[X^2 + (\alpha Y)^2]^2} \,, \tag{4.33}$$

which can be obtained by differentiating Eq. (4.21), and

$$\left\langle \sin\left(\sqrt{4\pi}\phi(\boldsymbol{r}+\boldsymbol{R})\right)\sin\left(\sqrt{4\pi}\phi(\boldsymbol{r})\right)\right\rangle = \frac{1}{4}\left\langle \mathrm{e}^{\mathrm{i}\sqrt{4\pi}[\phi(\boldsymbol{r}+\boldsymbol{R})-\phi(\boldsymbol{r})]} + \mathrm{c.c}\right\rangle \tag{4.34}$$

$$= \frac{a^2}{2[X^2+(\alpha Y)^2]}\,, \tag{4.35}$$

where, in the first line, terms involving the combination $\phi(\boldsymbol{r}+\boldsymbol{R})+\phi(\boldsymbol{r})$ average to zero, and in the second line we have used Eq. (4.21) with the result $\langle \mathrm{e}^A\rangle = \mathrm{e}^{\langle A^2\rangle/2}$ for a Gaussian random variable $A$ with zero mean. Combining these terms, one obtains

$$\frac{G^{xx}(\boldsymbol{R})}{\alpha^2} \approx (-1)^X \frac{X^2}{\pi^2[X^2+(\alpha Y)^2]^2}\,, \tag{4.36}$$

consistent with Eq. (3.140). As required for any observable, the result is not cutoff dependent; the factors of $a$ in Eqs. (4.31) and (4.35) cancel out. In previous work [7,59,91,92], the cutoff dependence of the coefficient of the sinusoidal term of Eqs. (4.28) and (4.31) was not recognized, leading to cutoff dependent correlators.

## 4.3 Interacting double dimer model

So far, we have only considered non-interacting dimers; in this section, we bosonize interactions and show how they modify the effective field theory (we set $\alpha = 1$ for simplicity). In particular, we return to the interacting double dimer model defined in Sec. 2.2. We have shown that this model exhibits a BKT phase transition between a standard Coulomb phase and a synchronized phase, and that the phase boundary passes through the non-interacting point $J = K = 0$.

Because we have diagonalized the two-row transfer matrix in Chapter 3, in the transfer-matrix formalism we must consider a reduced symmetry variation of this model, shown in Fig. 4.2, in which aligning interactions are restricted to alternate rows of vertical bonds (we also limit replica coupling to these bonds). Following Ref. [15], we refer to this as the 1-GS model, since it has a single ground state for $J < 0$ and $K < 0$. [Eq. (2.2) is the 4-GS model in this naming scheme.]

Denoting by $W^{(\alpha)}$ the two-row transfer-matrix in replica $\alpha$, the two-row trans-

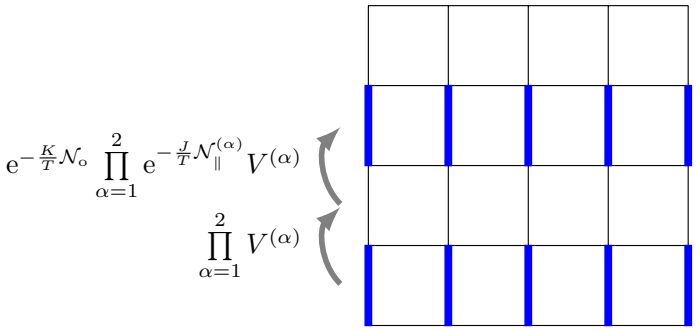


Figure 4.2: The 1-GS model [15]: dimer–dimer interactions in the interacting double dimer model, Eq. (2.2), are only counted on alternate rows of vertical bonds (blue). Equations show how the corresponding two-row transfer matrix $W_{\text{1-GS}}$, defined in Eq. (4.37), is constructed.

fer matrix for the 1-GS model is given by (see Fig. 4.2)

$$W_{\text{1-GS}} = \mathrm{e}^{-\frac{K}{T}\mathcal{N}_\mathrm{o}} \prod_{\alpha=1}^{2} \mathrm{e}^{-\frac{J}{T}\mathcal{N}_\parallel^{(\alpha)}} W^{(\alpha)} \,, \tag{4.37}$$

where the operator

$$\mathcal{N}_\parallel^{(\alpha)} = \sum_{j=1}^{L_x} d_{j,y}^{(\alpha)} d_{j+1,y}^{(\alpha)} \tag{4.38}$$

counts the number of parallel pairs of nearest-neighbor dimers in replica $\alpha$ on a row of vertical bonds, and the operator

$$\mathcal{N}_\mathrm{o} = \sum_{j=1}^{L_x} d_{j,y}^{(1)} d_{j,y}^{(2)} \tag{4.39}$$

counts the number of overlapping dimers on a row of vertical bonds [caligraphic font is used to distinguish $\mathcal{N}_\parallel^{(\alpha)}$ and $\mathcal{N}_\mathrm{o}$ from the terms in Eq. (2.2), which include the whole lattice]. The four-fermion interactions of Eqs. (4.38) and (4.39) are non-integrable [10], so we turn to perturbation theory.

Instead of perturbing the eigenvalues and eigenvectors of $\mathcal{H}$, we add perturbations to the effective field theory of Eq. (4.16) using bosonization. For the 1-GS model, we define the corresponding one-dimensional quantum Hamiltonian $\mathcal{H}_{\text{1-GS}}$ through

$$W_{\text{1-GS}} = \mathrm{e}^{-2\mathcal{H}_{\text{1-GS}}} \,, \tag{4.40}$$

which, from Eq. (4.37), is given by

$$\mathcal{H}_{\text{1-GS}} = -\frac{1}{2}\log\left(\mathrm{e}^{-\frac{K}{T}\mathcal{N}_{\text{o}}}\prod_{\alpha=1}^{2}\mathrm{e}^{-\frac{J}{T}\mathcal{N}_{\parallel}^{(\alpha)}}\mathrm{e}^{-2\mathcal{H}^{(\alpha)}}\right). \tag{4.41}$$

In the subsequent sections we bosonize $\mathcal{N}_{\parallel}^{(\alpha)}$ and $\mathcal{N}_{\text{o}}$ in the free theory, and use these results to calculate Eq. (4.41), and hence the corresponding 1-GS model action, perturbatively in the couplings $J$ and $K$. From this we infer the action of the 4-GS model, Eq. (2.2), which allows one to predict the shape of the phase boundary near the non-interacting point $J = K = 0$.

### 4.3.1 Aligning interactions $\mathcal{N}_{\parallel}$

The calculation of $\mathcal{N}_{\parallel}$ (we drop replica indices in this section) in the free theory follows the procedure in Sec. 4.2.2 for the dimer occupation numbers. However, because this operator is quartic, rather than quadratic, in fermions, the algebra is more involved. A similar (but simpler) calculation for the XXZ spin chain is outlined in Appendix 4.C.3.

The first step is to normal order, which, using Eq. (4.B.3), yields

$$\mathcal{N}_{\parallel} - \frac{L_x}{8} = \sum_{j=1}^{L_x}\left[:C_j^\dagger C_j C_{j+1}^\dagger C_{j+1}: + \frac{1}{4}\left(:2C_j^\dagger C_j - C_j C_{j+1} + C_j^\dagger C_{j+1}^\dagger:\right)\right]. \tag{4.42}$$

Here, the constant on the left-hand side is equivalent to $\langle\mathcal{N}_{\parallel}\rangle$, while the bilinear terms on the second line can be written as

$$\frac{1}{2}\sum_{k}(1+\sin^2 k)\sin(2\theta_k):{\zeta_k}^\dagger\zeta_{k+\pi}: \tag{4.43}$$

in terms of $\zeta_k$ fermions. Note that normal ordering does not generate a term proportional to $\mathcal{H}$ in this case, in contrast to Eq. (4.C.65) for the XXZ spin chain.

In order to linearize the first term in Eq. (4.42), we insert Eq. (4.25) to obtain

$$
\begin{aligned}
:C_j^\dagger C_j C_{j+1}^\dagger C_{j+1}: = -:\left[L^\dagger(x)L(x)+R^\dagger(x)R(x)\right]\left[L^\dagger(x')L(x')+R^\dagger(x')R(x')\right]:+\\
:\left[L^\dagger(x)R(x)+R^\dagger(x)L(x)\right]\left[L^\dagger(x')R(x')+R^\dagger(x')L(x')\right]:+\\
\text{terms containing } (-1)^x \text{ that integrate to zero,}
\end{aligned}
\tag{4.44}
$$

where $x' = x + 1$ [the same terms are encountered for the XXZ spin chain in Eq. (4.C.66)]. Note that we retain only the most RG relevant terms, i.e., those without derivatives.

We now expand brackets and bosonize term-by-term using Table 4.1, taking the scaling limit $a \to 0$. In the first line, terms in a single-fermion species may be written [98]

$$
:r^\dagger(x)r(x)r^\dagger(x')r(x'): \approx (x'-x)^2 :r^\dagger(x)r(x)\partial_x r^\dagger(x)\partial_x r(x):, \tag{4.45}
$$

and are thus RG irrelevant. Note that, in this expansion, the zero order term $:r^\dagger(x)r(x)r^\dagger(x)r(x): = 0$ [99] because, from Eq. (4.B.4),

$$
:r^\dagger(x)r(x)r^\dagger(x')r(x'): = -:r^\dagger(x')r(x)r^\dagger(x)r(x'):. \tag{4.46}
$$

Meanwhile, after bosonization, the remaining (mixed) terms contribute

$$
-2:L^\dagger(x)L(x)::R^\dagger(x)R(x): = \frac{1}{2\pi}\left[:\Pi^2 - (\partial_x\phi)^2:\right]. \tag{4.47}
$$

From the second line, one obtains the Umklapp process

$$
L^\dagger(x)R(x)L^\dagger(x')R(x') + \text{h.c.} = \frac{1}{2(\pi a)^2}\cos\left\{\sqrt{4\pi}\left[\phi(x)+\phi(x')\right]\right\} \tag{4.48}
$$

$$
\simeq \frac{1}{2(\pi a)^2}\cos\left[\sqrt{16\pi}\phi(x)\right], \tag{4.49}
$$

as well as, again, Eq. (4.47).

The bilinear terms in Eq. (4.42) are easily bosonized by analogy with the

Hamiltonian in Sec. 4.2.1. We find

$$\frac{1}{2}\sum_k (1+\sin^2 k)\sin(2\theta_k) {:}\zeta_k^\dagger \zeta_{k+\pi}{:} = \frac{1}{2}\int_0^{L_x} dx\, (L^\dagger R + R^\dagger L) \tag{4.50}$$

$$= \frac{1}{2\pi a}\cos\left(\sqrt{4\pi}\phi\right) . \tag{4.51}$$

Finally, combining the most RG relevant terms, we obtain

$$\mathcal{N}_\parallel - \frac{L_x}{8} = \int_0^{L_x} dx \left\{ \frac{1}{\pi}\left[{:}\Pi^2 - (\partial_x\phi)^2{:}\right] + \frac{1}{2\pi a}\cos\left(\sqrt{4\pi}\phi\right)\right\} . \tag{4.52}$$

This result is not in agreement with Ref. [59], in which Papanikolaou *et al.* derive $\mathcal{N}_\parallel$ by substituting Eq. (4.27) into the continuum version of Eq. (4.38), before using an operator product expansion. Although this approach is equivalent to ours in the case of the XXZ spin chain (compare Sec. 4.C.3 and Ref. [100]), it is incorrect in the present case due to its failure to properly normal order $\mathcal{N}_\parallel$.

### 4.3.2 Replica coupling $\mathcal{N}_\mathrm{o}$

In contrast to $\mathcal{N}_\parallel$, one can calculate $\mathcal{N}_\mathrm{o}$ directly by substituting Eq. (4.27) into the continuum version of Eq. (4.39)

$$\mathcal{N}_\mathrm{o} = \int_0^{L_x} dx\, d_y^{(1)} d_y^{(2)} . \tag{4.53}$$

This is because operators with different replica indices commute and hence, provided $d_y^{(1)}$ and $d_y^{(2)}$ are each fermion normal ordered, the product $d_y^{(1)} d_y^{(2)}$ is also normal ordered. An analogous calculation for the Hubbard model, with spin playing the role of replica index, can be found in Ref. [100]. One can similarly construct an operator that counts the number of overlapping dimers on a row of horizontal bonds using $d_x$.

Retaining only the most RG relevant terms, one obtains

$$\begin{aligned}\mathcal{N}_{\rm o} - \frac{L_x}{16} = \int_0^{L_x} dx \Bigg\{ & \sum_{\alpha=1}^{2} \frac{1}{4\pi a} \cos\left(\sqrt{4\pi}\phi^{(\alpha)}\right) + \\ & \sum_{\alpha=1}^{2} \frac{1}{8} \left[ : \left(\partial_x \phi^{(\alpha)}\right)^2 + \left(\Pi^{(\alpha)}\right)^2 : \right] + \\ & \frac{1}{\pi} \left(\partial_x \phi^{(1)}\right) \left(\partial_x \phi^{(2)}\right) + \\ & \frac{1}{(\pi a)^2} \cos\left(\sqrt{4\pi}\phi^{(1)}\right) \cos\left(\sqrt{4\pi}\phi^{(2)}\right) \Bigg\}\end{aligned} \tag{4.54}$$

[note that the second term derives from higher-order terms in $d_y$; see Eq. (4.27)]. Here, the constant on the left-hand side is equivalent to $\langle \mathcal{N}_{\rm o} \rangle = \sum_j \langle d_{j,y}^{(1)} \rangle \langle d_{j,y}^{(2)} \rangle$, while replicas are coupled by the third and fourth terms.

### 4.3.3 1-GS model

We calculate $\mathcal{H}_{\text{1-GS}}$ from Eq. (4.41) under the assumptions $|J/T| \ll 1$ and $|K/T| \ll 1$. In this limit, interactions only excite particle-hole pairs near the Fermi points of the free theory (see Fig. 4.1), and hence the linearization scheme used to calculate $\mathcal{H}$, $\mathcal{N}_\parallel$ and $\mathcal{N}_{\rm o}$ in Eqs. (4.9), (4.52) and (4.54) remains valid.

The operators $\mathcal{N}_\parallel^{(\alpha)}$ and $\mathcal{N}_{\rm o}$ do not commute with $\mathcal{H}^{(\alpha)}$ (although $[\mathcal{N}_\parallel^{(\alpha)}, \mathcal{N}_{\rm o}] = 0$), so the Baker–Campbell–Hausdorff formula, Eq. (4.A.1), is required to simplify Eq. (4.41). To linear order in the couplings this gives

$$\begin{aligned}\mathcal{H}_{\text{1-GS}} \approx & \sum_{\alpha=1}^{2} \left( \mathcal{H}^{(\alpha)} + \frac{1}{2}\frac{J}{T} \mathcal{N}_\parallel^{(\alpha)} \right) + \frac{1}{2}\frac{K}{T} \mathcal{N}_{\rm o} + \\ & \frac{1}{2} \sum_{\alpha=1}^{2} \left[ \mathcal{H}^{(\alpha)}, \frac{K}{T}\mathcal{N}_{\rm o} + \frac{J}{T}\mathcal{N}_\parallel^{(\alpha)} \right] - \\ & \frac{1}{3} \sum_{\alpha,\alpha'=1}^{2} \left[ \mathcal{H}^{(\alpha)}, \left[ \mathcal{H}^{(\alpha')}, \frac{K}{T}\mathcal{N}_{\rm o} + \frac{J}{T}\mathcal{N}_\parallel^{(\alpha')} \right] \right] + \dots ,\end{aligned} \tag{4.55}$$

where '…' refers to additional terms with three or more nested commutators and one $\frac{K}{T}\mathcal{N}_{\rm o} + \frac{J}{T}\mathcal{N}_\parallel^{(\alpha)}$. In fact, we need only retain terms on the first line. To see this, note that $[\mathcal{H}, \zeta_k] = -\epsilon(k)\zeta_k$, i.e., in the $\zeta_k$ basis each commutator of $\mathcal{N}_\parallel^{(\alpha)}$ or $\mathcal{N}_{\rm o}$ with $\mathcal{H}^{(\alpha)}$ generates similar operators, but with an extra factor of

$\epsilon(k)$. Following through the usual steps to bosonize these operators, one finds that each factor of $\epsilon(k)$ manifests itself as an extra derivative. Hence, any term involving a commutator is less RG relevant than the terms on the first line.

Dropping these terms, and substituting Eqs. (4.9), (4.52) and (4.54) into Eq. (4.55) gives

$$\begin{aligned}\mathcal{H}_{\text{1-GS}} = \int_0^{L_x} dx \Bigg\{ \sum_{\alpha=1}^{2} \frac{1}{2} \Bigg[ : \frac{\kappa_x}{\pi} \left(\partial_x \phi^{(\alpha)}\right)^2 + \frac{\pi}{\kappa_y} \left(\Pi^{(\alpha)}\right)^2 : \Bigg] + \\ \frac{\lambda_x}{\pi} \left(\partial_x \phi^{(1)}\right) \left(\partial_x \phi^{(2)}\right) + \\ V \cos\left(\sqrt{4\pi}\phi^{(1)}\right) \cos\left(\sqrt{4\pi}\phi^{(2)}\right) \Bigg\}\end{aligned} \tag{4.56}$$

[we have dropped terms proportional to $\cos(\sqrt{4\pi}\phi^{(\alpha)})$], up to additive constants, where

$$\kappa_x = \pi \left(1 - \frac{1}{\pi}\frac{J}{T} + \frac{1}{8}\frac{K}{T}\right) \tag{4.57}$$

$$\kappa_y = \pi \left(1 + \frac{1}{\pi}\frac{J}{T} + \frac{1}{8}\frac{K}{T}\right)^{-1} \tag{4.58}$$

$$\simeq \pi \left(1 - \frac{1}{\pi}\frac{J}{T} - \frac{1}{8}\frac{K}{T}\right) \tag{4.59}$$

$$\lambda_x = \frac{1}{2}\frac{K}{T} \tag{4.60}$$

$$V = \frac{1}{2}\frac{K}{T}\frac{1}{(\pi a)^2}\,. \tag{4.61}$$

All RG irrelevant operators omitted in the derivation of Eq. (4.56) only modify these coefficients at higher order in $J/T$ and $K/T$ [59].

To perform the path integral, we diagonalize the quadratic terms through

$$\phi^{(\pm)} = \frac{1}{\sqrt{2}} \left(\phi^{(1)} \pm \phi^{(2)}\right) \tag{4.62}$$

$$\Pi^{(\pm)} = \frac{1}{\sqrt{2}} \left(\Pi^{(1)} \pm \Pi^{(2)}\right)\,, \tag{4.63}$$

where the coefficient is chosen to ensure that $\Phi^{(\pm)}$ has canonically conjugate momentum variable $\Pi^{(\pm)}$ [in the same way as $\Phi^{(\alpha)}$ and $\Pi^{(\alpha)}$; see Eq. (4.C.26)].

This yields

$$\mathcal{H}_{\text{1-GS}} = \sum_{\sigma\in\pm} \frac{1}{2} \int_0^{L_x} dx \left[ : \frac{2\kappa_{x,\sigma}}{\pi} \left(\partial_x \phi^{(\sigma)}\right)^2 + \frac{\pi}{\kappa_y} \left(\Pi^{(\sigma)}\right)^2 : + V \cos\left(\sqrt{8\pi}\phi^{(\sigma)}\right)\right], \tag{4.64}$$

with

$$\kappa_{x,\pm} = \frac{1}{2}(\kappa_x \pm \lambda_x)\,. \tag{4.65}$$

Then, according to Eqs. (4.13) and (4.14), the action is given by

$$S_{\text{1-GS}} = \sum_{\sigma\in\pm} \frac{1}{2} \int d^2\boldsymbol{r} \left[ \frac{2\kappa_{x,\sigma}}{\pi} \left(\partial_x \phi^{(\sigma)}\right)^2 + \frac{\kappa_y}{\pi} \left(\partial_y \Phi^{(\sigma)}\right)^2 + V \cos\left(\sqrt{8\pi}\phi^{(\sigma)}\right)\right], \tag{4.66}$$

which is a sine-Gordon theory in both height components $\phi^{(\pm)}$.

In each case, the Gaussian terms are of the same form as the non-interacting theory, Eq. (4.16), but with stiffness renormalized by the couplings $J$ and $K$ (we note that, even though both types of interaction are anisotropic, at first order anisotropy in the stiffnesses is only generated by $K$). The cosine terms [including those dropped $\sim \cos(\sqrt{4\pi}\phi^{(\alpha)})$] are those most RG relevant and consistent with constraints on the action due to locality and symmetry under simultaneous translation of both replicas by one lattice constant in the $x$ direction, as discussed in Sec. 4.2.2. They become RG relevant at sufficiently large stiffness and drive BKT transitions into ordered phases, in which $\phi^{(\pm)}$ are locked to discrete values.

### 4.3.4 4-GS model

To infer the action of the 4-GS model, we decompose the lattice into four bond families $i \in \{1,2,3,4\}$, defined in Fig. 4.3, associating couplings $J_i$ and $K_i$ to each. For general $\boldsymbol{J}$, $\boldsymbol{K}$, the action for the relative height takes the form

$$S_{\boldsymbol{J},\boldsymbol{K}} = \frac{1}{2} \int d^2\boldsymbol{r} \left[ \frac{2\tilde{\kappa}_{x,-}}{\pi} \left(\partial_x \phi^{(-)}\right)^2 + \frac{2\tilde{\kappa}_{y,-}}{\pi} \left(\partial_y \Phi^{(-)}\right)^2 + V^{(-)} \cos\left(\sqrt{8\pi}\phi^{(-)}\right)\right], \tag{4.67}$$

where $\tilde{\kappa}_{\mu,-}$ are functions of $\boldsymbol{J}$ and $\boldsymbol{K}$ with leading-order Taylor series

$$\tilde{\kappa}_{\mu,-}(\boldsymbol{J},\boldsymbol{K}) \approx \tilde{\kappa}_{\mu,-}(\boldsymbol{0},\boldsymbol{0}) + \sum_{i=1}^{4} \left[ \frac{J_i}{T} \frac{\partial \tilde{\kappa}_{\mu,-}}{\partial (J_i/T)} + \frac{K_i}{T} \frac{\partial \tilde{\kappa}_{\mu,-}}{\partial (K_i/T)} \right], \tag{4.68}$$

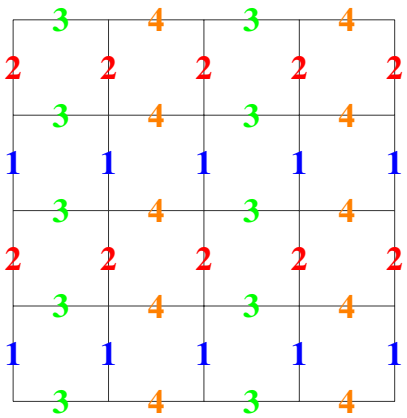


Figure 4.3: Definition of bond families $i \in \{1, 2, 3, 4\}$ associated with couplings $J_i$ and $K_i$. The 1-GS and 4-GS models correspond to $J_i = J\delta_{i,1}$, $K_i = K\delta_{i,1}$ (see Fig. 4.2) and $J_i = J\,\forall\, i$, $K_i = K\,\forall\, i$, respectively.

and similar for $V^{(-)}$. In the case of the 1-GS model with $J_i = J\delta_{i,1}$, $K_i = K\delta_{i,1}$, we have $\tilde{\kappa}_{x,-} = \kappa_{x,-}$, $\tilde{\kappa}_{y,-} = \frac{\kappa_y}{2}$, which allows us to read off from Eqs. (4.57)–(4.60) and Eq. (4.65)

$$\tilde{\kappa}_{\mu,-}(\mathbf{0}, \mathbf{0}) = \pi/2 \tag{4.69}$$

$$\partial_{J_1/T}\tilde{\kappa}_{x,-} = -1/2 \qquad \partial_{J_1/T}\tilde{\kappa}_{y,-} = -1/2 \tag{4.70}$$

$$\partial_{K_1/T}\tilde{\kappa}_{x,-} = \frac{\pi}{16} - \frac{1}{4} \qquad \partial_{J_1/T}\tilde{\kappa}_{y,-} = -\frac{\pi}{16}\,. \tag{4.71}$$

The remaining partial derivatives are related to the above by symmetry, i.e., $\partial_{J_1/T}\tilde{\kappa}_{\mu,-} = \partial_{J_2/T}\tilde{\kappa}_{\mu,-}$ and $\partial_{J_3/T}\tilde{\kappa}_{\mu,-} = \partial_{J_4/T}\tilde{\kappa}_{\mu,-}$ by translation symmetry, and $\partial_{J_3/T}\tilde{\kappa}_{x,-} = \partial_{J_1/T}\tilde{\kappa}_{y,-}$ and $\partial_{J_3/T}\tilde{\kappa}_{y,-} = \partial_{J_1/T}\tilde{\kappa}_{x,-}$ by rotation symmetry (and the same for $\boldsymbol{K}$ derivatives). Hence, the leading order dependence of the stiffnesses can be deduced for any choice of $\boldsymbol{J}$, $\boldsymbol{K}$; a similar argument holds for $V^{(-)}$.

In the case of the 4-GS model, where $J_i = J\,\forall\, i$, $K_i = K\,\forall\, i$, one then finds

$$S_{\text{4-GS}} = \int d^2\boldsymbol{r} \left[ \frac{\kappa_-}{\pi} \left(\partial_x \phi^{(-)}\right)^2 + \frac{\kappa_-}{\pi} \left(\partial_y \Phi^{(-)}\right)^2 + V^{(-)} \cos\left(\sqrt{8\pi}\phi^{(-)}\right) \right], \tag{4.72}$$

with

$$\kappa_- = \frac{\pi}{2}\left(1 - \frac{4}{\pi}\frac{J}{T} - \frac{1}{\pi}\frac{K}{T}\right) \tag{4.73}$$

$$V^{(-)} = \frac{K}{T}\frac{1}{(\pi a)^2}\,. \tag{4.74}$$

This form was deduced in Eq. (2.18) using a symmetry-based analysis. Here, we have determined how the phenomenological parameters $\kappa_-$ and $V^{(-)}$ depend on the microscopic couplings $J$ and $K$.

In order to determine the critical properties of $S_{\text{4-GS}}$, we appeal to an RG analysis. For the general sine-Gordon action

$$S_{\text{SG}}[\Phi] = \frac{1}{2\mathcal{K}}\int dx d\tau\, \left[v_{\text{F}}(\partial_x\phi)^2 + \frac{1}{v_{\text{F}}}(\partial_y\Phi)^2\right] + \frac{2g}{(2\pi a)^2}\cos(\sqrt{8\pi}\phi)\,, \tag{4.75}$$

one can show that the RG flow equations for $|g| \ll 1$ are given by [100]

$$\frac{dy_\parallel}{d\ell} = -y^2 \qquad \frac{dy}{d\ell} = -y_\parallel y\,, \tag{4.76}$$

where $y_\parallel = 2(\mathcal{K}-1)$ and $y = g/\pi v_{\text{F}}$. The RG flows described by these equations are illustrated in Fig. 4.4. In particular, since $ydy = y_\parallel dy_\parallel$, we have

$$y_\parallel^2 - y^2 = \text{const.}\,, \tag{4.77}$$

i.e., the trajectories are hyperbolas. There is a BKT phase transition along the separatrix

$$|y| = y_\parallel\,. \tag{4.78}$$

To the right, where $|y|$ flows to zero, the cosine term is irrelevant, i.e., it renormalizes to zero in the long distance theory, which is thus a free Coulomb phase. To the left, where $|y|$ flows to infinity, it is relevant and locks the height field to discrete values.

In the case of the 4-GS model, where $v_{\text{F}} = 1$, $\mathcal{K} = \pi/2\kappa_-$ and $g = 2K/T$,

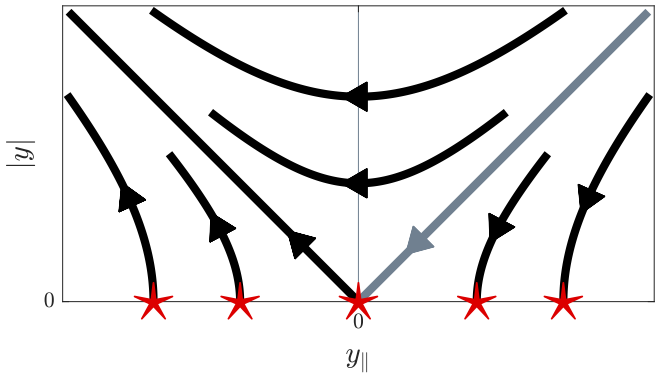


Figure 4.4: RG flows of the sine-Gordon action, Eq. (4.75), with $y_\parallel = 2(\mathcal{K}-1)$ and $y = g/\pi v_\mathrm{F}$. There is a line of fixed points (red stars) along $|y| = 0$, which are stable (unstable) for $y_\parallel > 0$ ($y_\parallel < 0$). The trajectories are hyperbolas, and the separatrix $|y| = y_\parallel$ (gray) divides regions where $|y|$ flows to zero and infinity.

Eq. (4.78) implies that there is a phase boundary at

$$\frac{J}{T} = \begin{cases} 0 & \text{for } \dfrac{K}{T} \geq 0 \\ -2\dfrac{K}{T} & \dfrac{K}{T} \leq 0, \end{cases} \tag{4.79}$$

in the vicinity of the non-interacting point. This finding is consistent with our numerical determination of the phase boundary in Fig. 2.3, using a MC worm algorithm. In particular, the data point closest to the origin is $(J/T, K/T) = (0.05, -0.097(9))$, while the phase boundary runs along the line $J/T = 0$ for positive $K/T$, as has previously been conjectured [20]. We have attempted to obtain data points closer to $K = 0$, but this is not possible because the finite-size scaling becomes more difficult.

## 4.4 Conclusions

In this chapter, we have rigorously derived the effective height theory that was written down in Chapter 2 based on symmetry. Our derivation, which started from the free-fermion Hamiltonian of Chapter 3, includes a long-wavelength approximation and utilizes the technique of bosonization. It could easily be applied to similar systems, e.g., the dimer model defined on other bipartite lattices [87], as well as other exactly-solvable 2D models with hard constraints.

In particular, we have derived effective field theory expressions for the action and dimer occupation numbers in the noninteracting case. By carefully keeping track of cutoffs in the bosonization formalism, we have used these to recover asymptotic dimer–dimer correlation functions calculated in Chapter 3, clearing up an ambiguity in the literature.

We then included aligning interactions and replica coupling perturbatively in the 1GS model, and worked out how this modifies the Gaussian action. Finally, we deduced the action of the model studied in Chapter 2, and used an RG analysis to infer the shape of the phase boundary in the vicinity of the noninteracting point. The result is in good agreement with our phase diagram, Fig. 2.3, obtained using a MC worm algorithm.

The approach employed in this chapter should also capture further features of the height theory, which have not been included in our treatment. For example, the operator $\sigma_j^-$ inserts a monomer on site $j$, and is known to take the form $\sigma_j^- \sim \mathrm{e}^{\pm \mathrm{i}\sqrt{\pi}\theta}$ in terms of the dual height field $\theta$ [10,92,101], with the sign depending on the sublattice.

Furthermore, one could include higher-order terms in the action of Eq. (4.16), by taking into account the curvature of the dispersion $\epsilon(k)$. Such 'band curvature' effects have previously been studied in quantum wires [102], as well as the XXZ spin chain [103]. In the isotropic dimer model, we expect these to take the form $|\boldsymbol{\nabla}^2\phi|^2$ and $|\boldsymbol{\nabla}\phi|^4$ [7, 91]. Although RG irrelevant, these terms can influence finite-size behavior and could in principle be measured in the MC simulations.

# Appendices

## 4.A Baker–Campbell–Hausdorff formula

The first few terms in the Baker–Campbell–Hausdorff formula are [77]

$$\log\left(\mathrm{e}^{A}\mathrm{e}^{B}\right) = A + B + \frac{1}{2}[A,B] + \frac{1}{12}\left([A,[A,B]] + [B,[B,A]\right) + \dots\,, \qquad (4.\mathrm{A}.1)$$

where '. . . ' refers to additional terms involving three or more nested commutators.

In the case $[A,[A,B]] = [B,[A,B]] = 0$, Eq. (4.A.1) implies

$$\mathrm{e}^{A}\mathrm{e}^{B} = \mathrm{e}^{A+B}\mathrm{e}^{[A,B]/2}\,, \tag{4.A.2}$$

and

$$\mathrm{e}^{A}\mathrm{e}^{B} = \mathrm{e}^{B}\mathrm{e}^{A}\mathrm{e}^{[A,B]}\,. \tag{4.A.3}$$

# 4.B Normal ordering

In this appendix we define fermion and boson normal ordering, denoted by $:\quad:$.

## 4.B.1 Fermions

In the $\zeta_k$ basis, $:\quad:$ means to anticommute all $\zeta_k^\dagger$ with $k \in [-\pi, 0]$ and all $\zeta_k$ with $k \in [0, \pi]$ to the right of all other creation and annihilation operators. For example, with $k, k' \in [-\pi, 0]$,

$$:\zeta_k^\dagger \zeta_{k'}: = -\zeta_{k'}\zeta_k^\dagger\,. \tag{4.B.1}$$

The meaning of $:\quad:$ for the left- and right- moving fermions $r_k$ then follows from Eq. (4.3): anticommute all $r_k^\dagger$ with $k < 0$ and all $r_k$ with $k > 0$ to the right of all other creation and annihilation operators of the same species [30].

In the case of two fermion operators, the above definitions of normal ordering are equivalent to

$$AB = :AB: + \langle AB\rangle_0\,, \tag{4.B.2}$$

where $\langle\cdot\rangle_0 \equiv {}_0\langle 0|\cdot|0\rangle_0$ denotes an expectation value in the ground state of the relevant Hamiltonian $\mathcal{H}$, i.e., Eqs. (4.6) and (4.7) in the cases $A, B \in \{\zeta_k; \zeta_k^\dagger\}$ and $\{r_k; r_k^\dagger\}$, respectively. For four fermion operators one requires the Wick expansion [98, 99, 104]

$$\begin{aligned} ABCD = :ABCD: &+ \langle AB\rangle_0 :CD: - \langle AC\rangle_0 :BD: + \langle AD\rangle_0 :BC: + \\ &\langle BC\rangle_0 :AD: - \langle BD\rangle_0 :AC: + \langle CD\rangle_0 :AB: + \\ &\langle AB\rangle_0\langle CD\rangle_0 - \langle AC\rangle_0\langle BD\rangle_0 + \langle AD\rangle_0\langle BC\rangle_0\,. \end{aligned} \tag{4.B.3}$$

Note that within normal ordering, any two fermion operators can be considered to anticommute, e.g.,

$$:ABCD: = -:BACD: . \tag{4.B.4}$$

### 4.B.2 Bosons

For boson operators, to be introduced in the next section, : : means to commute all annihilation operators $b_{qr}$ to the right of all creation operators $b^\dagger_{qr}$ of the same species, e.g.,

$$:b_{qr}b^\dagger_{q'r}: = b^\dagger_{q'r}b_{qr} . \tag{4.B.5}$$

Boson and fermion normal ordering are not in general equivalent [105], but it will always be clear from context which we mean.

## 4.C Bosonization

This appendix provides a brief overview of (abelian) bosonization.

### 4.C.1 Bosonization identity

In this section we state the bosonization identity, which is an operator identity in Fock space, as well as defining the fermion and boson fields that appear within it. We follow Ref. [30] but with some changes to definitions of the fields; see Refs. [74, 100] for other useful resources.

We will consider left- $L(x)$ and right- $R(x)$ moving fermion fields, i.e.,

$$r(x) = \frac{1}{\sqrt{L_x}} \sum_{k=-\infty}^{\infty} \mathrm{e}^{\mathrm{i}rkx} r_k , \tag{4.C.1}$$

where $r$ means $\{L, R\}$ in symbols and $\{-, +\}$ in equations, respectively. Here, $r_k$ are fermion operators satisfying

$$\{r_k, r_{k'}\} = \delta_{rr'}\delta_{kk'} , \tag{4.C.2}$$

and $L_x$ is the number of lattice sites. We place the system on a ring with an-

tiperiodic boundaries, so that

$$k = \frac{2\pi}{L_x}\left(n_k - \frac{1}{2}\right), \qquad n_k \in \mathbb{Z}\,. \tag{4.C.3}$$

In the ground state $|0\rangle_0$, fermions are assumed to only occupy states with $k < 0$, i.e.,

$$r_k|0\rangle_0 = 0 \qquad \text{for} \qquad k > 0\,, \tag{4.C.4}$$

$$r_k^\dagger|0\rangle_0 = 0 \qquad \text{for} \qquad k < 0\,. \tag{4.C.5}$$

A useful operator is the fermion number operator

$$N_r = \sum_{k=-\infty}^{\infty} :r_k^\dagger r_k:\,, \tag{4.C.6}$$

which counts the number of fermions relative to the ground state (fermion normal ordering is defined in Appendix 4.B.1).

We now construct boson operators from the fermion operators. One can define boson creation and annihilation operators

$$b_{qr}^\dagger = \frac{\mathrm{i}}{\sqrt{n_q}} \sum_{k=-\infty}^{\infty} r_{k+q}^\dagger r_k\,, \tag{4.C.7}$$

where $q = \frac{2\pi n_q}{L_x}$ and $n_q \in \mathbb{Z}^+$, which generate particle-hole excitations and satisfy

$$[b_{qr}, N_{r'}] = [b_{qr}^\dagger, N_{r'}] = 0 \tag{4.C.8}$$

$$[b_{qr}, b_{q'r'}] = [b_{qr}^\dagger, b_{q'r'}^\dagger] = 0 \qquad [b_{qr}, b_{q'r'}^\dagger] = \delta_{rr'}\delta_{qq'}\,. \tag{4.C.9}$$

The boson fields that appear in the bosonization identity are the chiral fields

$$\phi_r(x) = \frac{\sqrt{\pi}}{L_x} N_r x + \varphi_r(x) + \varphi_r^\dagger(x)\,, \tag{4.C.10}$$

where

$$\varphi_r^\dagger(x) = \frac{r}{\sqrt{4\pi}} \sum_{q>0} \frac{1}{\sqrt{n_q}} \mathrm{e}^{-\mathrm{i}rqx} b_{qr}^\dagger \mathrm{e}^{-aq/2}\,. \tag{4.C.11}$$

Here, $a > 0$ is an infinitesimal cutoff required to regularize certain non-normal-

ordered expressions. Note that the chiral fields are not periodic, while their derivatives are.

The bosonization identity is [30]

$$r(x) = \frac{\mathrm{e}^{-\mathrm{i}r\frac{\pi}{L_x}x}}{\sqrt{L_x}} F_r {:}\mathrm{e}^{\mathrm{i}r\sqrt{4\pi}\phi_r(x)}{:} \tag{4.C.12}$$

$$= \frac{\mathrm{e}^{-\mathrm{i}r\frac{\pi}{L_x}x}}{\sqrt{2\pi a}} F_r \mathrm{e}^{\mathrm{i}r\sqrt{4\pi}\phi_r(x)} \,. \tag{4.C.13}$$

The Klein factors $F_r^\dagger$ and $F_r$ are required to increase and decrease the fermion number by one, respectively, which no combination of boson operators can achieve, while also ensuring anticommutation of different fermion species, i.e., $L(x)$ and $R(x)$. They obey the following commutation relations:

$$[b_{qr}, F_{r'}^\dagger] = [b_{qr}^\dagger, F_{r'}^\dagger] = [b_{qr}, F_{r'}] = [b_{qr}^\dagger, F_{r'}] = 0 \tag{4.C.14}$$

$$[N_r, F_{r'}^\dagger] = \delta_{rr'} F_r^\dagger \qquad [N_r, F_{r'}] = -\delta_{rr'} F_r \tag{4.C.15}$$

$$\{F_r^\dagger, F_{r'}\} = 2\delta_{rr'} \qquad F_r F_r^\dagger = F_r^\dagger F_r = 1 \,. \tag{4.C.16}$$

The first form of the bosonization identity, Eq. (4.C.12), is boson normal ordered (see Appendix 4.B.2). One can unnormal order by expanding the exponential

$${:}\mathrm{e}^{\mathrm{i}r\sqrt{4\pi}\phi_r(x)}{:} = \mathrm{e}^{\mathrm{i}r\frac{2\pi}{L_x}N_r x} \mathrm{e}^{\mathrm{i}r\sqrt{4\pi}\varphi_r^\dagger(x)} \mathrm{e}^{\mathrm{i}r\sqrt{4\pi}\varphi_r(x)} \tag{4.C.17}$$

and using Eq. (4.A.2) with the commutator

$$[\varphi_r(x), \varphi_{r'}^\dagger(y)] = \frac{\delta_{rr'}}{4\pi} \sum_{q>0} \frac{1}{n_q} \mathrm{e}^{q[\mathrm{i}r(x-y)-a]} \tag{4.C.18}$$

$$= -\frac{\delta_{rr'}}{4\pi} \log\left[1 - \mathrm{e}^{\mathrm{i}\frac{2\pi}{L_x}[r(x-y)+\mathrm{i}a]}\right], \tag{4.C.19}$$

to obtain the second form, Eq. (4.C.13).

In practice, it is useful to define the fields

$$\phi = \phi_L + \phi_R \tag{4.C.20}$$

$$\theta = \phi_L - \phi_R \,, \tag{4.C.21}$$

with $\Pi = \partial_x \theta$. Using Eq. (4.C.18) and the identity

$$\sum_{n\in\mathbb{Z}} \mathrm{e}^{\mathrm{i}ny}\mathrm{e}^{-\lambda|n|} = 2\pi \sum_{\bar{n}\in\mathbb{Z}} \delta_\lambda(y - 2\pi\bar{n}), \qquad \lambda > 0\,, \tag{4.C.22}$$

where

$$\delta_\lambda(x) = \frac{\lambda}{\pi}\frac{1}{\lambda^2 + x^2} \tag{4.C.23}$$

is a Lorentzian of width $\lambda$, we have

$$[\phi(x), \Pi(x')] = \mathrm{i}\left[\sum_{n\in\mathbb{Z}} \delta_a(x - x' - nL_x) - \frac{1}{L_x}\right]. \tag{4.C.24}$$

We also define a field $\Phi$ through

$$\phi(x) = (\delta_a * \Phi)(x) = \int_{-\infty}^{\infty} dx'\, \delta_a(x - x')\Phi(x')\,, \tag{4.C.25}$$

where $*$ denotes convolution, which has commutator

$$[\Phi(x), \Pi(x')] = \mathrm{i}\left[\sum_{n\in\mathbb{Z}} \delta(x - x' - nL_x) - \frac{1}{L_x}\right], \tag{4.C.26}$$

i.e., $\Pi$ plays the role of the canonically conjugate momentum variable to $\Phi$ in the thermodynamic limit $L_x \to \infty$. Note that the field $\phi$ is not periodic, and satisfies

$$\phi(x + L_x) = \phi(x) + \sqrt{\pi}(N_L + N_R)\,. \tag{4.C.27}$$

### 4.C.2 Bosonization dictionary

We now use the bosonization identity to derive a 'dictionary' of useful bosonization formulae, as summarized in Table 4.1.

In order to bosonize bilinears (and their derivatives) that contain a single fermion species, as shown in rows 1–4 of Table 4.1, we define a generating function

$$G_r(x, y) = :r^\dagger(x)r(y): \tag{4.C.28}$$

$$= r^\dagger(x)r(y) - \langle r^\dagger(x)r(y)\rangle_0\,, \tag{4.C.29}$$

| Fermions | Bosons |
|---|---|
| $:L^\dagger L + R^\dagger R:$ | $\partial_x\phi/\sqrt{\pi}$ |
| $:L^\dagger L - R^\dagger R:$ | $\Pi/\sqrt{\pi}$ |
| $\frac{\mathrm{i}}{2}\left[:L^\dagger\partial_x L - (\partial_x L^\dagger)L - R^\dagger\partial_x R + (\partial_x R^\dagger)R:\right]$ | $\frac{1}{2}\left[:(\partial_x\phi)^2 + \Pi^2:\right]$ |
| $\mathrm{i}\int_0^{L_x} dx\,(:L^\dagger\partial_x L - R^\dagger\partial_x R:)$ | $\frac{1}{2}\int_0^{L_x} dx\ [:(\partial_x\phi)^2 + \Pi^2:]$ |
| $L^\dagger R + R^\dagger L$ | $\frac{1}{\pi a}\cos(\sqrt{4\pi}\phi)$ |
| $\frac{1}{\mathrm{i}}(L^\dagger R - R^\dagger L)$ | $\frac{1}{\pi a}\sin(\sqrt{4\pi}\phi)$ |

Table 4.1: Bosonization dictionary: Useful bosonization formulae, obtained using the bosonization identity, Eqs. (4.C.12) and (4.C.13), which relate bilinears in left- $L$ and right- $R$ moving fermion fields (left column) to expressions containing the boson field $\Phi$ and its canonically conjugate momentum variable $\Pi$ (right column). Note that $\Phi$ always appears as the convolution $\phi = \delta_a * \Phi$, where $\delta_a$ is a Lorentzian of width $a$.

such that

$$:(\partial_x^m r^\dagger)\partial_x^n r: = \lim_{y\to x}\partial_x^m\partial_y^n G_r(x,y)\,. \tag{4.C.30}$$

Note that products of fermion operators, such as those in Eq. (4.C.29), diverge when evaluated at coinciding points; in Eq. (4.C.30) this is regularized by 'point splitting' [106], i.e., we only manipulate expressions where fermions are evaluated at different points, $x$ and $y$, before finally taking the limit $y \to x$.

We construct $G_r(x,y)$ as follows. Inserting the bosonization identity, Eq. (4.C.12), yields

$$r^\dagger(x)r(y) = \frac{\mathrm{e}^{\mathrm{i}r\frac{\pi}{L}(x-y)}}{L_x}:\mathrm{e}^{-\mathrm{i}r\sqrt{4\pi}\phi_r(x)}::\mathrm{e}^{\mathrm{i}r\sqrt{4\pi}\phi_r(y)}: \tag{4.C.31}$$

[the product of Klein factors is unity from Eq. (4.C.16)]. To boson normal order the product of normal-ordered exponentials, we expand each exponential using Eq. (4.C.17), and use Eqs. (4.A.3) and (4.C.19) to exchange $\mathrm{e}^{-\mathrm{i}r\sqrt{4\pi}\varphi_r(x)}$ and

$e^{ir\sqrt{4\pi}\varphi_r^\dagger(y)}$, with result

$$r^\dagger(x)r(y) = \frac{:e^{-ir\sqrt{4\pi}[\phi_r(x)-\phi_r(y)]}:}{2iL_x \sin\left[-r\frac{\pi}{L_x}(x-y)\right]}\,. \tag{4.C.32}$$

Finally, because the expectation value of a normal-ordered exponential is unity, we obtain

$$G_r(x,y) = \frac{:e^{-ir\sqrt{4\pi}[\phi_r(x)-\phi_r(y)]}: - 1}{2iL_x \sin\left[-r\frac{\pi}{L_x}(x-y)\right]}\,. \tag{4.C.33}$$

The simplest terms are the densities of left- and right- movers, given by

$$:r^\dagger r: = \lim_{y\to x} G_r(x,y) \tag{4.C.34}$$

$$= \lim_{\epsilon\to 0} \frac{:e^{ir\sqrt{4\pi}\epsilon\partial_x\phi_r(x)}: - 1}{2ir\pi\epsilon} \tag{4.C.35}$$

$$= \frac{\partial_x\phi_r}{\sqrt{\pi}}\,. \tag{4.C.36}$$

Here, to obtain the second line, we rewrite $y = x+\epsilon$ in Eq. (4.C.33) before expanding the exponent and denominator to leading order in $\epsilon$. The third line follows after expanding the normal-ordered exponential. Hence, using Eqs. (4.C.20) and (4.C.21), we find

$$:L^\dagger L + R^\dagger R: = \frac{\partial_x\phi}{\sqrt{\pi}} \tag{4.C.37}$$

$$:L^\dagger L - R^\dagger R: = \frac{\Pi}{\sqrt{\pi}}\,, \tag{4.C.38}$$

as shown in rows 1 and 2 of Table 4.1.

Similarly, for the terms with first derivatives (see rows 3 and 4 of Table 4.1), we compute

$$\frac{i}{2}\left[:r^\dagger\partial_x r - (\partial_x r^\dagger)r:\right] = -r(\partial_x\phi_r)^2\,, \tag{4.C.39}$$

which implies

$$\frac{i}{2}\left[:L^\dagger\partial_x L - (\partial_x L^\dagger)L - R^\dagger\partial_x R + (\partial_x R^\dagger)R:\right] = \frac{1}{2}\left[:(\partial_x\phi)^2 + \Pi^2:\right]\,. \tag{4.C.40}$$

Integration over $x$ yields

$$\mathrm{i}\int_0^{L_x} dx\ \left(:L^\dagger\partial_x L - R^\dagger\partial_x R:\right) = \frac{1}{2}\int_0^{L_x} dx\ \left[:(\partial_x\phi)^2 + \Pi^2:\right]\ , \tag{4.C.41}$$

where the second and fourth terms on the left-hand side of Eq. (4.C.40) have been integrated by parts (boundary terms vanish due to antiperiodicity of $L$ and $R$).

We now bosonize bilinears that mix left- and right- movers, as shown in rows 5 and 6 of Table 4.1. To do so, we use the second form of the bosonization identity, Eq. (4.C.12), and consider

$$L^\dagger(x)R(y) = \frac{\mathrm{e}^{-\mathrm{i}\frac{\pi}{L_x}(x+y)}}{2\pi a}\mathrm{e}^{\mathrm{i}\sqrt{4\pi}\phi_L(x)}F_L^\dagger F_R\mathrm{e}^{\mathrm{i}\sqrt{4\pi}\phi_R(y)}\,. \tag{4.C.42}$$

The first exponential can be exchanged with the product of Klein factors using the following theorem [30]: If $[A,B] = DB$, where $[A,D] = [B,D] = 0$, it follows that $f(A)B = Bf(A+D)$. With $A = \phi_L$ and $B = F_L^\dagger$, Eqs. (4.C.10), (4.C.14) and (4.C.15) imply $D = \frac{\sqrt{\pi}}{L_x}x$, and hence

$$L^\dagger(x)R(y) = \frac{\mathrm{e}^{\mathrm{i}\frac{\pi}{L_x}(x-y)}}{2\pi a}F_L^\dagger F_R\mathrm{e}^{\mathrm{i}\sqrt{4\pi}[\phi_L(x)+\phi_R(y)]}\,. \tag{4.C.43}$$

By combining suitable derivatives of Eq. (4.C.43) and its Hermitian conjugate, and then setting $x = y$, one obtains sinusoidal terms in the boson field $\phi$ (Klein factors can be dropped). The simplest two cases are

$$L^\dagger R + R^\dagger L = \frac{1}{\pi a}\cos(\sqrt{4\pi}\phi)\,, \tag{4.C.44}$$

and

$$\frac{1}{\mathrm{i}}(L^\dagger R - R^\dagger L) = \frac{1}{\pi a}\sin(\sqrt{4\pi}\phi)\,. \tag{4.C.45}$$

### 4.C.3 XXZ spin chain

As an example, we use the bosonization dictionary to bosonize the XXZ spin chain, with Hamiltonian

$$\mathcal{H}_{\mathrm{XXZ}} = \sum_{j=1}^{L_x} \left( S_j^x S_{j+1}^x + S_j^y S_{j+1}^y + \Delta S_j^z S_{j+1}^z \right) \tag{4.C.46}$$

$$= \sum_{j=1}^{L_x} \left[ \frac{1}{2} (S_j^+ S_{j+1}^- + S_j^- S_{j+1}^+) + \Delta S_j^z S_{j+1}^z \right] , \tag{4.C.47}$$

where $\boldsymbol{S}_j = \frac{1}{2}\boldsymbol{\sigma}_j$ and $S_j^\pm = S_j^x \pm \mathrm{i} S_j^y$.

This model is exactly solvable through the Bethe ansatz, and can be expressed in the form of Eq. (4.13) with

$$v_{\mathrm{F}} = \frac{\pi}{2} \frac{\sin\varphi}{\varphi} \tag{4.C.48}$$

$$\mathcal{K} = \frac{\pi}{2(\pi - \varphi)} , \tag{4.C.49}$$

and $\cos\varphi = \Delta$ [107]. We will derive this result in the limit $|\Delta| \ll 1$ using bosonization.

We first map to spinless fermions using the Jordan–Wigner transformation, Eqs. (3.19)–(3.21), and perform the canonical transformation $C_j \to (-1)^j C_j$, to obtain

$$\mathcal{H}_{\mathrm{XXZ}} = \mathcal{H} + \mathcal{H}_{\mathrm{int}} \tag{4.C.50}$$

$$\mathcal{H} = -\frac{1}{2} \sum_{j=1}^{L_x} \left( C_j^\dagger C_{j+1} + \mathrm{h.c.} \right) \tag{4.C.51}$$

$$\mathcal{H}_{\mathrm{int}} = \Delta \sum_{j=1}^{L_x} \left( C_j^\dagger C_j - \frac{1}{2} \right) \left( C_{j+1}^\dagger C_{j+1} - \frac{1}{2} \right) . \tag{4.C.52}$$

Here, $\mathcal{H}$ describes free fermions with nearest-neighbor hopping, while $\mathcal{H}_{\mathrm{int}}$ contains fermion-fermion interactions.

**The case $\Delta = 0$**

We first treat the case $\Delta = 0$ and bosonize $\mathcal{H}$. Inserting the Fourier series

$$C_j = \frac{\mathrm{e}^{-\mathrm{i}\pi/4}}{\sqrt{L_x}} \sum_{k \in \mathbb{K}_p} \mathrm{e}^{\mathrm{i}kj} \eta_k \tag{4.C.53}$$

into Eq. (4.C.51) yields

$$\mathcal{H} = -\sum_k \cos k \eta_k^\dagger \eta_k \,, \tag{4.C.54}$$

hence there are Fermi points at $\pm k_\mathrm{F}$ with $k_\mathrm{F} = \frac{\pi}{2}$ (fermions occupy all states with $|k| < k_\mathrm{F}$ in the ground state $|0\rangle_0$). Using Eq. (4.B.2) and the correlator

$$\langle C_j^\dagger C_{j+1} \rangle_0 = -\langle C_j C_{j+1}^\dagger \rangle_0 = \frac{1}{\pi} \,, \tag{4.C.55}$$

the normal-ordered form in real space is then

$$\mathcal{H} = -\frac{1}{2} \sum_{j=1}^{L_x} \Big( :C_j^\dagger C_{j+1} + \mathrm{h.c.}: \Big) - \frac{L_x}{\pi} \,. \tag{4.C.56}$$

We linearize the dispersion by inserting

$$C_x = \mathrm{e}^{-\mathrm{i}k_\mathrm{F} x} L(x) + \mathrm{e}^{\mathrm{i}k_\mathrm{F} x} R(x) \tag{4.C.57}$$

[this is the real-space analog of Eq. (4.3) with $k_r = r k_\mathrm{F}$], and making the long-wavelength expansion

$$r(x + a_0) \simeq r(x) + a_0 \partial_x r(x) \,, \tag{4.C.58}$$

which gives

$$\mathcal{H} = \mathrm{i} \int_0^{L_x} dx \, (:L^\dagger \partial_x L - R^\dagger \partial_x R:) - \frac{L_x}{\pi} \tag{4.C.59}$$

(oscillatory cross terms integrate to zero). Finally, according to Table 4.1, the bosonized form is

$$\mathcal{H} = \frac{1}{2} \int_0^{L_x} dx \, \left[ :(\partial_x \phi)^2 + \Pi^2 : \right] - \frac{L_x}{\pi} \,. \tag{4.C.60}$$

We now find expressions for the microscopic degrees of freedom, i.e., the spin operators $\boldsymbol{S}_j$, in terms of $\phi$ and $\theta$. For $S^z_j$, we fermion normal order Eq. (3.21) using Eq. (4.B.2) and the correlator

$$\langle C^\dagger_j C_j \rangle_0 = \frac{1}{2}\,, \tag{4.C.61}$$

to obtain

$$S^z_j = :C^\dagger_j C_j: \,. \tag{4.C.62}$$

Linearization using Eq. (4.C.57) and subsequent bosonization using Table 4.1 results in

$$S^z(x) = :L^\dagger L + R^\dagger R: + (-1)^x (L^\dagger R + R^\dagger L) \tag{4.C.63}$$

$$= \frac{1}{\sqrt{\pi}} \partial_x \phi + \frac{(-1)^x}{\pi a} \cos(\sqrt{4\pi}\phi)\,. \tag{4.C.64}$$

[Bosonization of $\sigma^z_j$ in the dimer model is considerably more complicated because of the additional Bogoliubov transformation from $\eta_k$ to $\zeta_k$ fermions, Eq. (3.63), required to diagonalize $\mathcal{H}$.]

**The case $|\Delta| \ll 1$**

We now bosonize the interaction term $\mathcal{H}_{\text{int}}$, by linearizing around the Fermi points of the free-fermion theory. This is a perturbative treatment valid for $|\Delta| \ll 1$: The perturbation must be sufficiently small such that only particle-hole pairs near the Fermi points, i.e., those well-described by the linearization scheme, are excited.

To normal order, we use Eq. (4.B.3) with the correlators of Eqs. (4.C.55) and (4.C.61) to obtain

$$\mathcal{H}_{\text{int}} = \Delta \sum_{j=1}^{L_x} :C^\dagger_j C_j C^\dagger_{j+1} C_{j+1}: + \frac{2\Delta}{\pi}\mathcal{H} + \frac{\Delta L_x}{\pi^2}\,, \tag{4.C.65}$$

i.e., the four-fermion term remains but we also find a new term proportional to

$\mathcal{H}$. After inserting Eq. (4.C.57), the four-fermion term has linearized form

$$\begin{aligned} :C_j^\dagger C_j C_{j+1}^\dagger C_{j+1}: = &:\left[L^\dagger(x)L(x) + R^\dagger(x)R(x)\right]\left[L^\dagger(x')L(x') + R^\dagger(x')R(x')\right]: - \\ &:\left[L^\dagger(x)R(x) + R^\dagger(x)L(x)\right]\left[L^\dagger(x')R(x') + R^\dagger(x')L(x')\right]: + \\ &\text{terms containing } (-1)^x \text{ that integrate to zero,} \end{aligned} \tag{4.C.66}$$

where $x' = x + 1$. Bosonization of these terms in the scaling limit $a_0 \to 0$ is discussed in detail in Sec. 4.3.1 [see Eq. (4.44) and text thereafter], and gives

$$\mathcal{H}_{\text{int}} = \frac{2\Delta}{\pi}\int_0^{L_x} dx\, :(\partial_x\phi)^2: - \frac{2\Delta}{(2\pi a)^2}\cos\left[\sqrt{16\pi}\phi(x)\right] - \frac{\Delta L_x}{\pi^2}\,, \tag{4.C.67}$$

hence

$$\begin{aligned} \mathcal{H}_{\text{XXZ}} = \frac{1}{2}\int_0^{L_x} dx\, &\left[\left(1 + \frac{4\Delta}{\pi}\right):(\partial_x\phi)^2: + :\Pi^2:\right] - \\ &\frac{2\Delta}{(2\pi a)^2}\cos\left[\sqrt{16\pi}\phi(x)\right]\,. \end{aligned} \tag{4.C.68}$$

Under the transformation $\phi = \tilde{\phi}/\sqrt{2}$, $\Pi = \sqrt{2}\tilde{\Pi}$, and using Eqs. (4.13) and (4.14), the corresponding action takes the form of Eq. (4.75) with $v_{\text{F}} = 1 + \frac{2\Delta}{\pi}$, $\mathcal{K} = 2(1 - \frac{2\Delta}{\pi})$ and $g = -\Delta$. From the RG analysis of this action in Sec. 4.3.4, we see that the cosine term is RG irrelevant for $|\Delta| \ll 1$. One can thus write down an equivalent action with $(y, y_\parallel) \to (0, y_\parallel(0))$, where

$$y_\parallel(0) = \sqrt{y_\parallel^2 - y^2} \tag{4.C.69}$$

from Eq. (4.77). However, at leading order in $\Delta$ we have $y_\parallel(0) = y_\parallel$, and hence one can simply drop the cosine term from Eq. (4.C.68), i.e.,

$$\mathcal{H}_{\text{XXZ}} = \frac{1}{2}\int_0^{L_x} dx\, \left[\left(1 + \frac{4\Delta}{\pi}\right):(\partial_x\phi)^2: + :\Pi^2:\right]\,, \tag{4.C.70}$$

in agreement with Eq. (4.13) and the Taylor series of Eqs. (4.C.48) and (4.C.49) for $|\Delta| \ll 1$.

# Chapter 5

# Synchronization transition in the double dimer model on the cubic lattice

## 5.1 Introduction

In this chapter, we turn to the three-dimensional case. As for the double dimer model on the square lattice, we find a transition without any symmetry breaking, between a standard 'Coulomb' phase [6] and a 'synchronized' phase, where both replicas remain disordered but their relative fluctuations are suppressed. The synchronization transition on the cubic lattice is therefore an unusual example of a classical transition in 3D with no local order parameter.

It will be insightful to make a connection to loop models in the cubic-lattice case. Consider overlaying any pair of dimer configurations and deleting all dimers that coincide. As illustrated in Fig. 5.1, the result is a gas of directed loops, referred to as the 'transition graph' and corresponding to the set of dimer rearrangements that take one configuration to the other [12, 108]. A coupling that favors overlapping dimers then amounts to an energy cost per unit loop length. This makes possible a loop proliferation (or 'condensation') transition, between a phase at low $T$ with only sparse short loops and one at high $T$ with a finite density of boundary-spanning loops, as a result of competition between energy and entropy [109, 110]. (See Sec. 5.2 for a precise definition.) In terms of the

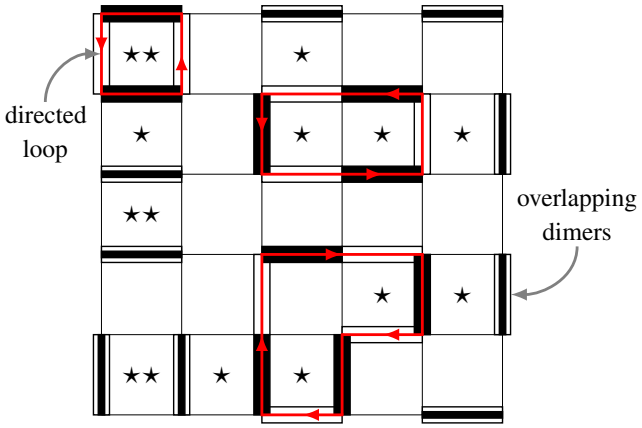


Figure 5.1: An example configuration of the double dimer model, in which two replicas of the close-packed dimer model (shown in black and white) are defined on the same lattice. Although we consider a cubic lattice, illustrations are shown on the square lattice for clarity. If overlapping dimers are deleted, the result is a gas of directed loops (red).

dimers, the proliferation of loops amounts to a synchronization transition.

In the subsequent sections we argue theoretically that the transition, if continuous, belongs in the inverted-XY universality class, and demonstrate using MC results that this is indeed the case. It can therefore be seen as an unusual example of a scalar Higgs transition, similar to the 1GS model [15] and the helical-field transition in spin ice [111, 112], but without any external symmetry breaking.

An outline of this chapter is as follows. In Sec. 5.2 we define the double dimer model, including couplings between and within replicas, and present theoretical arguments for its phase structure and critical properties. Our MC results, including a detailed study of the critical properties of the synchronization transition, are presented Sec. 5.3. Finally, in Sec. 5.4, we show that the double dimer model, including coupling between replicas, can be solved exactly on the Bethe lattice. We conclude in Sec. 5.5 with a brief comparison with the 2D case.

## 5.2 Model

We consider the cubic-lattice analog of the double dimer model defined in Sec. 2.2. Because the cubic lattice is also bipartite, one can still construct an effective magnetic field $B^{(\alpha)}_{\boldsymbol{r},\mu}$ and its associated flux $\boldsymbol{\Phi}^{(\alpha)}$ [see Eqs. (2.4) and (2.7)], although in three dimensions the divergence-free constraint is no longer resolved in terms

of a height.

### 5.2.1 Loop picture

When the two replicas are overlaid, the result can be interpreted as a set of directed loops. To see this, consider the relative magnetic field $B^{(-)}_{\boldsymbol{r},\mu} = B^{(1)}_{\boldsymbol{r},\mu} - B^{(2)}_{\boldsymbol{r},\mu}$, which takes values on each bond of $\pm 1$ or 0. The former is interpreted as a loop element directed along $\pm\boldsymbol{\delta}_\mu$, while the latter means that the dimers overlap and is interpreted as the absence of a loop element. Since the relative field is clearly also divergenceless, these elements indeed form a set of closed loops. Note that swapping the two replicas switches the direction of each loop. Adding a loop in $B^{(-)}_{\boldsymbol{r},\mu}$ that spans the system once in direction $\mu$ increases the relative flux $\Phi^{(-)}_\mu = \Phi^{(1)}_\mu - \Phi^{(2)}_\mu$ by one.

### 5.2.2 Phase diagram

The phase diagram of the double dimer model on the cubic lattice, obtained using the MC method detailed in Sec. 2.4, is shown in Fig. 5.2. In this section we define the phases shown and explain how the phase structure can be understood theoretically. In Sec. 5.3 we describe how the phase boundaries, as well as the critical properties at each, are determined in the simulations.

#### Independent replicas

We first review the phase structure for $K = 0$, where the two replicas act as independent (single) dimer models. For $K = J = 0$, the cubic dimer model exhibits a Coulomb phase [6, 8], in which the dimers are disordered and their correlations take a dipolar form. A single phase transition at $(J/T)_\mathrm{c} = -0.597$ separates this from a low-temperature phase with nonzero magnetization order parameter $\langle \boldsymbol{M} \rangle \neq \boldsymbol{0}$ [see Eq. (2.8)] [11]. The transition is apparently continuous with critical exponents compatible with the tricritical universality class. Theoretical arguments [15, 113, 114], however, suggest that the critical properties should be described by the so-called noncompact $\mathbb{CP}^1$ theory (see Sec. 5.2.3), and additional interactions [115,116] indeed modify the exponents to values compatible with this universality class [53].

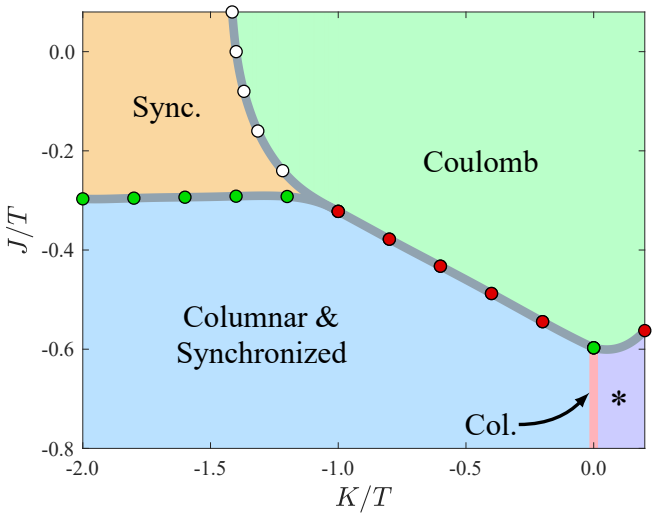


Figure 5.2: Phase diagram for the double dimer model of Eq. (2.2) on the cubic lattice, in the $(J/T, K/T)$ plane. Dots show points where the phase boundary has been determined using MC simulations, and thick grey lines are guides to the eye. The orange region, labeled 'Sync.' is the synchronized phase. The pink line labeled 'Col.' is the (unsynchronized) columnar phase, known to occur at $K = 0$, whilst the purple region, labeled '$*$', is the columnar & antisynchronized phase. Red dots represent first-order transitions, whilst green and white dots represent continuous transitions, in the tricritical and inverted-XY universality classes, respectively.

Besides the order parameter $\langle \boldsymbol{M} \rangle$, the Coulomb and columnar phases can be distinguished either through the flux or through the effective interactions between monomers. Consider first the latter, which involves introducing a test pair of monomers with opposite charge into the background of close-packed dimers. For $K = 0$, the replicas are independent, and so the monomer distribution function $G_{\mathrm{m}}$ (see Sec. 2.2.2 for a definition) reduces to that of the single dimer model. In the Coulomb phase for small $|J|/T$, $U_{\mathrm{m}} \equiv -\ln G_{\mathrm{m}}$ is a Coulomb potential at large separation, $U_{\mathrm{m}}(\boldsymbol{r}_+ - \boldsymbol{r}_-) \sim U_{\mathrm{m}}(\infty) - \kappa/(4\pi|\boldsymbol{r}_+ - \boldsymbol{r}_-|)$, where $\kappa$ (the 'flux stiffness') and $U_{\mathrm{m}}(\infty)$ are finite (positive) constants [6]. In the low-temperature phase, separating the monomers necessarily disrupts the columnar order along a string joining them [consider Figs. 5.3(a)–(c)], and so has a free-energy cost proportional to distance [6]. This qualitative distinction, between a confining interaction (preventing separation to infinite distance) at low $T$ and deconfinement at high $T$, provides an alternative characterization of the phase transition.

In practice, it is convenient to use the confinement length $\xi$ [see Eq. (2.28)],

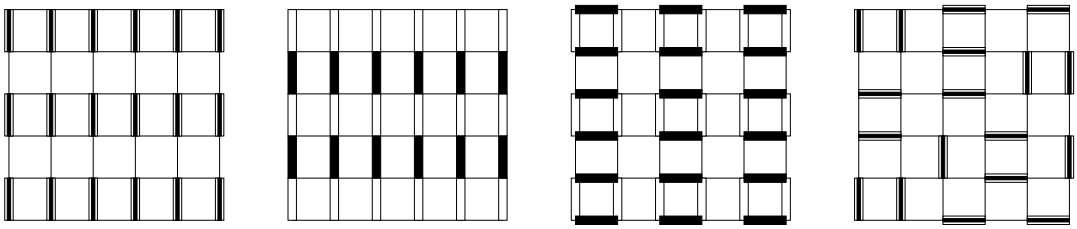


Figure 5.3: Example ground states of the double dimer model of Eq. (2.2), illustrated for the square lattice but applying also to the cubic lattice. (a)–(c) Columnar configurations, which minimize the energy for $J < 0$, $K = 0$. In each replica $\alpha \in \{1, 2\}$ (white and black dimers, respectively), the dimers are arranged in columns, maximizing the number of parallel plaquettes $N_{\parallel}^{(\alpha)}$ and hence minimizing the energy. For $K = 0$, the two replicas are uncoupled and so all three arrangements have equal energy. For $J < 0$, $K < 0$ configuration (a), the columnar & synchronized ground state, maximizes the overlap and hence minimizes the energy. Configurations (b) and (c) are columnar & antisynchronized, with replica magnetizations antiparallel and perpendicular respectively; both have zero overlap between replicas and so are degenerate ground states for $J < 0$, $K > 0$. (d) Example of a fully synchronized configuration, one of an extensive number of ground states for $J = 0$, $K < 0$. Each replica is disordered, but the overlap between their configurations is maximal, minimizing the energy.

which represents the root-mean-square separation of the test monomers. In the Coulomb phase, $G_{\mathrm{m}}(\boldsymbol{R}) \to \mathrm{e}^{-U_{\mathrm{m}}(\infty)/T} > 0$ for large separation, and so $\xi \sim L$. In the columnar phase, by contrast, $U_{\mathrm{m}}(\boldsymbol{R})$ grows without limit as $|\boldsymbol{R}| \to \infty$, $G_{\mathrm{m}}(\boldsymbol{R}) \to 0$, and so $\xi$ is an $L$-independent constant.

A related criterion for the phases can be expressed in terms of the flux $\boldsymbol{\Phi}^{(\alpha)}$. The mean flux vanishes by symmetry in both phases, while the variance, $\operatorname{Var} \boldsymbol{\Phi}^{(\alpha)} = \langle |\boldsymbol{\Phi}^{(\alpha)}|^2 \rangle$, scales differently with system size in the two: In the Coulomb phase, flux fluctuations are large, $\operatorname{Var} \boldsymbol{\Phi}^{(\alpha)} \approx L/\kappa$ [8]. In the columnar phase, the variance is exponentially small in $L$, because shifting dimers along a loop spanning the system disturbs the columnar order and hence costs energy $E \sim JL$.[1] Because the two replicas are independent, the variances of the total and relative flux $\boldsymbol{\Phi}^{(\pm)} = \boldsymbol{\Phi}^{(1)} \pm \boldsymbol{\Phi}^{(2)}$ are identical, and equally serve to distinguish the two phases.

[1] To see the connection to the monomer-confinement criterion, imagine changing the flux by removing a dimer to create a monomer pair, winding one monomer around the periodic boundaries, and then recombining the pair [117].

| | Coulomb | Columnar | Synchronized |
|---|---|---|---|
| Var $\mathbf{\Phi}^{(-)}$ | Large | Small | Small |
| Var $\mathbf{\Phi}^{(+)}$ | Large | Small | Large |
| $\xi$ | Large | Small | Small |

Table 5.1: Behavior in different phases of the double dimer model of: the variance of the flux difference, $\mathbf{\Phi}^{(-)} = \mathbf{\Phi}^{(1)} - \mathbf{\Phi}^{(2)}$; the variance of the total flux, $\mathbf{\Phi}^{(+)} = \mathbf{\Phi}^{(1)} + \mathbf{\Phi}^{(2)}$; and the confinement length, $\xi$. 'Small' means Var $\mathbf{\Phi}^{(\pm)}$ decreases exponentially with linear system size $L$ and $\xi$ is independent of $L$, while 'Large' means Var $\mathbf{\Phi}^{(\pm)} \sim L$ and $\xi \sim L$. In the columnar & (anti)synchronized phases, these observables behave as in the columnar phase.

### Coupled replicas

Consider now $J = 0$ and nonzero coupling $K < 0$ between replicas. If a monomer pair is inserted in replica 1, $B^{(2)}_{\boldsymbol{r},\mu}$ is divergenceless while $B^{(1)}_{\boldsymbol{r},\mu}$ has nonzero divergence at $\boldsymbol{r}_+$ and $\boldsymbol{r}_-$. This implies the presence of an open string in $B^{(-)}_{\boldsymbol{r},\mu}$ that runs between these two sites, and along which the two replicas differ. In the limit $K/T \to -\infty$, the string will take the shortest possible path, resulting in an energy proportional to separation and hence a confining effective interaction $U_{\mathrm{m}}$. Comparing this limit with the case where $K = 0$ (and $J = 0$), it follows that there must be a confinement transition, a qualitative change in the large-separation form of $U_{\mathrm{m}}$, between the two. In our results, shown in Fig. 5.2, we indeed find such a transition at a critical coupling $(K/T)_{\mathrm{c}} = -1.400$.

At temperatures above this point, where the entropy of the open string overcomes its energy cost, closed loops of $B^{(-)}_{\boldsymbol{r},\mu}$ are also free-energetically favorable. As a result, loops spanning the system boundaries, which cost an energy $E \sim KL$ and are hence suppressed exponentially in $L$ at low temperatures, 'proliferate' at the transition. Because these loops change the relative flux $\mathbf{\Phi}^{(-)}$, the high-temperature phase has Var $\mathbf{\Phi}^{(-)} \approx L/\kappa_-$, as at $K = 0$ but with a modified flux stiffness $\kappa_-$. By contrast, the variance of the total flux, Var $\mathbf{\Phi}^{(+)}$, is large ($\approx L/\kappa_+$) in both phases, because identical loops in both replicas costs zero energy [consider Fig. 5.3(d)]. The behavior of the flux variances in the different phases is summarized in Table 5.1.

While confinement and the flux variance thereby provide precise definitions of the phases, we also expect loop proliferation to reduce the overlap $\sum_l d^{(1)}_l d^{(2)}_l$

between the replicas. We therefore refer to the low-$T$, high-overlap phase as 'synchronized' and the high-$T$, low-overlap phase as 'unsynchronized', although the overlap is nonzero in both phases and so does not provide an order parameter in the strict sense.

It should be noted that the energy $\propto K$ associated with each element of a directed loop (or open string) is not the only contribution to its free-energy cost. In regions devoid of loops, overlapping dimers can be rearranged without changing the loop configuration. (For example, in the configuration of Fig. 5.1, flipping the parallel pair of overlapping dimers around the bottom-left plaquette in both replicas does not create a new directed loop). To leading order, this results in an entropy that scales with the number of overlapping dimers. Since the introduction of a directed loop reduces this number, and so the entropy, at finite $K/T$ we expect an additional free-energy cost per unit length of loops, which can be thought of as renormalizing $K/T$ towards more negative values.[2]

The arguments for the phase structure can be straightforwardly extended to include both $J/T$ and $K/T$. At large negative $J/T$ and $K = 0$, both replicas are columnar ordered, but the relative orientations of the two magnetizations $\boldsymbol{M}^{(1)}$ and $\boldsymbol{M}^{(2)}$ are arbitrary. Infinitesimal negative $K/T$ is sufficient to split this degeneracy extensively and therefore to synchronize the two replicas, giving the columnar & synchronized phase, illustrated in Fig. 5.3(a), with $\langle \boldsymbol{M}^{(1)} \rangle = \langle \boldsymbol{M}^{(2)} \rangle$.

For positive $K/T$, any pair of columnar configurations with distinct magnetizations has zero overlap and hence minimal energy. There is an accidental degeneracy, between antiparallel ($\boldsymbol{M}^{(1)} = -\boldsymbol{M}^{(2)}$) and perpendicular ($\boldsymbol{M}^{(1)} \cdot \boldsymbol{M}^{(2)} = 0$) magnetizations in the two replicas, illustrated in Figs. 5.3(b) and (c) respectively, which can be resolved by order by disorder [4, 118]. The elementary fluctuations, which involve flipping a single pair of parallel dimers around a plaquette, cost energy $+6|J|$ in both cases, but additionally may cost energy $+2K$ in the case of perpendicular magnetization. The free energy is therefore lower in the antiparallel arrangement, suggesting that this is selected by order by disorder. Our MC re-

[2]The significance of this effect can be estimated by comparing with a simple approximation that neglects it and treats the loops as simply costing energy $\frac{1}{2}|K|$ per unit length. (A loop of length $\ell$ reduces the number of overlapping dimers by $\frac{1}{2}\ell$.) This model has a proliferation transition at $T_c \simeq 0.33|K|$ [110]. In fact, our MC simulations give $T_c = 0.714|K|$ (see Fig. 5.6) – the additional free-energy cost of loops due to the entropy of overlapping dimers, neglected in our approximation, means a higher temperature is needed for them to proliferate.

sults (see Sec. 5.3.4) are indeed consistent with a phase where $\langle \boldsymbol{M}^{(1)} \rangle = -\langle \boldsymbol{M}^{(2)} \rangle$, which we refer to as columnar & antisynchronized.

Comparison with the single dimer model further allows some quantitative details of the phase boundaries to be inferred: The critical point separating the Coulomb and columnar phases for $K = 0$ is clearly $(J/T)_{\mathrm{c}} = -0.597$ as for the single dimer model. Similarly, when $K/T \to -\infty$, the two replicas are perfectly synchronized, and behave as a single dimer model with effective interaction $J_{\mathrm{eff}} = 2J$. The critical temperature for columnar ordering is therefore given by $\frac{1}{2}(J/T)_{\mathrm{c}} = -0.299$ in this limit. As shown in Fig. 5.2, the critical value of $J/T$ closely approximates this limiting value already for $K/T = -2$.

### 5.2.3 Field theories and critical properties

A continuum description for the Coulomb phase in the single dimer model is given by replacing the effective magnetic field $B_{\boldsymbol{r},\mu}$ by a continuum vector field $\boldsymbol{B}$ [6,8]. The latter is subject to the constraint $\boldsymbol{\nabla} \cdot \boldsymbol{B} = 0$, inherited from the close-packing constraint on the dimers, and hence can be expressed as $\boldsymbol{B} = \boldsymbol{\nabla} \times \boldsymbol{A}$ in terms of the vector potential $\boldsymbol{A}$. The continuum (Euclidean) action density is then given by

$$\mathcal{L}_{\mathrm{SDM}} = \frac{1}{2}\kappa |\boldsymbol{B}|^2 = \frac{1}{2}\kappa |\boldsymbol{\nabla} \times \boldsymbol{A}|^2 \,, \tag{5.1}$$

where $\kappa$ is the flux stiffness introduced in Sec. 5.2.2, plus irrelevant higher-order terms.

In the double dimer model, one can similarly introduce a continuum magnetic field $\boldsymbol{B}^{(\alpha)}$ for each replica, with the same stiffness $\kappa$ for each. The coupling $K$ leads to a term $\lambda \boldsymbol{B}^{(1)} \cdot \boldsymbol{B}^{(2)}$, with $\lambda \sim K$, and so an effective action for the unsynchronized Coulomb phase can be written as

$$\mathcal{L}_{\mathrm{DDM}} = \frac{1}{2}\kappa_+ |\boldsymbol{B}^{(+)}|^2 + \frac{1}{2}\kappa_- |\boldsymbol{B}^{(-)}|^2 \,, \tag{5.2}$$

where $\boldsymbol{B}^{(\pm)} = \boldsymbol{B}^{(1)} \pm \boldsymbol{B}^{(2)}$ and $\kappa_\pm = \frac{1}{2}(\kappa \pm \lambda)$. The synchronization transition, at which fluctuations of $\boldsymbol{B}^{(-)}$ are suppressed, occurs when $K < 0$ and hence $\kappa_- > \kappa_+$.

Confinement transitions from the Coulomb phase, such as the synchronization

and columnar-ordering transitions, can be described by introducing 'matter' fields to enforce the restriction to discrete values [15,119]. Condensation of these fields then leads, by the Higgs mechanism, to suppression of magnetic-field fluctuations. The structure of the critical theory is determined by considering representations of the projective symmetry group (PSG) [120] under which the matter fields transform.

In the case of the columnar-ordering transition in the single dimer model, the critical theory is [15,113,114]

$$\mathcal{L}_{\text{SDM,crit.}} = \mathcal{L}_{\text{SDM}} + |(\boldsymbol{\nabla} - \mathrm{i}\boldsymbol{A})\boldsymbol{z}|^2 + s|\boldsymbol{z}|^2 + u|\boldsymbol{z}|^4 \,, \tag{5.3}$$

where $s$ and $u$ are real parameters and $\boldsymbol{z}$ is a two-component complex vector (which is said to be 'minimally coupled' to $\boldsymbol{A}$). The PSG analysis shows that the field $\boldsymbol{z}$ transforms as a spinor under real-space rotations and allows one to express the magnetization as $\boldsymbol{M} \sim \boldsymbol{z}^\dagger \boldsymbol{\sigma} \boldsymbol{z}$. In this description, the ordering transition occurs when $s$ is reduced below its critical value and $\boldsymbol{z}$ condenses, giving a nonzero magnetization and also suppressing fluctuations of the magnetic field via the Higgs mechanism.

In the double dimer model, the matter field should couple identically to both replicas. We therefore expect the critical properties at the columnar-ordering transition in the double dimer model to be the same as in the single-replica case. While some theoretical aspects of this transition remain unresolved [121], its properties have been well characterized numerically [11,115,116].

To describe the synchronization transition, one must similarly include a matter field $\varphi$ whose role is to restrict $B^{(-)}_{\boldsymbol{r},\mu}$ to $\pm 1$ or 0. Because these values are integers, the PSG is trivial in this case[3], and so the result is a scalar Higgs theory,

$$\mathcal{L}_{\text{DDM,crit.}} = \mathcal{L}_{\text{DDM}} + |(\boldsymbol{\nabla} - \mathrm{i}\boldsymbol{A}^{(-)})\varphi|^2 + s_-|\varphi|^2 + u_-|\varphi|^4 \,, \tag{5.4}$$

where $\boldsymbol{B}^{(-)} = \boldsymbol{\nabla} \times \boldsymbol{A}^{(-)}$. We have not included a field coupling to $\boldsymbol{B}^{(+)}$, which would remain noncritical across the synchronization transition.

[3] In the notation of Ref. [15], the background flux is zero, and so the static gauge configuration $\bar{\alpha}$ vanishes.

In 3D, the scalar Higgs theory has a continuous transition in the XY universality class but with an inverted temperature axis [110]. (A more direct route to the same critical theory starts from the loop picture and uses the standard mapping from integer loops to the XY model [109].) We therefore expect the synchronization transition to belong to the inverted-XY universality class.

## 5.3 Numerical results

We have used the worm algorithm to find the phase diagram shown in Fig. 5.2, and to determine the critical properties of each transition. In this section, we present our results for each of the phase boundaries in turn, and also for the nature of the ordered phases at large negative $J/T$.

### 5.3.1 Synchronized $\longleftrightarrow$ Coulomb

We first focus on the synchronization transition, between the synchronized and Coulomb phases. In particular, we consider the case $J = 0$, $K = -1$, and vary the temperature.

Our data for the flux difference variance $\mathrm{Var}\,\mathbf{\Phi}^{(-)}$ and normalized confinement length $\xi/L$ are shown in Fig. 5.4. Both quantities are small (large) at low (high) temperatures, indicating a phase transition between synchronized and Coulomb phases (see Sec. 5.2.2). In particular, the high-temperature limit $\xi^2/L^2 \simeq 0.25$ is observed, which closely matches the mean-square separation of $(L^2+2)/4$ for free monomers hopping on an empty lattice [15]. This is evidence for deconfined monomers in the Coulomb phase.

In contrast to $\mathrm{Var}\,\mathbf{\Phi}^{(-)}$, the variance of the total flux, $\mathrm{Var}\,\mathbf{\Phi}^{(+)}$, is large in both phases, as shown in Fig. 5.5. This confirms that the dimers in each replica remain disordered, even though relative fluctuations between the two replicas are suppressed. In fact, as $|K|/T$ increases and the replicas become more synchronized, $\mathrm{Var}\,\mathbf{\Phi}^{(+)}$ becomes larger. In the limit of perfect synchronization, $K/T = -\infty$, $\mathbf{\Phi}^{(1)} = \mathbf{\Phi}^{(2)}$ and so $\mathrm{Var}\,\mathbf{\Phi}^{(+)} = 4\,\mathrm{Var}\,\mathbf{\Phi}^{(1)}$, double the value at $K = 0$, where $\mathbf{\Phi}^{(1,2)}$ are independent and their variances add.

In order to classify the phase transition, we use finite-size scaling arguments

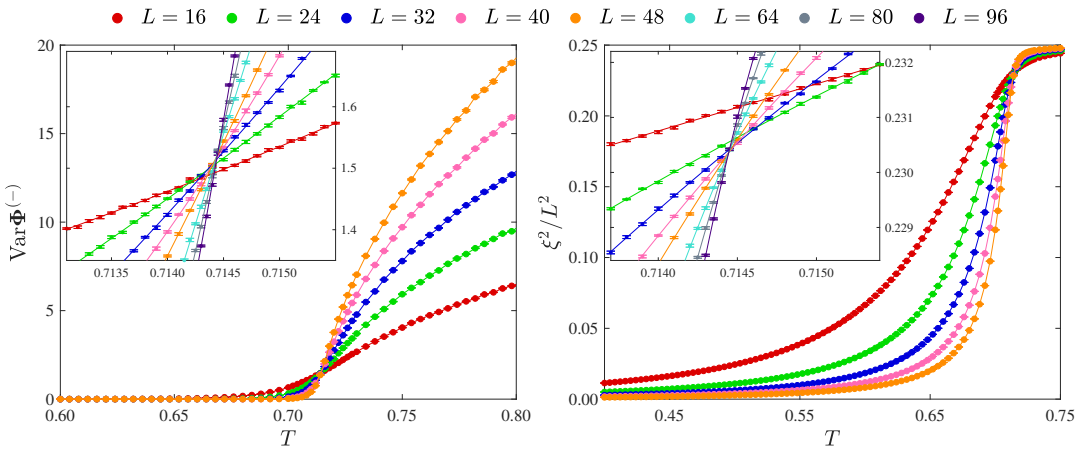


Figure 5.4: Variance of the flux difference $\mathbf{\Phi}^{(-)} = \mathbf{\Phi}^{(1)} - \mathbf{\Phi}^{(2)}$ (left panel) and square of the normalized confinement length $\xi^2/L^2$ (right panel) versus temperature $T$, for the cubic-lattice double dimer model with $J = 0$, $K = -1$, and different system sizes $L$. In each case, quadratic fits in the vicinity of the crossing point are shown (insets). Both quantities are small (large) at low (high) temperatures, indicating a phase transition between synchronized and Coulomb phases. The distinct crossing points imply that the transition is continuous.

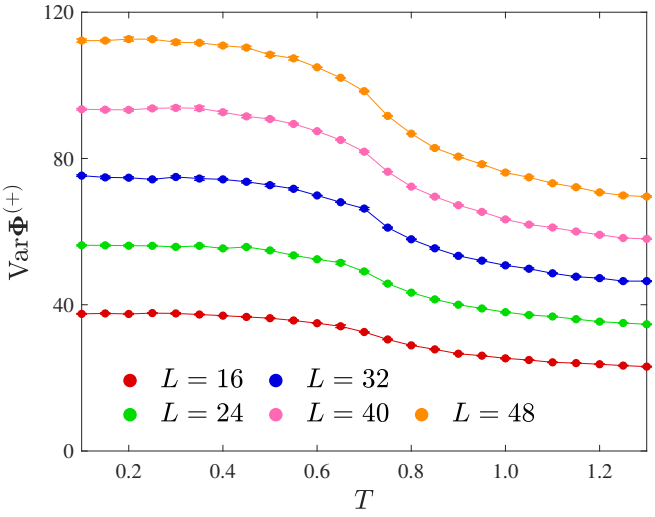


Figure 5.5: Variance of the total flux $\mathbf{\Phi}^{(+)} = \mathbf{\Phi}^{(1)} + \mathbf{\Phi}^{(2)}$ versus temperature $T$, for $J = 0$, $K = -1$, and different system sizes $L$. At low temperatures the replicas are synchronized, but remain fluctuating, and hence Var $\mathbf{\Phi}^{(+)}$ is still large ($\sim L$).

[47]. At the transition of interest, both $\mathrm{Var}\,\boldsymbol{\Phi}^{(-)}$ and $\xi^2/L^2$ have zero scaling dimension [11, 112], and so for a continuous transition at critical temperature $T_\mathrm{c}$, obey the scaling forms

$$\mathrm{Var}\,\boldsymbol{\Phi}^{(-)} \sim f_\Phi(L^{1/\nu}t) \tag{5.5}$$

and

$$\xi^2/L^2 \sim f_\xi(L^{1/\nu}t)\,, \tag{5.6}$$

where $t = (T - T_\mathrm{c})/T_\mathrm{c}$ is the reduced temperature, $\nu$ is the correlation-length exponent, and $f_\Phi$ and $f_\xi$ are universal functions. At the critical temperature $t = 0$, Eqs. (5.5) and (5.6) become independent of system size, predicting a distinct crossing point in MC data at $T = T_\mathrm{c}$. This is observed (see Fig. 5.4, insets), indicating that the transition is continuous.

In reality, we observe a weak dependence on system size at the critical point, which may be explained by corrections to scaling. Including the leading-order correction, Eq. (5.5) becomes

$$\mathrm{Var}\,\boldsymbol{\Phi}^{(-)} \sim f_\Phi(L^{1/\nu}t) + uL^{-|y_u|}\tilde{f}_\Phi(L^{1/\nu}t)\,, \tag{5.7}$$

where $u$ is a constant, $-|y_u|$ is the RG eigenvalue of the leading irrelevant scaling operator, and $\tilde{f}_\Phi$ is a universal function. For two system sizes $L_1$ and $L_2$, this implies a crossing temperature $T_\times$ scaling as [122, 123]

$$T_\times(L_1, L_2) - T_\mathrm{c} \sim \frac{L_2^{-|y_u|} - L_1^{-|y_u|}}{L_1^{1/\nu} - L_2^{1/\nu}}\,. \tag{5.8}$$

Fixing the ratio $\rho = L_2/L_1$ gives

$$T_\times(L_1, \rho L_1) - T_\mathrm{c} \sim L_1^{-|y_u|-1/\nu}\,, \tag{5.9}$$

with an identical result applying to the $\xi^2/L^2$ crossing point. We determine $T_\mathrm{c}$ by fitting to these expressions with $\rho = 2$, using quadratic fits in the vicinity of the crossing point to measure $T_\times$ for each $L_1$ (insets of Fig. 5.4). From our results, shown in Fig. 5.6, we obtain consistent critical temperatures $T_\mathrm{c} = 0.71447(4)$ (flux) and $T_\mathrm{c} = 0.714444(2)$ (confinement length).

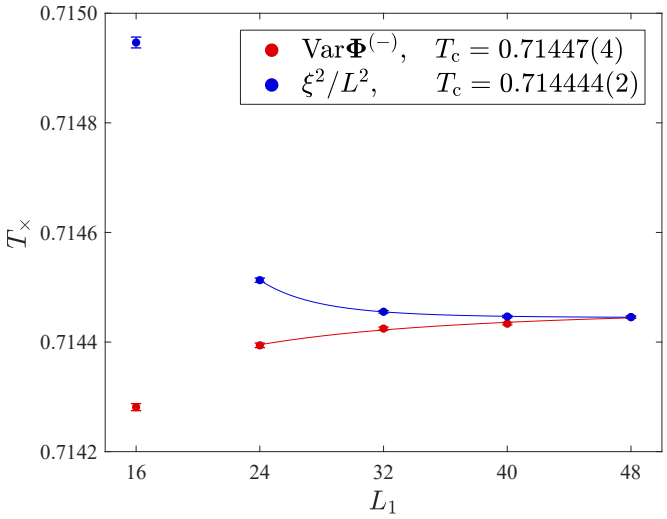


Figure 5.6: Crossing temperature $T_\times$ of Var $\mathbf{\Phi}^{(-)}$ (red) and $\xi^2/L^2$ (blue), for pairs of system sizes $L_1, L_2$ in the ratio $L_2/L_1 = 2$. Solid lines are fits to Eq. (5.9) for $L_1 \geq 24$, from which consistent values for the critical temperature $T_c = 0.71447(4)$ (flux) and $T_c = 0.714444(2)$ (confinement length) are obtained.

In order to determine the correlation length exponent $\nu$, we evaluate the temperature derivative of Eqs. (5.5) and (5.6) at the critical point. For Var $\mathbf{\Phi}^{(-)}$ this gives

$$\frac{\partial}{\partial T} \text{Var } \mathbf{\Phi}^{(-)} \Big|_{T=T_c} \sim L^{1/\nu}, \tag{5.10}$$

and one finds the same result for $\xi^2/L^2$. The system size dependence of the slope at $T_c$ is extracted from quadratic fits. The results are shown in Fig. 5.7, and a fit to Eq. (5.10) yields consistent estimates $\nu = 0.671(8)$ (flux) and $\nu = 0.677(3)$ (confinement length). These values are compatible with the 3D XY universality class, for which $\nu_{3DXY} = 0.6717(1)$ [124].

Now equipped with estimates for $T_c$ and $\nu$, we replot the data of Fig. 5.4 against $L^{1/\nu}t$ in Fig. 5.8. Near the critical temperature, a good data collapse is obtained for all but the smallest system size. The curves, which represent the universal functions $f_\Phi$ and $f_\xi$, are consistent (up to normalization) with those in Fig. 6 of Ref. [15].

As shown in Fig. 5.9 (left panel), a single peak in the heat capacity per site $c$ is observed at the transition temperature, indicating a single phase transition between the synchronized and Coulomb phases. To measure the specific heat

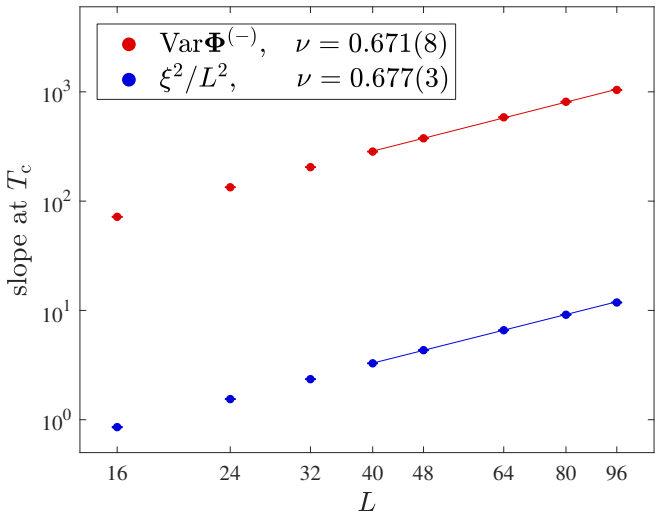


Figure 5.7: Log–log plot of temperature derivative of Var $\mathbf{\Phi}^{(-)}$ (red) and $\xi^2/L^2$ (blue), evaluated at the critical temperature $T_c$, versus system size $L$. Solid lines are fits to Eq. (5.10) for $L \geq 40$, from which consistent values for the correlation length exponent $\nu = 0.671(8)$ (flux) and $\nu = 0.677(3)$ (confinement length) are obtained.

exponent $\alpha$, we consider its scaling at the critical point,

$$c = c_0 + AL^{\alpha/\nu}, \tag{5.11}$$

where $c_0$ represents the regular part, and $A$ is a constant. A fit to this form in Fig. 5.9 (bottom right panel) yields $\alpha/\nu = 0.13(11)$, and using $\nu = 0.677(3)$ (flux) gives a rough estimate $\alpha = 0.09(7)$. In the 3D XY universality class, the corresponding value is $\alpha_{\mathrm{3DXY}} = -0.0151(3)$ [124]. Our results satisfy hyperscaling $\alpha = 2 - d\nu$.

We next measure the crossover exponent $\phi$, which can be found by considering the monomer distribution function $G_{\mathrm{m}}$ [112]. Each MC simulation can only construct $G_{\mathrm{m}}$ up to an arbitrary multiplicative constant, so we define the ratio

$$G(L) = \frac{G_{\mathrm{m}}(\boldsymbol{R}_{\max}; L)}{G_{\mathrm{m}}(\boldsymbol{R}_{\min}; L)}, \tag{5.12}$$

where $|\boldsymbol{R}_{\max}| \sim L$, $|\boldsymbol{R}_{\min}| = 1$, and the system size dependence of $G_{\mathrm{m}}$ has been shown explicitly. At the critical point, this has scaling form [53]

$$G(L) \sim L^{-2\left(d - \frac{\phi}{\nu}\right)}, \tag{5.13}$$

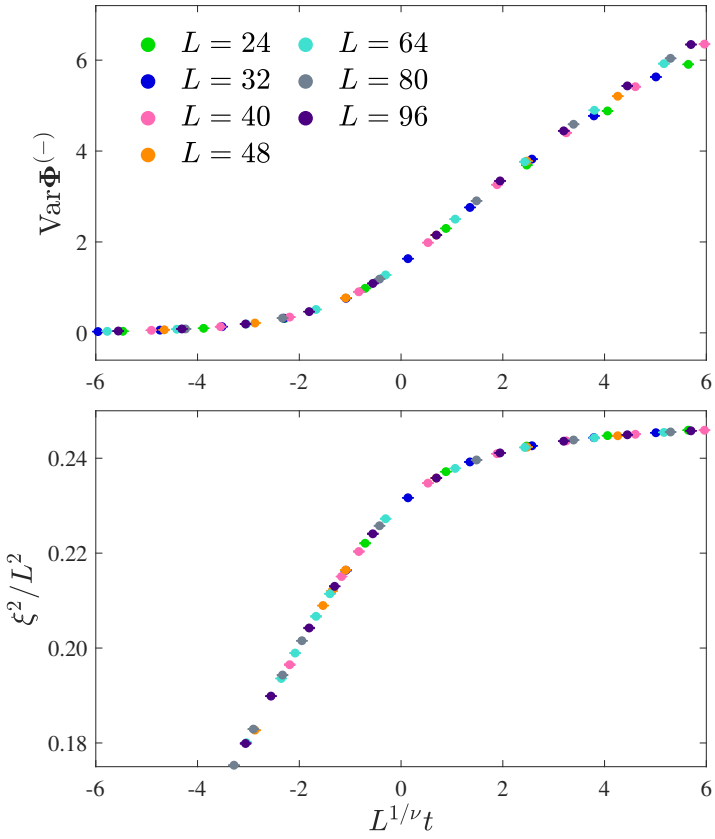


Figure 5.8: Flux difference variance Var $\mathbf{\Phi}^{(-)}$ (top panel) and squared normalized confinement length $\xi^2/L^2$ (bottom panel) versus $L^{1/\nu}t$, for $J = 0$, $K = -1$, and different system sizes $L$. In each case, we have replotted the data of Fig. 5.4 near the critical point, using values $T_c = 0.714444$ (obtained from the crossing point of the confinement length) and $\nu = \nu_{3\mathrm{DXY}} = 0.6717$. The data collapse is consistent with a synchronization transition in the 3D XY universality class.

for sufficiently large systems. A fit to this form in Fig. 5.10 yields $\phi/\nu = 2.4820(6)$, and using $\nu = 0.677(3)$ (confinement length) gives $\phi = 1.680(8)$. This value is compatible with the 3D XY universality class, for which $\phi_{3\mathrm{DXY}} = d\nu_{3\mathrm{DXY}} - \beta_{3\mathrm{DXY}} = 1.6665(3)$, using the exponents reported in Ref. [124].

Finally, we consider the same phase boundary, between the synchronized and Coulomb phases, at points where $J \neq 0$. The critical point $(K/T)_c$ for each $J/T$, plotted in Fig. 5.2, has been obtained from the crossing point of Var $\mathbf{\Phi}^{(-)}$ for system sizes $L = 16$ and $L = 24$. We expect that the universality class is the same for each point along the boundary, and have confirmed this for the points $J/T = -0.16$ and $J/T = -0.24$.

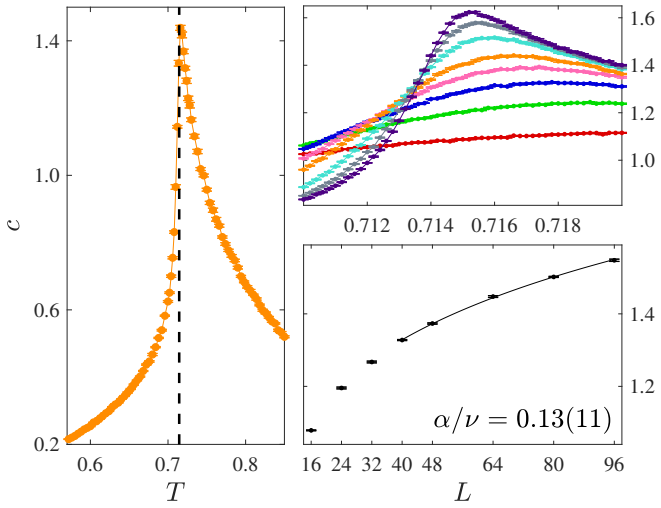


Figure 5.9: Left panel: heat capacity per site $c$ versus temperature $T$ for $J = 0$, $K = -1$, and system size $L = 48$. A single peak is observed at the critical temperature $T_c = 0.714444$ (dashed vertical line), which grows slowly with system size (top right panel). (Colors indicate different values of $L$ as in Fig. 5.4.) Bottom right panel: System size dependence at the critical temperature $T_c = 0.714444$. The solid line is a fit to Eq. (5.11) for $L \geq 40$, from which a value $\alpha/\nu = 0.13(11)$ is obtained.

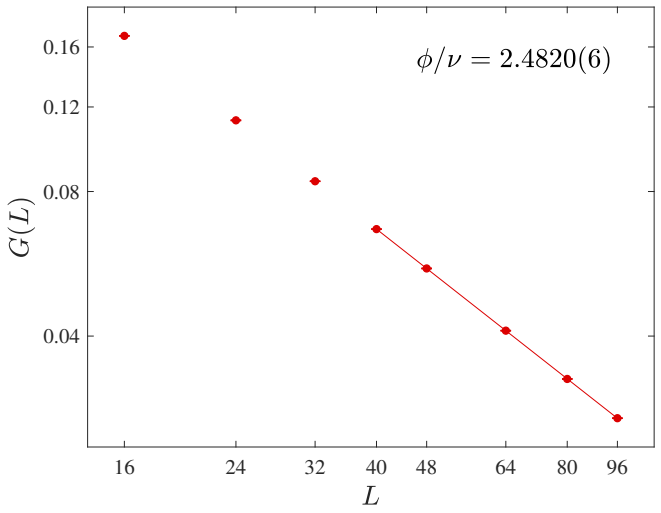


Figure 5.10: Log–log plot of $G(L)$, the normalized value of the monomer distribution function $G_m$, evaluated at the critical temperature $T_c = 0.714444$, versus system size $L$. The solid line is a fit to Eq. (5.13) for $L \geq 40$, from which a value $\phi/\nu = 2.4820(6)$ is obtained.

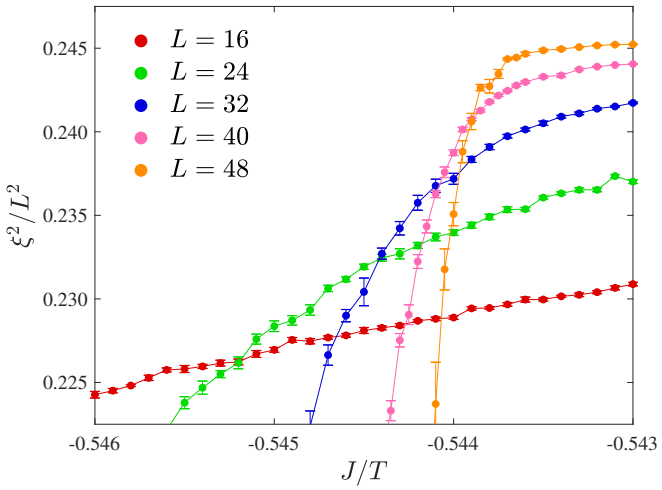


Figure 5.11: Squared normalized confinement length $\xi^2/L^2$ versus $J/T$, for $K/T = -0.2$, $J/T \simeq (J/T)_c$, and different system sizes $L$. A confinement transition between the columnar & synchronized and Coulomb phases is not accompanied by a distinct crossing point, and is thus not continuous.

### 5.3.2 Columnar & (Anti)synchronized $\longleftrightarrow$ Coulomb

As discussed in Sec. 5.2.2, independent replicas ($K = 0$) exhibit a continuous transition between the columnar and Coulomb phases [11]. We now consider columnar ordering of coupled replicas ($K \neq 0$), i.e., the transition between the columnar & (anti)synchronized and Coulomb phases. Our results indicate that columnar ordering is driven first-order when replicas are coupled. (Certain other additional interactions have previously been shown to have this effect [115, 116].)

According to Eq. (5.6), a continuous (confinement) transition is characterized by a crossing point in $\xi^2/L^2$, at the critical temperature. We plot this quantity in Fig. 5.11, in the vicinity of a transition between the columnar & synchronized and Coulomb phases. A distinct crossing point is not observed [cf. Fig. 5.4 (insets)], and hence the transition is not continuous. Similar behaviour is obtained for Var $\mathbf{\Phi}^{(\pm)}$.

Instead, the transition must be first-order. One thus expects a bimodal energy histogram in the vicinity of the critical point, which can be seen in Fig. 5.12 (red). The same behavior is also obtained for transitions between the columnar & antisynchronized and Coulomb phases (blue). In contrast, a single peak is observed for columnar ordering of independent replicas (green), as expected for a continuous transition.

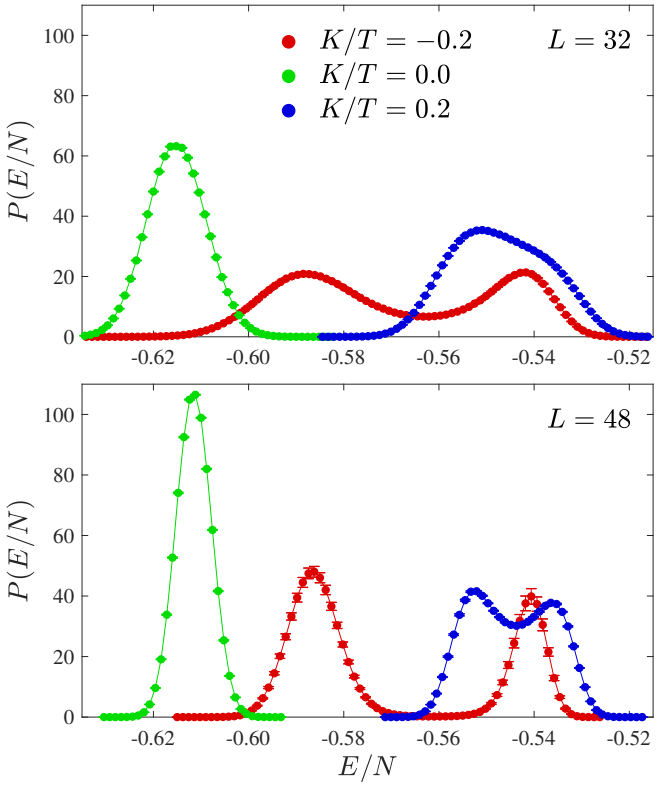


Figure 5.12: Histograms of energy per site, $E/N$, for different values of $K/T$ and with $J/T$ close to the columnar-ordering transition for each. The system sizes shown are $L = 32$ (top panel) and $L = 48$ (bottom panel). A single peak at $K/T = 0$ is consistent with the well-known continuous transition between columnar and Coulomb phases. The distributions for $K/T \neq 0$ are mixtures of two approximately normal distributions, and become more clearly bimodal for larger $L$, indicating first-order transitions between columnar & (anti)synchronized and Coulomb phases.

Six points along this first-order phase boundary are included in the phase diagram of Fig. 5.2. These have been located by identifying peaks in the heat capacity per site, using system size $L = 32$.

### 5.3.3 Columnar & Synchronized $\longleftrightarrow$ Synchronized

We next consider the transition between the columnar & synchronized and synchronized phases. In the limit $K/T \to -\infty$, this phase boundary corresponds to columnar ordering of a single dimer model with $J_{\text{eff}} = 2J$ (see Sec. 5.2.2). This is known to be an (apparently) continuous transition in the tricritical universality class, and we expect the whole phase boundary to share the same critical properties as this point.

Since the flux difference variance Var $\mathbf{\Phi}^{(-)}$ and confinement length $\xi$ are small in both (synchronized) phases, we locate the phase boundary using crossing points in the total flux variance Var $\mathbf{\Phi}^{(+)}$, for system sizes $L = 16$ and $L = 24$. We have analyzed the points $K/T = -2.0$ and $K/T = -1.2$ in greater detail (not shown), and verified the expected critical properties.

### 5.3.4 Columnar & (Anti)synchronized phases

Finally, we consider the different possible columnar-ordered phases at negative $J/T$ and both signs of $K/T$. To classify these, it is convenient to use the covariance of the replica magnetizations $\sigma_{12} = \langle \boldsymbol{M}^{(1)} \cdot \boldsymbol{M}^{(2)} \rangle$, which, deep within the columnar-ordered region, indicates the relative orientations of the magnetizations.

In the columnar phase at $K = 0$, the two replicas are independent, and so $\sigma_{12} = \langle \boldsymbol{M}^{(1)} \rangle \cdot \langle \boldsymbol{M}^{(2)} \rangle = 0$, since the mean magnetization vanishes by symmetry. Deep within the columnar & synchronized phase for $K < 0$, the 6 ground states with $\boldsymbol{M}^{(1)} = \boldsymbol{M}^{(2)} = \pm\boldsymbol{\delta}_\mu$ [see Fig. 5.3(a)] dominate, giving $\sigma_{12} = 1$.

For positive $K$, there are two sets of configurations that minimize the energy: 6 where the magnetizations are antiparallel, $\boldsymbol{M}^{(1)} = -\boldsymbol{M}^{(2)} = \pm\boldsymbol{\delta}_\mu$ [see Fig. 5.3(b)], and $6 \times 4 = 24$ where they are perpendicular, $\boldsymbol{M}^{(1)} \cdot \boldsymbol{M}^{(2)} = 0$ [see Fig. 5.3(c)]. Because the degeneracy between the two sets is accidental (i.e., not required by symmetry), it is liable to be resolved by order by disorder (ObD). There are, *a priori*, three possibilities: ObD favoring antiparallel magnetizations; ObD favoring perpendicular magnetizations; and no ObD, leaving all orientations equally likely. For large negative $J/T$, where columnar order is well established and so $\langle |\boldsymbol{M}^{(\alpha)}| \rangle \simeq 1$, these give limiting values of

$$\sigma_{12} = \begin{cases} -1 & \text{ObD, antiparallel} \\ 0 & \text{ObD, perpendicular} \\ -0.2 & \text{no ObD.} \end{cases} \tag{5.14}$$

MC results for $\sigma_{12}$ are shown in Fig. 5.13. The expected behaviour is obtained in the columnar phase ($\sigma_{12} = 0$ when $K/T = 0$), and the columnar & synchronized phase ($\sigma_{12} \to 1$ for $K/T < 0$). In the columnar & antisynchronized phase, the

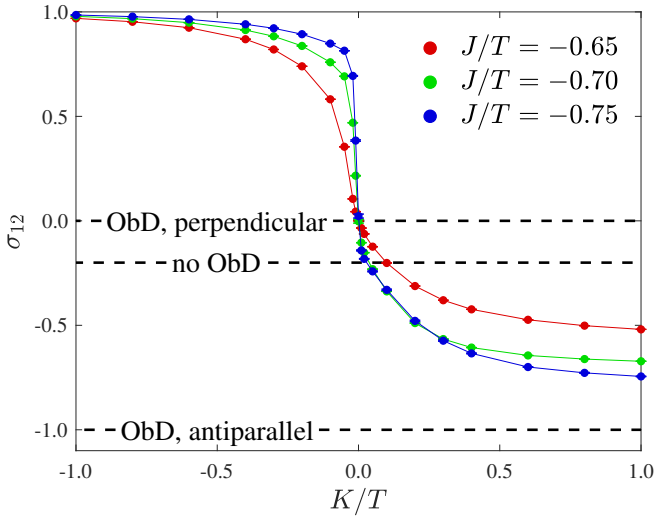


Figure 5.13: Covariance of the replica magnetizations $\sigma_{12} = \langle \boldsymbol{M}^{(1)} \cdot \boldsymbol{M}^{(2)} \rangle$ versus $K/T$, for different values of $J/T < 0$ and system size $L = 8$. As explained in Sec. 5.3.4, $\sigma_{12}$ vanishes at $K = 0$ and approaches $+1$ in the columnar & synchronized phase for $K/T < 0$. Deep within the columnar & antisynchronized phase, $K/T > 0$, we expect $\sigma_{12}$ to approach one of the values in Eq. (5.14), shown with dashed lines, depending on the result of order-by-disorder effects. The evidence indicates that antiparallel magnetizations $\boldsymbol{M}^{(1)} = -\boldsymbol{M}^{(2)}$ are preferred. (Accessible values of $L$ and $|J|/T$ are limited by loss of ergodicity deep within the ordered phase.)

data appear to converge towards $\sigma_{12} = -1$ as $J/T$ becomes more negative. This indicates that ObD selects an arrangement with antiparallel magnetizations, in agreement with consideration of the elementary fluctuations, as in Sec. 5.2.2.

## 5.4 Bethe lattice

To gain further insight into the synchronization transition, we consider the double dimer model on the Bethe lattice, which, we will show, can be solved exactly. This provides an approximation to the model on the cubic lattice that is in the spirit of mean-field theory. In particular, we expect it to reproduce the qualitative behavior correctly, with a critical temperature that approximates the true value, but to fail to predict the critical properties.

We first consider a 'Cayley tree', illustrated in Fig. 5.14, a graph where each vertex has $q$ neighbors, except for those at the boundaries, and where there are no closed loops. To avoid contributions from the boundaries, which in the

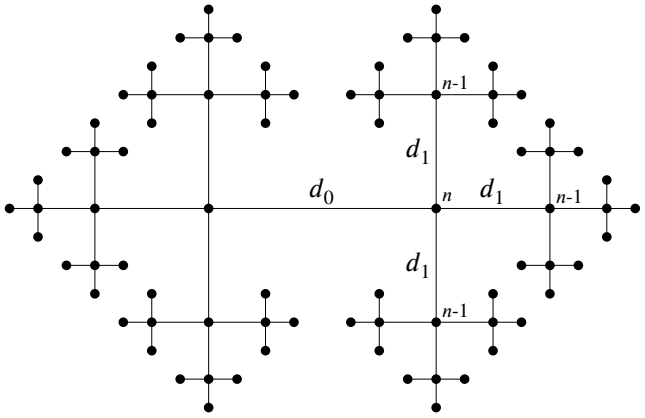


Figure 5.14: Cayley tree with coordination number $q = 4$. The 'root' bond, labeled $d_0$, has depth $n$ and is connected at each of its vertices to $q-1$ 'subbranches', with roots labeled $d_1$, of depth $n - 1$.

thermodynamic limit constitute a finite fraction of the vertices, we define the Bethe lattice as the part of the Cayley tree that is far away from all boundaries. A dimer model on the Bethe lattice has dimers occupying the bonds of the lattice (i.e., the edges of the graph).

Statistical mechanics problems with nearest-neighbour interactions are often exactly solvable on the Bethe lattice, since the absence of circuits allows one to formulate a recurrence relation for the partition function. This method has been used for the Ising model [61], whilst a similar calculation has been performed for spin ice on the Husimi tree [14,112,125]. Here we apply it to the synchronization transition on the Bethe lattice.

### 5.4.1 Noninteracting dimers

To illustrate the method, we begin with a simpler calculation. Consider a single close-packed dimer model, with no interactions, on the Cayley tree. In this case the partition function is simply

$$Z = \sum_{c \in \mathfrak{C}_0} 1 \,. \tag{5.15}$$

A quantity of interest is the mean dimer occupation number for the central bond, or root, of the Cayley tree, given by

$$\langle d_0 \rangle = \frac{1}{Z} \sum_{c \in \mathfrak{C}_0} d_0 \,. \tag{5.16}$$

To begin, the partition function is written as

$$Z = \sum_{d_0} \left[ Z_n(d_0) \right]^2 \tag{5.17}$$

$$= \left[ Z_n(0) \right]^2 + \left[ Z_n(1) \right]^2 \,. \tag{5.18}$$

In the first line, the quantity $Z_n(d_0)$ is the 'partial partition function' of the left, or equivalently right, branch of the Cayley tree, when the root dimer occupation number is fixed to $d_0$. The index $n$ enumerates the branch depth. The same logic may be applied to Eq. (5.16), and results in

$$\langle d_0 \rangle = \frac{\left[ Z_n(1) \right]^2}{\left[ Z_n(0) \right]^2 + \left[ Z_n(1) \right]^2} \,. \tag{5.19}$$

A branch with root $d_0$ and depth $n$ consists of $(q-1)$ 'subbranches', rooted at $d_1$ and with depth $n-1$ (see Fig. 5.14). This observation allows the construction of recurrence relations which connect the partial partition functions of branches of depth $n$ and $n-1$. By allowing for all consistent configurations of the subbranches, while applying (at the roots) the constraint that each site should be covered by exactly one dimer, one finds

$$Z_n(0) = (q-1) Z_{n-1}(1) \left[ Z_{n-1}(0) \right]^{q-2} \tag{5.20}$$

$$Z_n(1) = \left[ Z_{n-1}(0) \right]^{q-1} \,. \tag{5.21}$$

It is convenient to introduce the variable

$$x_n = \frac{Z_n(0)}{Z_n(1)} \,, \tag{5.22}$$

for which Eqs. (5.20) and (5.21) imply

$$x_n = \frac{q-1}{x_{n-1}}\,. \tag{5.23}$$

Next we consider only sites on the Bethe lattice, deep within the Cayley tree, by taking the thermodynamic limit $n \to \infty$. Here, the solution is a fixed point satisfying $x_n = x_{n-1} = x$, so that Eq. (5.19) may be re-written

$$\langle d_0 \rangle = \frac{1}{1+x^2}\,, \tag{5.24}$$

whilst Eq. (5.23) becomes

$$x = \frac{q-1}{x}\,. \tag{5.25}$$

This has solution

$$x = \sqrt{q-1}\,, \tag{5.26}$$

and substitution into Eq. (5.24) yields

$$\langle d_0 \rangle = \frac{1}{q}\,. \tag{5.27}$$

This is given, as expected, by the ratio of the number of dimers to the number of bonds.

In reality, the recurrence relation of Eq. (5.23) does not converge towards its fixed point in the thermodynamic limit, but instead oscillates indefinitely. To perform a more rigorous treatment, one can permit monomers with a small nonzero fugacity $z$, modifying Eq. (5.23) to

$$x_n = \frac{q-1}{x_{n-1}} + z\,. \tag{5.28}$$

This recurrence relation does converge in the thermodynamic limit, and Eq. (5.27) is easily retrieved by subsequently taking the limit $z \to 0$.

Using the same approach, one can also calculate the response to monomer insertion, which, as discussed in Sec. 5.2.2, allows one to distinguish confined and deconfined phases. The monomer distribution function $G_{\mathrm{m}}$ involves a pair of monomers and cannot easily be calculated using the recurrence relation. Instead,

we consider the corresponding quantity for a single monomer,

$$\Psi_{\mathrm{m}} = \frac{Z_{\mathrm{m}}}{Z}\,, \tag{5.29}$$

where $Z_{\mathrm{m}} = \sum_{c\in\mathfrak{C}(\boldsymbol{r}_+)} \mathrm{e}^{-E/T}$ is the partition function with a monomer inserted at $\boldsymbol{r}_+$. This takes the form of an expectation value (specifically, of a monomer insertion operator [121]) and we therefore refer to it as the 'monomer expectation value'. While it vanishes due to the requirement of charge neutrality when PBCs are applied, it can be nonzero with open boundary conditions, including on the Bethe lattice.

Suppose $\boldsymbol{r}_+$ is taken as the left side of the root $d_0$. Then the left (right) branch of the Cayley tree 'sees' an occupied (unoccupied) root, and the system has partition function $Z_{\mathrm{m}} = Z_n(1)Z_n(0)$. The partition function without monomers $Z$ is again given by Eq. (5.18). From the definition of Eq. (5.22), and its solution in Eq. (5.26), one obtains

$$\Psi_{\mathrm{m}} = \frac{\sqrt{q-1}}{q}. \tag{5.30}$$

The result is nonzero, indicating that an isolated monomer can occur with finite free-energy cost $\Delta F_{\mathrm{m}} = -T\ln\Psi_{\mathrm{m}}$. Monomers are therefore deconfined, as expected in the noninteracting dimer model.

### 5.4.2 Synchronization transition

Now consider the double dimer model of Eq. (2.2) on the Cayley tree. Since parallel pairs of dimers cannot be defined, we set $J = 0$, leaving configuration energies

$$E = K\sum_l d_l^{(1)} d_l^{(2)}\,, \tag{5.31}$$

and a partition function given by Eq. (2.3). The quantity of interest is the mean energy per site deep within the interior of the tree, which we take as its value on the root bond,

$$\frac{\langle E\rangle}{N} = \frac{q}{2}K\langle d_0^{(1)} d_0^{(2)}\rangle\,, \tag{5.32}$$

assuming translational symmetry (at least on average). We therefore require the correlation function

$$\langle d_0^{(1)} d_0^{(2)} \rangle = \frac{1}{Z} \sum_{\substack{c^{(1)} \in \mathfrak{C}_0 \\ c^{(2)} \in \mathfrak{C}_0}} d_0^{(1)} d_0^{(2)} \mathrm{e}^{-E/T} \tag{5.33}$$

on the same bond. This may be calculated in analogy with Sec. 5.4.1, although the algebra is more involved.

The partition function is written as

$$Z = \sum_{d_0^{(1)}, d_0^{(2)}} \mathrm{e}^{-k d_0^{(1)} d_0^{(2)}} \left[ Z_n \left( d_0^{(1)}, d_0^{(2)} \right) \right]^2 \tag{5.34}$$

$$= \left[ Z_n(0,0) \right]^2 + \left[ Z_n(1,0) \right]^2 + \left[ Z_n(0,1) \right]^2 + \mathrm{e}^{-k} \left[ Z_n(1,1) \right]^2 , \tag{5.35}$$

where the reduced coupling $k = K/T$ has been introduced for convenience. In the first line, the quantity $Z_n \left( d_0^{(1)}, d_0^{(2)} \right)$ is the 'partial partition function' of the left, or equivalently right, branch of the Cayley tree, when the root dimer occupation numbers are fixed to $d_0^{(1)}$ and $d_0^{(2)}$. Similarly, Eq. (5.33) may be written

$$\langle d_0^{(1)} d_0^{(2)} \rangle = \frac{\mathrm{e}^{-k} \left[ Z_n(1,1) \right]^2}{\left[ Z_n(0,0) \right]^2 + \left[ Z_n(1,0) \right]^2 + \left[ Z_n(0,1) \right]^2 + \mathrm{e}^{-k} \left[ Z_n(1,1) \right]^2} . \tag{5.36}$$

In order to construct recurrence relations, one must again allow for all possible configurations of the subbranches, while applying (at the roots) the constraint that each site should be covered by exactly one dimer in each replica. The results are

$$\begin{aligned} Z_n(0,0) = (q-1)\mathrm{e}^{-k} Z_{n-1}(1,1) \left[ Z_{n-1}(0,0) \right]^{q-2} + \\ (q-1)(q-2) Z_{n-1}(1,0) Z_{n-1}(0,1) \left[ Z_{n-1}(0,0) \right]^{q-3} \end{aligned} \tag{5.37}$$

$$Z_n(1,0) = (q-1) Z_{n-1}(0,1) \left[ Z_{n-1}(0,0) \right]^{q-2} \tag{5.38}$$

$$Z_n(0,1) = (q-1) Z_{n-1}(1,0) \left[ Z_{n-1}(0,0) \right]^{q-2} \tag{5.39}$$

$$Z_n(1,1) = \left[ Z_{n-1}(0,0) \right]^{q-1} . \tag{5.40}$$

Next we define the variables

$$\begin{pmatrix} u_n \\ v_n \\ w_n \end{pmatrix} = \frac{1}{Z_n(1,1)} \begin{pmatrix} Z_n(0,0) \\ Z_n(1,0) \\ Z_n(0,1) \end{pmatrix} \tag{5.41}$$

and take the thermodynamic limit. The solutions are again fixed points, and Eq. (5.36) may be rewritten

$$\langle d_0^{(1)} d_0^{(2)} \rangle = \frac{\mathrm{e}^{-k}}{u^2 + v^2 + w^2 + \mathrm{e}^{-k}} \,, \tag{5.42}$$

whilst Eqs. (5.37)–(5.40) translate into a system of coupled, nonlinear equations given by

$$u = \frac{q-1}{u} \left[ \mathrm{e}^{-k} + (q-2) \frac{vw}{u} \right] \tag{5.43}$$

$$v = (q-1) \frac{w}{u} \tag{5.44}$$

$$w = (q-1) \frac{v}{u} \,. \tag{5.45}$$

The solutions to this system depend on the value of the reduced coupling $k$. For $k \leq k_\mathrm{c} = -\log(q-1)$, there is a single solution

$$\begin{pmatrix} u \\ v \\ w \end{pmatrix} = \begin{pmatrix} \sqrt{(q-1)\mathrm{e}^{-k}} \\ 0 \\ 0 \end{pmatrix} \,, \tag{5.46}$$

whereas, for $k > k_\mathrm{c}$, we find additionally

$$\begin{pmatrix} u \\ v \\ w \end{pmatrix} = \begin{pmatrix} q-1 \\ \sqrt{\frac{q-1}{q-2}(q-1-\mathrm{e}^{-k})} \\ \sqrt{\frac{q-1}{q-2}(q-1-\mathrm{e}^{-k})} \end{pmatrix} \,, \tag{5.47}$$

which, as we have confirmed by a linear stability analysis, is the only stable solution. (Note that the critical value $k_\mathrm{c}$ is negative – as expected, the transition occurs for attractive coupling $K < 0$.)

Substitution of this result into Eq. (5.42), and then into Eq. (5.32), yields the

final result for the mean energy per site of

$$\frac{\langle E\rangle}{N} = \begin{cases} \dfrac{K}{2}\dfrac{(q-2)\mathrm{e}^{-k}}{(q-1)^2-\mathrm{e}^{-k}} & \text{for } k \geq k_\mathrm{c} \\ \dfrac{K}{2} & k \leq k_\mathrm{c}. \end{cases} \tag{5.48}$$

In line with $x_n$ in Sec. 5.4.1, the recurrence relations for $u_n$, $v_n$ and $w_n$ derivable from Eqs. (5.37)–(5.40) may oscillate in the thermodynamic limit. Again, convergence is achieved by allowing monomers with fugacity $z$ and taking the limit $z \to 0$.

In Fig. 5.15 (top panel) we show the temperature dependence of the mean energy per site for a Bethe lattice with the same coordination number as the cubic lattice, $q = 6$, and with $K = -1$. There is a second-order phase transition at $T_\mathrm{c} = 1/\log(5) \simeq 0.62$, characterized by a kink in the mean energy per site. Note that on the cubic lattice, our corresponding result (with $J = 0$) is $T_\mathrm{c} \simeq 0.71$. The low-temperature phase is always perfectly synchronized, since there is an energy $K$ for every dimer in a given replica. The high-temperature phase, which we identify with the Coulomb phase, is unsynchronized. In particular, when $k = 0$, the mean energy per bond is $K/q^2$. This is sensible, because in this limit the replicas are independent, and from Eq. (5.27) the probability of double bond occupation is $1/q^2$.

To confirm our identification of the high-temperature solution with the (unsynchronized) Coulomb phase, we return to the monomer expectation value $\Psi_\mathrm{m}$ defined in Eq. (5.29). In this case, we consider the partition function with a monomer in a single replica (again on the left side of the root $d_0$), which is

$$Z_\mathrm{m} = Z_n(1,0)Z_n(0,0) + Z_n(1,1)Z_n(0,1)\,, \tag{5.49}$$

while the partition function without monomers $Z$ is given by Eq. (5.35). From the definitions of Eq. (5.41), and their solution in Eqs. (5.46) and (5.47), one obtains

$$\Psi_\mathrm{m} = \begin{cases} \dfrac{\sqrt{(q-1)(q-2)(q-1-\mathrm{e}^{-k})}}{(q-1)^2-\mathrm{e}^{-k}} & \text{for } k \geq k_\mathrm{c} \\ 0 & k \leq k_\mathrm{c}. \end{cases} \tag{5.50}$$

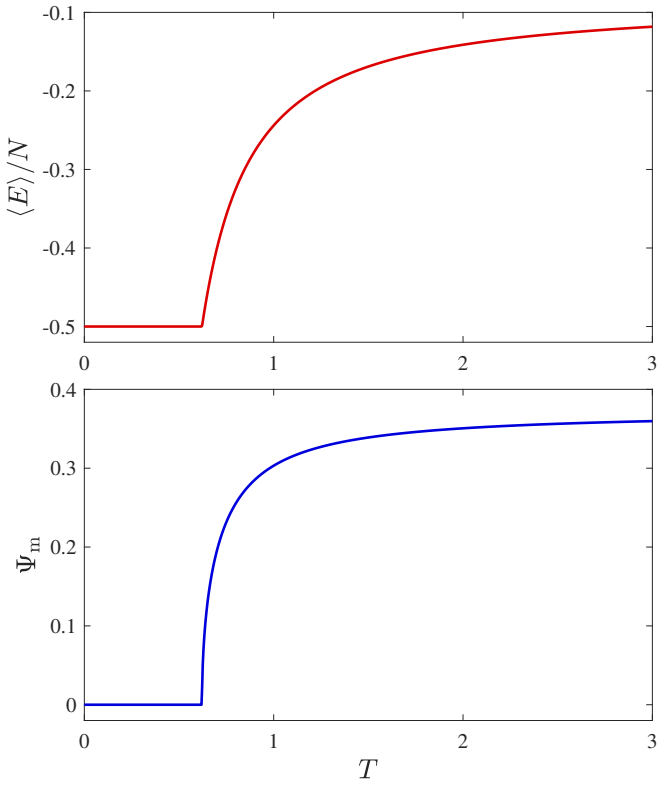


Figure 5.15: Mean energy per site $\langle E \rangle / N$ (top panel) and monomer expectation value $\Psi_{\rm m}$ (bottom panel), versus temperature $T$ for the double dimer model on a Bethe lattice with the same coordination number as the cubic lattice, $q = 6$. In this case, there are no interactions within each replica (i.e., $J = 0$), and we set $K = -1$. A second-order phase transition at $T_{\rm c} = 1/\log(5) \simeq 0.62$ separates a low-temperature (perfectly) synchronized phase, in which monomers are confined ($\Psi_{\rm m} = 0$), from a high-temperature unsynchronized phase, in which monomers are deconfined ($\Psi_{\rm m} > 0$).

The result is shown in Fig. 5.15 (bottom panel), using the same parameters as for the mean energy per site. In the low-temperature synchronized phase ($k < k_{\rm c} < 0$), $\Psi_{\rm m} = 0$ and the free-energy cost for an isolated monomer, $\Delta F_{\rm m} = -T \ln \Psi_{\rm m}$, is infinite, while in the high-temperature unsynchronized phase, $\Psi_{\rm m} > 0$ and $\Delta F_{\rm m}$ is finite. This qualitative distinction, equivalent to the criterion based on $G_{\rm m}$ introduced in Sec. 5.2.2, implies that the synchronization transition on the Bethe lattice is a *bona fide* confinement transition.

While the model on the Bethe lattice with $q = 6$ gives a reasonable approximation to the critical temperature on the cubic lattice, it does not reproduce the correct critical behavior. This is directly evident for the heat capacity, $\frac{\partial}{\partial T}\langle E \rangle$, which, according to Eq. (5.48), has a discontinuity at $T = T_{\rm c}$, as expected for

a mean-field theory. For the monomer expectation value, the duality mapping to the XY model [112] gives $\Psi_{\mathrm{m}} \sim t^{\beta}$ for $t > 0$, where $\beta$ is the magnetization exponent. From Eq. (5.50), we find the mean-field value $\beta = \frac{1}{2}$.

## 5.5 Conclusions

We have studied the phases of the double dimer model on the cubic lattice using a combination of theoretical arguments and MC simulations. As on the square lattice, we find a synchronization transition at a critical coupling between the replicas, which has no local order parameter but can be characterized through the confinement of monomers.

In particular, our detailed finite-size scaling analysis of the synchronization transition yielded critical exponents compatible with the 3D XY universality class, in line with our expectations from both field theory and the loop picture. An exact solution on the Bethe lattice provided a reasonable approximation to the critical temperature, but with mean-field critical exponents.

It is interesting to compare the qualitative phase structure in 2D and 3D. Two notable differences are the absence of direct transitions between the Coulomb and columnar phases for coupled replicas in 2D, as well as the lack of antisynchronized and staggered phases in 3D. Moreover, in the 3D case we have demonstrated that replica coupling renders columnar ordering first order, which has no analog in 2D.

# Chapter 6

# Conclusions

In this thesis, we have studied an interesting example of a non-LGW phase transition in the double dimer model, in both two and three dimensions. In the absence of a local order parameter, we have used the concepts of topological order and confinement to distinguish the two phases. By also including interactions between parallel dimers within each replica, we have seen that this system exhibits a particularly rich phase structure.

In Chapter 2, we focused on the two-dimensional case, namely the square and honeycomb lattices. Here, our symmetry-based analysis of an effective height theory showed that, in both cases, the synchronization transition is BKT type and occurs at zero critical coupling. Considerable attention was also devoted to a MC study of the transition between the Coulomb and staggered phases.

Chapter 3 then commenced an analytical calculation of the phase boundary near the noninteracting point, as measured in Chapter 2. We mapped the square-lattice dimer model to a quantum Hamiltonian in $1 + 1$ dimensions, and diagonalized this to obtain a free-fermion form. As an aside, we were able to use this to reproduce known exact results previously obtained using Pfaffian methods.

The next stage in our calculation of the phase boundary was the subject of Chapter 4. By bosonizing the free-fermion Hamiltonian of Chapter 3, we recovered the Gaussian height theory of Chapter 2, but with known values for the phenomenological parameters. We then constructed and bosonized interaction operators, and used an RG analysis to determine the shape of the phase boundary at linear order in the couplings.

Finally, in Chapter 5 we considered the three-dimensional case, specifically that of the cubic lattice. The main focus here was a finite-size scaling analysis of the MC data, which yielded accurate estimates for the critical temperature and two critical exponents, the latter being consistent with the 3D XY universality class. Furthermore, we solved the double dimer on the Bethe lattice exactly, which provided an approximation in the spirit of mean-field theory.

Extensions of the work in this thesis to dimer models on other bipartite lattices are straightforward. By adapting the synchronization criterion introduced here, analogous transitions can also be expected in other systems consisting of two coupled replicas of a fractionalized phase. These include the Coulomb phase in ice models [5,6], where a pair of monopoles in one replica would similarly become confined upon synchronization.

Experimental realizations of such transitions could be possible in various frustrated systems. In 2D, these include magnetic materials with a bilayer structure (like the bilayer TLIAFM of Sec. 2.3) as well as nanomagnet arrays [126], which have been used to simulate ice models with a variety of geometries, constructed in a double-layer configuration. A 3D synchronization transition could be possible between magnetic moments of two types, for example, in pyrochlore oxides with magnetic ions on both the A and B sites of the crystal structure [127]. In these cases, one expects a thermodynamic phase transition (see, e.g., Fig. 5.9), but with no magnetic ordering. We leave the detailed study of possible experimental signatures to future work.

A natural extension of the system studied here would involve multiple replicas $\alpha \in \{1, 2, \ldots, n\}$. With sufficiently strong coupling between 'adjacent' replicas $\alpha$ and $\alpha + 1$, this could be interpreted as a trajectory either of the classical dimer model imbued with dynamics or the Suzuki–Trotter decomposition of the partition function for a quantum dimer model [128]. The double-loop algorithm introduced in Sec. 2.4.2 could be extended to the case of multiple replicas, giving a method that is similar (at least in spirit) to the membrane algorithm [129] previously applied to quantum ice. Alternatively, coupling one replica to $n$ others and taking the limit $n \to 0$ [47] provides a way to introduce a quenched disorder potential on the links of the single dimer model.

# Bibliography


[1] J. K. Roberts. Some properties of adsorbed films of oxygen on tungsten. *Proceedings of the Royal Society A: Mathematical, Physical and Engineering Sciences*, 152(876):464–477, 1935.

[2] J. K. Roberts and A. R. Miller. The application of statistical methods to immobile adsorbed films. *Mathematical Proceedings of the Cambridge Philosophical Society*, 35(02):293, 1939.

[3] L. Balents. Spin liquids in frustrated magnets. *Nature*, 464(7286):199–208, 2010.

[4] J. T. Chalker. Spin liquids and frustrated magnetism. In C. Chamon, M. Goerbig, R. Moessner, and L. Cugliandolo, editors, *Topological Aspects of Condensed Matter Physics*, volume 103. Oxford University Press, 2017. Lecture notes of the Les Houches Summer School, August 2014.

[5] C. Castelnovo, R. Moessner, and S. L. Sondhi. Spin ice, fractionalization, and topological order. *Annual Review of Condensed Matter Physics*, 3(1):35–55, 2012.

[6] C. L. Henley. The "Coulomb phase" in frustrated systems. *Annual Review of Condensed Matter Physics*, 1(1):179–210, 2010.

[7] Ying Tang, Anders W. Sandvik, and Christopher L. Henley. Properties of resonating-valence-bond spin liquids and critical dimer models. *Phys. Rev. B*, 84:174427, 2011.

[8] David A. Huse, Werner Krauth, R. Moessner, and S. L. Sondhi. Coulomb and liquid dimer models in three dimensions. *Phys. Rev. Lett.*, 91:167004, 2003.

[9] Fabien Alet, Jesper Lykke Jacobsen, Grégoire Misguich, Vincent Pasquier, Frédéric Mila, and Matthias Troyer. Interacting classical dimers on the square lattice. *Phys. Rev. Lett.*, 94:235702, 2005.

[10] Fabien Alet, Yacine Ikhlef, Jesper Lykke Jacobsen, Grégoire Misguich, and Vincent Pasquier. Classical dimers with aligning interactions on the square lattice. *Phys. Rev. E*, 74:041124, 2006.

[11] Fabien Alet, Grégoire Misguich, Vincent Pasquier, Roderich Moessner, and Jesper Lykke Jacobsen. Unconventional continuous phase transition in a three-dimensional dimer model. *Phys. Rev. Lett.*, 97:030403, 2006.

[12] P. W. Kasteleyn. Dimer statistics and phase transitions. *Journal of Mathematical Physics*, 4(2):287–293, 1963.

[13] Somendra M. Bhattacharjee, John F. Nagle, David A. Huse, and Michael E. Fisher. Critical behavior of a three-dimensional dimer model. *Journal of Statistical Physics*, 32(2):361–374, 1983.

[14] L. D. C. Jaubert, J. T. Chalker, P. C. W. Holdsworth, and R. Moessner. Three-dimensional Kasteleyn transition: Spin ice in a [100] field. *Phys. Rev. Lett.*, 100:067207, 2008.

[15] Gang Chen, Jan Gukelberger, Simon Trebst, Fabien Alet, and Leon Balents. Coulomb gas transitions in three-dimensional classical dimer models. *Phys. Rev. B*, 80:045112, 2009.

[16] L. D. Landau and E. M. Lifshitz. *Statistical Physics*. Butterworth-Heinemann, 1980.

[17] Doron L. Bergman, Gregory A. Fiete, and Leon Balents. Ordering in a frustrated pyrochlore antiferromagnet proximate to a spin liquid. *Phys. Rev. B*, 73:134402, 2006.

[18] T. Senthil, Ashvin Vishwanath, Leon Balents, Subir Sachdev, and Matthew P. A. Fisher. Deconfined quantum critical points. *Science*, 303(5663):1490–1494, 2004.

[19] T. Senthil, Leon Balents, Subir Sachdev, Ashvin Vishwanath, and Matthew P. A. Fisher. Quantum criticality beyond the Landau-Ginzburg-Wilson paradigm. *Phys. Rev. B*, 70:144407, 2004.

[20] R. Raghavan, C. L. Henley, and S. L. Arouh. New two-color dimer models with critical ground states. *Journal of Statistical Physics*, 86(3-4):517–550, 1997.

[21] Kedar Damle, Deepak Dhar, and Kabir Ramola. Resonating valence bond wave functions and classical interacting dimer models. *Phys. Rev. Lett.*, 108:247216, 2012.

[22] R. Kenyon. Conformal invariance of loops in the double-dimer model. *Communications in Mathematical Physics*, 326(2):477–497, 2014.

[23] E. H. Lieb. Solution of the dimer problem by the transfer matrix method. *Journal of Mathematical Physics*, 8(12):2339–2341, 1967.

[24] P. W. Kasteleyn. The statistics of dimers on a lattice. *Physica*, 27(12):1209–1225, 1961.

[25] H. N. V. Temperley and M. E. Fisher. Dimer problem in statistical mechanics–an exact result. *Philosophical Magazine*, 6(68):1061–1063, 1961.

[26] Michael E. Fisher. Statistical mechanics of dimers on a plane lattice. *Phys. Rev.*, 124:1664–1672, 1961.

[27] Arthur E. Ferdinand. Statistical mechanics of dimers on a quadratic lattice. *Journal of Mathematical Physics*, 8(12):2332–2339, 1967.

[28] Cédric Boutillier and Béatrice de Tilière. Loop statistics in the toroidal honeycomb dimer model. *Ann. Probab.*, 37(5):1747–1777, 2009.

[29] Michael E. Fisher and John Stephenson. Statistical mechanics of dimers on a plane lattice. II. dimer correlations and monomers. *Phys. Rev.*, 132:1411–1431, 1963.

[30] Jan von Delft and Herbert Schoeller. Bosonization for beginners — refermionization for experts. *Annalen der Physik*, 7(4):225–305, 1998.

[31] H. W. J. Blöte and H. J. Hilhorst. Roughening transitions and the zero-temperature triangular Ising antiferromagnet. *Journal of Physics A: Mathematical and General*, 15(11):L631–L637, 1982.

[32] Chen Zeng and Christopher L. Henley. Zero-temperature phase transitions of an antiferromagnetic Ising model of general spin on a triangular lattice. *Phys. Rev. B*, 55:14935–14947, 1997.

[33] N. D. Mermin and H. Wagner. Absence of ferromagnetism or antiferromagnetism in one- or two-dimensional isotropic Heisenberg models. *Phys. Rev. Lett.*, 17:1133–1136, 1966.

[34] P. C. Hohenberg. Existence of long-range order in one and two dimensions. *Phys. Rev.*, 158:383–386, 1967.

[35] Michael F. Faulkner, Steven T. Bramwell, and Peter C. W. Holdsworth. Topological-sector fluctuations and ergodicity breaking at the Berezinskii–Kosterlitz–Thouless transition. *Phys. Rev. B*, 91:155412, 2015.

[36] Michael E. Fisher, Michael N. Barber, and David Jasnow. Helicity modulus, superfluidity, and scaling in isotropic systems. *Phys. Rev. A*, 8:1111–1124, 1973.

[37] David R. Nelson and J. M. Kosterlitz. Universal jump in the superfluid density of two-dimensional superfluids. *Phys. Rev. Lett.*, 39:1201–1205, 1977.

[38] Claudio Castelnovo, Claudio Chamon, Christopher Mudry, and Pierre Pujol. Zero-temperature Kosterlitz–Thouless transition in a two-dimensional quantum system. *Annals of Physics*, 322(4):903 – 934, 2007.

[39] Hiromi Otsuka. Classical dimer model with anisotropic interactions on the square lattice. *Phys. Rev. E*, 80:011140, 2009.

[40] L. Mathey, A. Polkovnikov, and A. H. Castro Neto. Phase-locking transition of coupled low-dimensional superfluids. *EPL (Europhysics Letters)*, 81(1):10008, 2007.

[41] Giacomo Bighin, Nicolò Defenu, István Nándori, Luca Salasnich, and Andrea Trombettoni. Berezinskii-Kosterlitz-Thouless paired phase in coupled $XY$ models. *Phys. Rev. Lett.*, 123:100601, 2019.

[42] Anders W. Sandvik and R. Moessner. Correlations and confinement in nonplanar two-dimensional dimer models. *Phys. Rev. B*, 73:144504, 2006.

[43] J Michael Kosterlitz. Kosterlitz–Thouless physics: a review of key issues. *Reports on Progress in Physics*, 79(2):026001, 2016.

[44] J Jacobsen and P Zinn-Justin. Algebraic Bethe ansatz for the $\mathrm{FPL}^2$ model. *Journal of Physics A: Mathematical and General*, 37(29):7213–7225, 2004.

[45] P. Zinn-Justin. *Six-Vertex, Loop and Tiling Models: Integrability and Combinatorics*. Lambert Academic Publishing, 2009.

[46] R. J. Baxter. Colorings of a hexagonal lattice. *Journal of Mathematical Physics*, 11(3):784–789, 1970.

[47] J. Cardy. *Scaling and Renormalization in Statistical Physics (Cambridge Lecture Notes in Physics)*. Cambridge University Press, 1996.

[48] H. C. Bolton and B. S. Lee. Spin-phonon interactions in the compressible Ising magnet. *Journal of Physics C: Solid State Physics*, 3(7):1433–1441, 1970.

[49] H. L. Scott. Anisotropic Ising model with four-spin interactions: Application to lipid bilayers. *Phys. Rev. A*, 37:263–268, 1988.

[50] S. S. Aplesnin. Quantum spin liquid in an antiferromagnet with four-spin interactions. *Physics of the Solid State*, 39(8):1246–1250, 1997.

[51] Jian-Ping Lv, Youjin Deng, and Qing-Hu Chen. Worm-type Monte Carlo simulation of the Ashkin-Teller model on the triangular lattice. *Phys. Rev. E*, 84:021125, 2011.

[52] Jané Kondev and Christopher L. Henley. Kac-Moody symmetries of critical ground states. *Nuclear Physics B*, 464(3):540 – 575, 1996.

[53] G. J. Sreejith and Stephen Powell. Critical behavior in the cubic dimer model at nonzero monomer density. *Phys. Rev. B*, 89:014404, 2014.

[54] P. M. Chaikin and T. C. Lubensky. *Principles of Condensed Matter Physics*. Cambridge University Press, 2000.

[55] K.F. Riley, M.P. Hobson, and S.J. Bence. *Mathematical Methods for Physics and Engineering: A Comprehensive Guide*. Cambridge University Press, 2006.

[56] S T Bramwell and P C W Holdsworth. Magnetization and universal sub-critical behaviour in two-dimensional XY magnets. *Journal of Physics: Condensed Matter*, 5(4):L53–L59, 1993.

[57] S. T. Bramwell and P. C. W. Holdsworth. Magnetization: A characteristic of the Kosterlitz-Thouless-Berezinskii transition. *Phys. Rev. B*, 49:8811–8814, 1994.

[58] Ling Wang, K. S. D. Beach, and Anders W. Sandvik. High-precision finite-size scaling analysis of the quantum-critical point of $S = 1/2$ Heisenberg antiferromagnetic bilayers. *Phys. Rev. B*, 73:014431, 2006.

[59] Stefanos Papanikolaou, Erik Luijten, and Eduardo Fradkin. Quantum criticality, lines of fixed points, and phase separation in doped two-dimensional quantum dimer models. *Phys. Rev. B*, 76:134514, 2007.

[60] Fabien Alet. *Dimères classiques en interaction & Autres problèmes en magnétisme quantique*. Habilitation à diriger des recherches, Université Paul Sabatier (Toulouse 3), 2016.

[61] R. J. Baxter. *Exactly Solved Models in Statistical Mechanics*. Academic Press, 1982.

[62] Masuo Suzuki. Solution of Potts Model for Phase Transition. *Progress of Theoretical Physics*, 37(4):770–772, 1967.

[63] L. D. C. Jaubert, J. T. Chalker, P. C. W. Holdsworth, and R. Moessner. Spin ice under pressure: Symmetry enhancement and infinite order multicriticality. *Phys. Rev. Lett.*, 105:087201, 2010.

[64] L. Benguigui. Critical point of infinite type. *Phys. Rev. B*, 16:1266–1269, 1977.

[65] A. C. Maggs and V. Rossetto. Local simulation algorithms for Coulomb interactions. *Phys. Rev. Lett.*, 88:196402, 2002.

[66] David J. Griffiths. *Introduction to Electrodynamics*. Cambridge University Press, 2017.

[67] T. D. Schultz, D. C. Mattis, and E. H. Lieb. Two-dimensional Ising model as a soluble problem of many fermions. *Rev. Mod. Phys.*, 36:856–871, 1964.

[68] Jørgen Rasmussen and Philippe Ruelle. Refined conformal spectra in the dimer model. *Journal of Statistical Mechanics: Theory and Experiment*, 2012(10):P10002, 2012.

[69] Alexi Morin-Duchesne, Jørgen Rasmussen, and Philippe Ruelle. Integrability and conformal data of the dimer model. *Journal of Physics A: Mathematical and Theoretical*, 49(17):174002, 2016.

[70] Michael E. Fisher and Robert E. Hartwig. *Toeplitz Determinants: Some Applications, Theorems, and Conjectures*, pages 333–353. John Wiley & Sons, Ltd, 1969.

[71] Alexi Morin-Duchesne, Jørgen Rasmussen, and Philippe Ruelle. Dimer representations of the Temperley–Lieb algebra. *Nuclear Physics B*, 890:363 – 387, 2015.

[72] P. Jordan and E. Wigner. Über das Paulische Äquivalenzverbot. *Zeitschrift für Physik*, 47(9-10):631–651, 1928.

[73] Elliott Lieb, Theodore Schultz, and Daniel Mattis. Two soluble models of an antiferromagnetic chain. *Annals of Physics*, 16(3):407 – 466, 1961.

[74] S. Sachdev. *Quantum phase transitions*. Cambridge University Press, 2011.

[75] G. G. Cabrera and R. Jullien. Role of boundary conditions in the finite-size Ising model. *Phys. Rev. B*, 35:7062–7072, 1987.

[76] D. B. Abraham, L. F. Ko, and N. M. Švrakić. Ising model with adjustable boundary conditions: Exact results for finite lattice mass gaps. *Phys. Rev. Lett.*, 61:2393–2396, 1988.

[77] Wulf Rossmann. *Lie Groups: An Introduction Through Linear Groups*. Oxford University Press, 2006.

[78] V Elser. Solution of the dimer problem on a hexagonal lattice with boundary. *Journal of Physics A: Mathematical and General*, 17(7):1509–1513, 1984.

[79] Barry McCoy and Tai Tsun Wu. *The Two-Dimensional Ising Model*. Dover Publications, 2014.

[80] W.T. Lu and F.Y. Wu. Dimer statistics on the Möbius strip and the Klein bottle. *Physics Letters A*, 259(2):108 – 114, 1999.

[81] A.A. Abrikosov, L.P. Gorkov, I.E. Dzyaloshinski, and R.A. Silverman. *Methods of Quantum Field Theory in Statistical Physics*. Dover Books on Physics. Dover Publications, 2012.

[82] P. Fendley, R. Moessner, and S. L. Sondhi. Classical dimers on the triangular lattice. *Phys. Rev. B*, 66:214513, 2002.

[83] Estelle Basor and Torsten Ehrhardt. Asymptotics of block Toeplitz determinants and the classical dimer model. *Comm. Math. Phys.*, 274:427–455, 2006.

[84] Estelle L Basor and Craig A Tracy. The Fisher-Hartwig conjecture and generalizations. *Physica A: Statistical Mechanics and its Applications*, 177(1-3):167–173, 1991.

[85] Albrecht Böttcher and Harold Widom. Szegö via Jacobi. *Linear algebra and its applications*, 419(2-3):656–667, 2006.

[86] Daniel S. Rokhsar and Steven A. Kivelson. Superconductivity and the quantum hard-core dimer gas. *Phys. Rev. Lett.*, 61:2376–2379, 1988.

[87] Helder L. Casa Grande, S. R. Salinas, and F. A. da Costa. Fermionic representation of two-dimensional dimer models. *Brazilian Journal of Physics*, 41(1):86–93, 2011.

[88] Christopher L. Henley. Relaxation time for a dimer covering with height representation. *Journal of Statistical Physics*, 89(3-4):483–507, 1997.

[89] Tom Oakes, Juan P. Garrahan, and Stephen Powell. Emergence of cooperative dynamics in fully packed classical dimers. *Phys. Rev. E*, 93:032129, 2016.

[90] Alessandro Giuliani, Vieri Mastropietro, and Fabio Lucio Toninelli. Haldane relation for interacting dimers. *Journal of Statistical Mechanics: Theory and Experiment*, 2017(3):034002, 2017.

[91] Eduardo Fradkin, David A. Huse, R. Moessner, V. Oganesyan, and S. L. Sondhi. Bipartite Rokhsar–Kivelson points and Cantor deconfinement. *Phys. Rev. B*, 69:224415, 2004.

[92] Eduardo Fradkin. *Field theories of condensed matter physics*. Cambridge University Press, 2013.

[93] Richard Kenyon. Dominos and the Gaussian free field. *Ann. Probab.*, 29(3):1128–1137, 2001.

[94] Béatrice de Tilière. Scaling limit of isoradial dimer models and the case of triangular quadri-tilings. *Annales de l'Institut Henri Poincare (B) Probability and Statistics*, 43(6):729–750, 2007.

[95] Alessandro Giuliani, Vieri Mastropietro, and Fabio Toninelli. Height fluctuations in non-integrable classical dimers. *EPL (Europhysics Letters)*, 109(6):60004, 2015.

[96] Alessandro Giuliani, Vieri Mastropietro, and Fabio Lucio Toninelli. Height fluctuations in interacting dimers. *Ann. Inst. H. Poincaré Probab. Statist.*, 53(1):98–168, 2017.

[97] Alessandro Giuliani, V. Mastropietro, and Fabio Toninelli. Non-integrable dimers: Universal fluctuations of tilted height profiles. *Communications in Mathematical Physics*, 377, 2020.

[98] A. V. Rozhkov. Fermionic quasiparticle representation of Tomonaga-Luttinger Hamiltonian. *European Physical Journal B*, 47(2):193–206, 2005.

[99] A. V. Rozhkov. Class of exactly soluble models of one-dimensional spinless fermions and its application to the Tomonaga-Luttinger Hamiltonian with nonlinear dispersion. *Phys. Rev. B*, 74:245123, 2006.

[100] Thierry Giamarchi. *Quantum physics in one dimension*. Clarendon Press, 2004.

[101] Nicolas Allegra. Exact solution of the 2d dimer model: Corner free energy, correlation functions and combinatorics. *Nuclear Physics B*, 894:685–732, 2015.

[102] Sofian Teber. Bosonization approach to charge and spin dynamics of one-dimensional spin-$\frac{1}{2}$ fermions with band curvature in a clean quantum wire. *Phys. Rev. B*, 76:045309, 2007.

[103] R G Pereira, J Sirker, J-S Caux, R Hagemans, J M Maillet, S R White, and I Affleck. Dynamical structure factor at small $q$ for the XXZ spin-1/2 chain. *Journal of Statistical Mechanics: Theory and Experiment*, 2007(08):P08022–P08022, 2007.

[104] Alexander L. Fetter and John Dirk Walecka. *Quantum theory of many-particle systems*. Dover Publications, Mineola, N.Y, 2003.

[105] Sumathi Rao and Diptiman Sen. *An Introduction to Bosonization and Some of its Applications*. Hindustan Book Agency, 2001.

[106] D. Sénéchal. *An Introduction to Bosonization*, pages 139–186. Springer New York, 2004.

[107] J. Sirker. The Luttinger liquid and integrable models. *International Journal of Modern Physics B*, 26(22):1244009, 2012.

[108] Werner Krauth and R. Moessner. Pocket Monte Carlo algorithm for classical doped dimer models. *Phys. Rev. B*, 67:064503, 2003.

[109] T. Banks, R. Myerson, and J. Kogut. Phase transitions in Abelian lattice gauge theories. *Nuclear Physics B*, 129(3):493–510, 1977.

[110] C. Dasgupta and B. I. Halperin. Phase transition in a lattice model of superconductivity. *Phys. Rev. Lett.*, 47:1556–1560, 1981.

[111] Stephen Powell. Universal monopole scaling near transitions from the Coulomb phase. *Phys. Rev. Lett.*, 109:065701, 2012.

[112] Stephen Powell. Confinement of monopoles and scaling theory near unconventional critical points. *Phys. Rev. B*, 87:064414, 2013.

[113] Stephen Powell and J. T. Chalker. $SU(2)$-invariant continuum theory for an unconventional phase transition in a three-dimensional classical dimer model. *Phys. Rev. Lett.*, 101:155702, 2008.

[114] D. Charrier, F. Alet, and P. Pujol. Gauge theory picture of an ordering transition in a dimer model. *Phys. Rev. Lett.*, 101:167205, 2008.

[115] D. Charrier and F. Alet. Phase diagram of an extended classical dimer model. *Phys. Rev. B*, 82:014429, 2010.

[116] Stefanos Papanikolaou and Joseph J. Betouras. First-order versus unconventional phase transitions in three-dimensional dimer models. *Phys. Rev. Lett.*, 104:045701, 2010.

[117] Michael Hermele, Matthew P. A. Fisher, and Leon Balents. Pyrochlore photons: The $U(1)$ spin liquid in a $S = \frac{1}{2}$ three-dimensional frustrated magnet. *Phys. Rev. B*, 69:064404, 2004.

[118] Christopher L. Henley. Ordering due to disorder in a frustrated vector antiferromagnet. *Phys. Rev. Lett.*, 62:2056–2059, 1989.

[119] Stephen Powell. Higgs transitions of spin ice. *Phys. Rev. B*, 84:094437, 2011.

[120] Xiao-Gang Wen. Quantum orders and symmetric spin liquids. *Phys. Rev. B*, 65:165113, 2002.

[121] G. J. Sreejith, Stephen Powell, and Adam Nahum. Emergent SO(5) symmetry at the columnar ordering transition in the classical cubic dimer model. *Phys. Rev. Lett.*, 122:080601, 2019.

[122] K. Binder. Finite size scaling analysis of Ising model block distribution functions. *Zeitschrift für Physik B Condensed Matter*, 43(2):119–140, 1981.

[123] Alan M. Ferrenberg and D. P. Landau. Critical behavior of the three-dimensional Ising model: A high-resolution Monte Carlo study. *Phys. Rev. B*, 44:5081–5091, 1991.

[124] Massimo Campostrini, Martin Hasenbusch, Andrea Pelissetto, and Ettore Vicari. Theoretical estimates of the critical exponents of the superfluid transition in $^4$He by lattice methods. *Phys. Rev. B*, 74:144506, 2006.

[125] L. D. C. Jaubert. *Topological constraints and defects in spin ice.* PhD thesis, ENS Lyon, 2009.

[126] Cristiano Nisoli, Roderich Moessner, and Peter Schiffer. Colloquium: Artificial spin ice: Designing and imaging magnetic frustration. *Rev. Mod. Phys.*, 85:1473–1490, 2013.

[127] Jason S. Gardner, Michel J. P. Gingras, and John E. Greedan. Magnetic pyrochlore oxides. *Rev. Mod. Phys.*, 82:53–107, 2010.

[128] Roderich Moessner and Kumar S. Raman. Quantum dimer models. In C. Lacroix, F. Mila, and P. Mendels, editors, *Introduction to Frustrated Magnetism: Materials, Experiments, Theory*, volume 164. Springer, 2011.

[129] Louis-Paul Henry and Tommaso Roscilde. Order-by-disorder and quantum Coulomb phase in quantum square ice. *Phys. Rev. Lett.*, 113:027204, 2014.